TÉCNICO LISBOA

Fluid Structure Interaction With Beam Models

Diogo José Martins Cerdeira

Thesis to obtain the Master of Science Degree in

Aerospace Engineering

Supervisors: Prof. Fernando José Parracho Lau
Dr. Guilherme Nuno Vasconcelos Beleza Vaz

Examination Committee

Chairperson: Prof. Afzal Suleman
Supervisor: Prof. Fernando José Parracho Lau
Member of the Committee: Dr. João Lucas Dozzi Dantas

July 2022

Dedicated to my parents Isabel and José and my brother Duarte.

Acknowledgments

First of all, I would like to express my gratitude to Dr. Guilherme Vaz for igniting this study, sharing with me his immense experience and knowledge on the domain and motivating me constantly to go further in the elaboration of this thesis and its goals. I also wish to thank professor Fernando Lau, whose pertinent and helpful feedback greatly contributed for the guiding of my work and the development of this document. I extend this gratitude to Tiago Gomes as well, whose input on the final stages of the thesis was crucial for its conclusion. In addition, I also would like to acknowledge the key role that WavEC and blueOASIS played in this thesis and thank both companies, for providing the necessary means and proper formation that allowed the completion of this work.

I would also like to show my deep gratitude to my friends Sofia, Campos, Madalena and Gomes, as well as to everyone who has been by my side since way before my academic path in Técnico Lisboa started. I am also particularly grateful to Bezerra, Maria, Neves, Mariana and all the friends I made along these last years in Técnico Lisboa and ISAE-SUPAERO, whose feedback and support were crucial for the development of this thesis.

Lastly, I would like to thank my parents Isabel and José and my brother Duarte, to whom this thesis is dedicated to, not only for making this entire journey possible, but also for the unmatchable support and essential motivation they've always provided me.

Resumo

Nos últimos anos, a procura de energia eólica tem aumentado com a crescente geração de energia sustentável, o que levou ao desenvolvimento de geradores cada vez mais potentes, com turbinas de maior dimensão. Pretendendo atingir uma maior eficiência no estudo desses modelos, uma interface entre modelos de viga e malhas do fluído é desenvolvida, expandindo a compatibilidade de um módulo de interação fluído-estrutura (IFE), já existente, para elementos de viga. Visando a independência desse módulo relativamente à obtenção dos dados estruturais do modelo de viga, é criado um modelo computacional responsável pela sua geração, com base no Método de Elementos Finitos. Esta nova funcionalidade é validada com sucesso num problema bidimensional de referência num contexto IFE, assim como o acoplamento de interface implementado. Os desvios obtidos nos resultados foram atribuídos à falta de refinamento da malha estrutural exterior que interage com o fluído. Foram também identificadas limitações neste acoplamento, em que se inferiu que a falta de refinamento da malha da viga em comparação com a malha estrutural externa pode criar superfícies irregulares no corpo, levando a divergência do código. Tendo em vista a simulação do rotor DTU 10MW, são executadas simulações rígidas com Malhas Deslizantes e com o Método de Formulação Absoluta, tendo a primeira abordagem obtido resultados mais fiáveis. Os dados estruturais de entrada do módulo IFE para uma pá do rotor são também formulados com sucesso, utilizando o módulo de viga desenvolvido. A combinação destes avanços deverá levar a simulações futuras bem sucedidas desse mesmo rotor.

Palavras-chave: Aeroelasticidade, Interação fluído-estrutura, Acoplamento de interface, MFC

Abstract

In the past several years, the demand for wind energy has increased with the rising need for sustainable energy generation, which led to the escalation of power and size of the wind turbines. Aiming to study these new prototypes at realistic full-scale with efficiency, an interface is developed between a beam structural representation of the body and the fluid mesh, expanding the compatibility of an already existent Fluid-Structure Interaction (FSI) module to beam elements. Aiming to remove the dependency on other software, a solver responsible for generating the input data regarding the beam models is created, based on the Finite Element Method. This new structural solver is then successfully validated in a FSI context with a 2D benchmark, as well as the implemented interface coupling. Obtained deviations of the results were attributed to the lack of refinement of the outer mesh that interacts with the fluid. Limitations in this coupling were also identified, as it was founded that a lack of refinement from the beam grid in comparison with the outer mesh creates irregular surfaces in the body, possibly leading to divergence. Planning to simulate the DTU 10MW rotor, rigid simulations are executed with Sliding Grids and Absolute Formulation Method approaches, with the former presenting more reliable results. The structural input data of the FSI module for a blade of the rotor is also formulated successfully with the developed beam solver and the combination of these advancements should lead to successful future simulations of the turbine, with a parallelized code.

Keywords: Aeroelasticity, Fluid Structure Interaction, Interface coupling, CFD

Contents

List of Tables

List of Figures

Nomenclature

Greek Symbols	Description	Unit
Γ	Interface between fluid and structure grids	-
δ	Logarithmic decrement	-
ζ	Damping ratio	-
θ	Node rotation	rad
μ	Mass per length	kg/m
v	Poisson factor	-
ξ	Perpendicular distance between parallel axes	m
ρ	Density	kg/m^3
τ	Period of vibration	s
ϕ	Non-orthogonality angle	rad
ψ	Local scalar quantity	-
Ω	Angular speed	rad/s
ω	Natural angular frequency	rad/s

Roman Symbols	Description	Unit
A	Cross section area	m^2
B	External force	N
c	Chord	m
D	Rotor diameter	m
E	Young's modulus	N/m^2
F	Thrust	N
f	Face centroid	-
G	Shear modulus	N/m^2
I	Area moment of inertia	m^4
J	Torsional moment of inertia	m^4
k	Turbulent kinetic energy	J
L	Element length	m
M	Moment	Nm
$\boldsymbol{n}$	Outwards normal unit vector	m

p	Pressure	Pa
R	Turbine radius	m
Re	Reynolds number	-
S	Surface	-
T	Stress tensor	N/m^2
t	Time	s
$\boldsymbol{u}$	Displacement array	m
V	Volume domain	-
$\boldsymbol{v}$	Velocity array	m/s

Subscripts	
0.7	Radial section at 70% of blade's length
c	Critical
CM	Control Mass
CV	Control Volume
d	Damped
f	Fluid
i	Mesh Identification
j	Row Identification
n	Nodal
o	Exact
sh	Shear
s	Structural
t	Turbulent
w	Wind
x,y,z	Cartesian components
θ	Rotations

Superscripts	
H2	HAWC2
i	Element Identification
sc	Shear center
T	Transpose

Acronyms

2D	Two-dimensional
3D	Three-dimensional
AFM	Absolute Formulation Method
ALE-VMS	Arbitrary Lagrangian–Eulerian Variational Multi-Scale
BAM	Beam ANSYS Model
BC	Boundary Condition
BECAS	BEam Cross section Analysis Software
BEM	Blade Element Momentum
BL	Boundary Layer
BSM	Beam Solver Model
CFD	Computational Fluid Dynamics
CM	Control Mass
CSD	Computational Structural Dynamics
CV	Control Volume
DTU	Technical University of Denmark
FEM	Finite Element Method
FFT	Fast Fourier Transform
FOWT	Floating Offshore Wind Turbine
FSI	Fluid Structure Interactions
FVM	Free-Vortex Method

HAWT	HorizontalAxis Wind Turbine
HB	Harwell-Boeing
KSKL	K Square-root-K L (model)
MPI	Message Passing Interface
NLH	Non-linear Harmonic
NNI	Nearest Neighbour Interpolation
NREL	National Renewable Energy Laboratory
NS	Navier Stokes
NURBS	Non-Uniform Rational Basis Spline
OWT	Offshore Wind Turbine
PETSc	Portable Extensible Toolkit for Scientific Computation
RANS	Reynolds-Averaged Navier-Stokes
RHS	Right-Hand Side
RNA	Rotor-Nacelle Assembly
RWT	Reference Wind Turbine
ReFRESCO	Reliable & Fast RANS Equations (solver for) Ships, Cavitation and Offshore
SAS	Scale Adaptive Simulation
SFWVRM	Simplified Free Wake Vortex Ring Method
SG	Sliding Grids
SIMPLE	Semi Implicit Method for Pressure Linked Equations
SM	Solid Model
TSR	Tip Speed Ratio

Chapter 1

Introduction

Firstly, a context of the current status and trend of the offshore wind power is established, propelling the study that follows. Afterwards, a literature review on studies of wind turbines is introduced, with an assessment of knowledge gaps to be addressed by this thesis. The introduction ends with the objectives and scope of the present work.

1.1 Motivation

Nowadays, there is a remarkable development of the wind power technology in Europe, in alignment with the rising awareness of the need for sustainability in electrical power generation. This presents a reality for both onshore and offshore environments, with the latter being one of the focal points of this study.

As it can be noted in Table 1.1, the total installed capacity in Europe of offshore wind turbines increased approximately from 2 to 25 GW, from 2009 to 2020, exhibiting a clear tendency to keep expanding its implementation in the future. This growth can be attributed to the highly competitive costs of this technology in comparison to other renewable sources of energy [1], as well as to the possibility of using more powerful generators offshore than on the onshore environment. The offshore wind turbines originate from the lack of obstacles at the sea, where the access to exceptional quality of wind resources leads to the exploitation of strong and undisturbed wind flows.

It is worth noting that, according to a report from the National Renewable Energy Laboratory (NREL) [2], the COVID-19 pandemic didn't hinder significantly the installation of this technology and its rising trend, as most countries consider the energy sector an essential service and allowed on going construction activities to proceed, even in the presence of lockdowns.

Therefore, the continuing demand for turbines with bigger capacity and their installation further from the shore, with exceptional quality of the wind resources, lead to the design of larger rotors and blade sizes. The installation of these larger machines presents the best cost-effective energy production means to increase the power supply and their conceptualization is paramount to achieve high efficiency in the energy production of the wind turbine farms.

Table 1.1: Growth of offshore wind turbines in Europe over the years [3], with updated values for 2020 from the annual report of NREL [2].

	Current average				Trends	
Years	**2009**	**2014**	**2019**	**2020**	**2025**	**2030**
Number of Offshore Turbines	828	2488	5047	5402	11126	16850
Installed Capacity [GW]	2.06	8.05	22.07	25.1	47.4	76
Average Power [MW]	2.9	3.7	7.2	8.2		

In that sense, computational aeroelastic tests, combining the structural and fluid domains, can provide efficient and accurate methods that allow the optimization of these new devices, promoting thus a safe development and installation of more offshore wind turbines, with higher energy yield per unit of installation area.

1.2 Topic overview

1.2.1 Blade Element Momentum theory

An industry standard for the aeroelastic simulations of Horizontal Axis Wind Turbines (HAWT) and their design is based on the Blade Element Momentum (BEM) theory, which has been proven to have achieved good computational efficiency and an adequate flow response in multiple works [1]. Its formulation, introduced by Glauert [4], corresponds to a combination of the momentum theory and the blade element theory. While the former theory refers to a control volume analysis with conservation of momentum, the latter concerns a force analysis of a discretized blade in function of the incoming flow and the blade geometry [5]. This method's base formulation has been continuously improved through the introduction of new sub-models, aiming to keep up with the evolution of the design and testing of wind turbines [1].

For example, aiming to expand its applicability to the study of Floating Offshore Wind Turbines (FOWTs), in 2007, Jonkman and Junior [6] modeled fully coupled aero-hydro-servo-elastic responses from those machines, with the BEM theory as a foundation for their aerodynamics model. Heege *et al.* [7], rooted in that same theory as well, elaborated a pitch control strategy that compensated the hydrodynamically induced rotor plane speed variations of the OWTs. These and other advancements strongly contributed for the existence of current robust tools that tackle their simulations of HAWTs recurring to the BEM theory, namely HAWC2 [8], from Technical University of Denmark (DTU), and OpenFAST [9], from NREL. These software have been extensively researched and validated, serving as references and/or tools for several works in the wind energy domain [10] [11].

Alternatives to the BEM theory were also added to the code of OpenFAST. For instance, Shaler *et al.* [12] implemented the Free-Vortex Method (FVM) on that software, aiming to study the aero-elastic performance of the NREL UAE Phase IV turbine. A further development on this method was performed by Dong *et al.* [13], where a Simplified Free Wake Vortex Ring Method (SFWVRM) was deployed and tested on the NREL 5MW wind turbine, both on fixed and floating support structures. The obtained

results were proven to be more accurate but computed less efficiently than the ones originated from the BEM theory, with the latter presenting unreliability for small angles of attack in the region of low wind speeds and for high wind speeds with blade pitch motions.

Limitations of this nature are common in simplified models from aero-hydro coupled analysis tools, as many of their assumptions don't necessarily hold up when working with complex aerodynamic flow states [14]. The BEM method has been proven to be unsuitable when the rotor interacts with its own wake [1] [13], while Vortex Methods may lack, for example, on their portrayal of dynamic stall [15] and on the simulation of wind turbines when varying circulation occurs along the blade [16]. These are problems that can be addressed with the application of correction models but the highly skewed flows and heavy detachments typical of FOWTs are still a major obstacle to be surpassed by these tools [1]. Unlike onshore machines, the FOWTs are simultaneously subjected to wind and wave loads, creating translational and gyroscopic motions that are solely constrained by mooring cables. These floating dynamics lead to the operation of these turbines in various complex aerodynamic flow states that can be better tackled with more sophisticated Computational Fluid Dynamics (CFD) techniques, even if at a price of higher computational costs.

1.2.2 CFD simulations of floating offshore wind turbines

Traditional CFD approaches to the simulations of wind turbines are usually considering them as rigid models, that is, with their rotor not presenting any flexibility. Yet, as mentioned in Chapter 1.1, with the upscaling of the modern FOWTs, the study of aeroelastic effects has to come into play, since blade deflections may have an appreciable impact on the turbine performance, as well as their interactions with the tower [1].

In an FSI context, a simulation with the flexible rotor requires its structural model, in addition to the CFD grid with which it will interact. Considering the lack of publicly available studies on industrial configurations, most of the literature review of this thesis, concerning this matter, revolves around reference designs, in which the structural properties of the body are well documented and accessible. Since their inception, Reference Wind Turbines (RWTs) have been used to reflect the current wind energy technology, allowing the galvanization of innovative methods in its design and evaluation. Within this group of machines, the NREL 5MW and the DTU 10 MW tend to stand out with numerous studies focused around them.

In regards to the NREL 5MW RWT, Hsu and Bazilevs [17] and Yu and Kwon [18] studied its behavior, assuming the flexibility of its rotor's blades. While the former made use of a coupling between a low-order Arbitrary Lagrangian–Eulerian Variational Multi-Scale (ALE-VMS) flow solver and a Non-Uniform Rational Basis Spline (NURBS) based structural solver, the latter solved the incompressible Navier–Stokes equations of an unstructured grid for the blade forces and a beam model was used for the computation of the deformations. Both works initially focused on the Rotor-Nacelle Assembly (RNA) of the turbine and, based on its simulations, it was found in the Yu and Kwon's study [18] that the blade aerodynamic loads were significantly reduced by the nose-down torsion resultant of the elastic deformation. Therefore, it

was concluded that the flexibility of the blades should be an important factor to be taken into account when one intends to properly predict the wind turbine aerodynamic performances.

However, simulations with only the RNA omit an important source of unsteadiness: the tower geometry. Both aforementioned works later considered rotor-tower interactions, in order to close in on this gap. Now simulating with the whole machine, Bazilev *et al.* [19] concluded that the tower produced a significant drop in the aerodynamic torque, which generated additional cyclic loading on the blades. Yu and Kwon [18], also in the presence of the tower interference, identified oscillatory behaviors of the blade aerodynamic loads and the aeroelastic deformation, particularly in what concerned the tangential force and the flapwise bending deflection. These alterations not only affect the performance of the machine but should also be considered in fatigue-life analysis of the turbines.

As for the DTU 10MW turbine, RNA simulations were developed by Horcas el al. [1] [20], where the computed blade tip deformation associated to the rated wind speed corresponded to 8 meters, respecting the designed tower clearance of the model. Nevertheless, this deflection led to a 1.4% decrease of the power production of the machine, which corroborates what was already concluded for the NREL 5MW RWT: the blade flexibility is a crucial factor to consider in the estimation of the final rotor performance.

Rotor-tower interactions of this RWT were also explored by Horcas *el al.* [20], using the Non-linear Harmonic (NLH) approach, presented by Vilmin *et al.* [21]. However, this approach made use of rigid blades instead of flexible ones, only meshing a single blade passage due to rotational periodic nature of the problem, where the incoming wind was assumed to be aligned with rotor axis. Considering these assumptions, the presence of the tower still presented a strong influence on the rotor performance, with the computation of an around 5% decrease of time-averaged rotor thrust and 8% of power. Sayer [22] performed a study with identical goals, also for the DTU 10 MW RWT, though this time with flexible blades. Recurring to Reynolds Averaged Navier Stokes (RANS) equations for the CFD solver and a Finite Element Method (FEM) software to compute the structural deformations of a beam model, it was possible to observe that, similarly to the NREL 5MW turbine, the deformations in all directions were reduced after the blade passed by the tower, due to an abrupt decrease of the aerodynamic loads resultant of the tower-rotor interactions.

Hence, as it will be presented in Chapter 1.3, this work intends not only to perform similar flexible simulations to the ones conducted in this literature review, but also set the stage for future works, where, for example, rotor-tower interactions may be studied.

1.2.3 Structural representation of the rotor

As stated in Otero *et al.* [23], the wind turbine industry aims to implement structural models increasingly capable of capturing the complex features of new blade prototypes, simulated at realistic full-scale conditions with reasonable computational costs. Considering this goal, different approaches can be taken with the structural representation of an offshore wind turbine. The Finite Element Method, explained on Chapter 2, offers an extensive selection of elements to approximate any body and, for

the present case, there are several works approaching its aeroelastic studies through beam and shell elements. This approach doesn't require as much computational costs as three-dimensional (3D) tetrahedral or hexahedral elements and it doesn't necessarily lose accuracy in process of the simplification of the computations.

In the work of Júnior *et al.* [24], a comparison is established between the behavior of these two types of elements, regarding the modelling of a wind turbine blade. According to its results, while the beam models do not convey local buckling phenomenons and detailed information on the stress distribution of the blades, they present themselves as reliable choices to an overall study and design of a wind turbine system, with fast and accurate results for static and dynamic simulations. These results presented a good agreement with the ones obtained for shell models, even for high levels of induced bending and torsion. Other studies corroborate this accuracy, such as Sharma *et al.* [25], where static simulations of a beam representing the NREL S818 blade were validated, and Tüfecki *et al.* [26], where the dynamic analysis of a blade from the DTU 10 MW RWT was also successfully validated with a beam model. This type of elements are also adopted to approximate the entire body of the wind turbines in the aforementioned software HAWC2 and OpenFAST.

Beam elements have also been largely used in an FSI context. Yu and Kwon [18] investigated the aeroelastic response of the NREL 5MW RWT employing as a structural solver a nonlinear Euler-Bernoulli beam undergoing spanwise, torsional and lead-lag and flap bending deformations. Sayed *et al.* [22] accomplished a similar goal, by developing an FSI coupling between a CFD solver and the software Caratt^{++}, responsible for calculating the elastic deformations, also based on non-linear Timoshenko beam elements. This coupling was then successfully tested on the DTU 10 MW turbine, after the coupling and aeroelastic verification was performed with simpler benchmarks. The used mechanism is portrayed in Figure 1.1, where the properties of the rotor's blade are carried by the beam model (black grid), with all the rigidity of the body concentrated on itself.

Similarly, Almeida [27] developed a coupling between beam models and the surrounding CFD grid, in this case to perform aeroelastic studies on wings. The FSI module was tested on a rectangular wing with a NACA0015 airfoil and the computed results were compatible with theoretical expectations, making it an appropriate wing aeroelastic performance predictor for early stages of aircraft design.

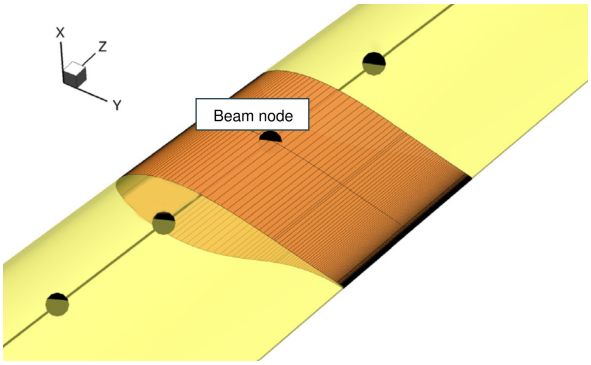

Figure 1.1: Representation of sectional area used to calculate the aerodynamic loads and Computational Structural Dynamics (CSD) mesh, which corresponds to the black dotted line, of a blade from the DTU 10MW RWT (from Sayed [22]).

Concerning the use of shell models in CFD simulations, Bazilevs *et al.* [19] conducted their RNA and full machine simulations with the structural model of the composite blades defined by the Kirchhoff–Love shell formulation [28], in conjunction with the bending strip method [29]. The resulting aerodynamic parameters and blade tip deflections had a good agreement with the documentation of the turbine at study, from which it its possible to infer that these elements should be reliable to represent the rotor of a FOWT.

1.3 Objectives and deliverables

The fluid solver employed in this work corresponds to ReFRESCO, a multi-phase viscous flow solver where a FSI module has already been implemented by Jongsma and Windt [30].

While 3D elements, such as solids, have already been successfully tested with this module on the work of Bronswijk [31], with the intent of representing a marine propeller, it is clearly necessary to obtain less complex computations and mathematical simplicity in the simulations of a body like the blade of a wind turbine. Stemming from the literature review previously stated, one intends to formulate a beam model representing that body and then test it in the FSI module. This possible simplification of the simulations arises nonetheless the need for compatibility of ReFRESCO with beam elements, which is not yet implemented and constitutes a main goal in this thesis.

In addition to this problematic, currently the FSI module is reliant on outsourcing the generation of the structural data of the model to external commercial software, namely ANSYS© Mechanical. Aiming to remove this dependency of ReFRESCO, the objective of creating a computational structural dynamics model is set. The already existent documentation on beam solvers and the complexity associated to the formulation of shell models makes the first type of elements preferable to the latter. An adjunct module is thus coded to work linked to ReFRESCO, providing it the structural data of any beam model at hand.

After applying these elements on simpler models and developing more efficient solvers, one may obtain a better understanding of the influence of these elements on the performance of the simulations, while also being able to decrease the computational load associated to wind turbine calculations, aiding on a focal point of this thesis: the aeroelastic study of a DTU 10MW RWT.

In addition to the testing of the new interface with beam elements and the developed solver on a two dimensional (2D) benchmark, a RWT is also considered as an object of study for this work. Based on the literature review previously stated, the concept description of a 10 MW wind turbine, that was proposed by the DTU in 2013, corresponds to an adequate choice for this thesis. As mentioned before, the DTU 10MW RWT has significant research interest from the wind energy domain and it is chosen due to the public availability of its documented geometry, as well as due to the existence of all the aforementioned studies encompassing it. Therefore, it is established that an approximation of the DTU 10 MW RWT rotor is to be executed with three dimensional beam elements, on a full scale.

Having all the aforementioned problematics in mind, one aims to:

1. Develop an interface between beam elements and the fluid grid on the FSI module of ReFRESCO;

2. Expand on the features of the FSI module by creating a beam solver, which provides structural data to the simulation;

3. Validate the interface and the developed beam module with a benchmark from available literature;

4. Test the beam solver on a full scale turbine, the DTU 10 MW RWT.

To sum up, for a better understanding of the knowledge gaps to be addressed in this thesis and of the planned deliverables, refer to the flowchart from Figure 1.2.

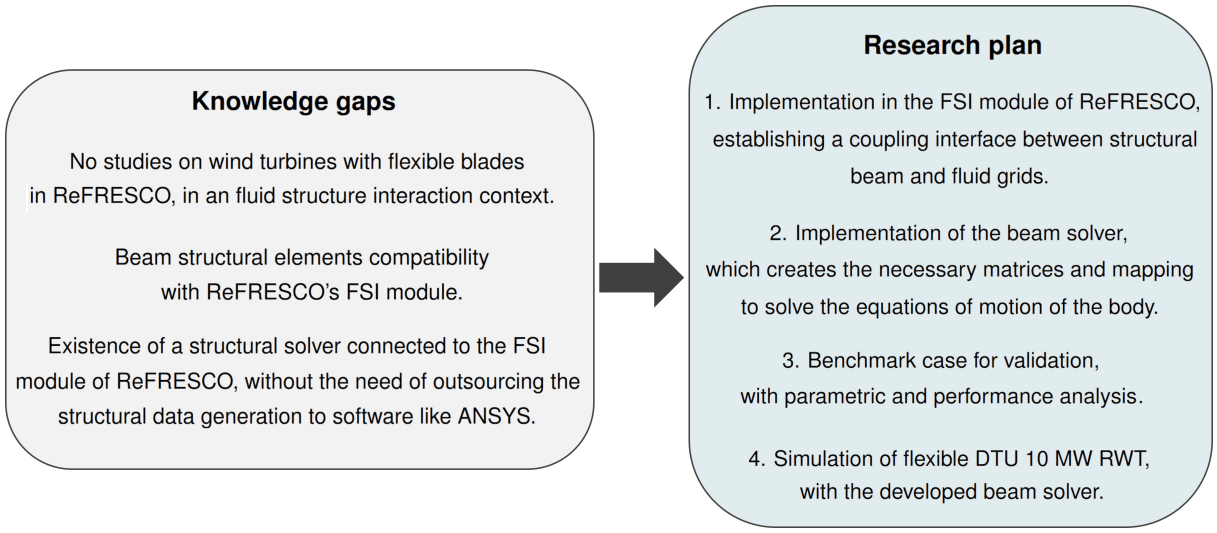

Figure 1.2: Knowledge gaps and research plan of the thesis.

1.4 Thesis outline

Before the actual study is started, in Chapter 2, some theoretical background is covered in regards to the solving numerical methods of fluid and structure.

In Chapter 3, the functioning of the FSI module of ReFRESCO is covered, as well as the implementation carried out in its code, with the objective of making it compatible with beam elements.

Afterwards, in Chapter 4, the theoretical formulation of the beam elements from the new developed solver is explained with the finite element method as a through line. Moreover, the practical development of the program is addressed, where the data input of the solver is specified and each step is covered. This Chapter ends with the validation and verification of the solver, through static and dynamic analysis, with ANSYS© results as a reference.

In Chapter 5, numerical simulations are executed on a reference case in order to validate the computational structural dynamics model on a FSI context. Considering as reference the results of a flexible model with solid elements, the beam interface with the flow is evaluated on a simulation where the data is generated by ANSYS©. This process is followed by the validation of the beam solver, where the supplied structural data to the FSI simulation is originated from it. Furthermore, performance and sensitivity studies of the solver are conducted.

Finally, Chapter 6 deals with the simulations concerning the DTU 10 MW RWT, recurring to the developed beam solver. It covers the formulation of a rigid and a flexible model for the rotor of said turbine. These simulations and the one performed on Chapter 5 are made clear in the flowchart of Figure 1.3.

The thesis is concluded with a summary of the accomplished achievements and suggestions for future work in Chapter 7.

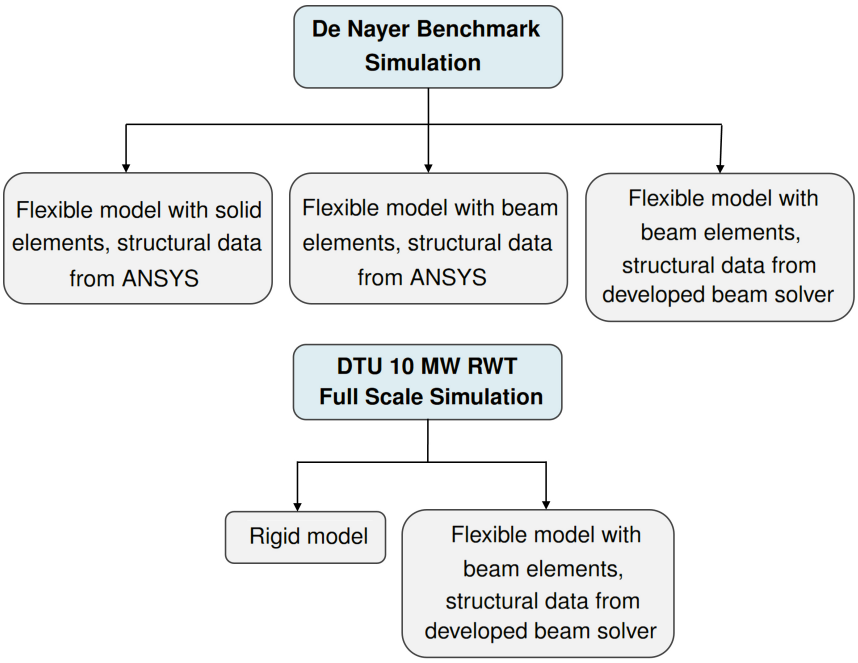

Figure 1.3: Simulations performed on the present work.

Chapter 2

Numerical methods

The current Chapter covers key concepts related to the fluid and structure problems. Background knowledge on the RANS equations is introduced, as well as the most relevant methods and settings of the solver ReFRESCO. Furthermore, important parameters associated to the grid quality and accuracy of the generated fluid meshes are presented.

In regards to the structural portion of the problem, the Finite Element Method and the effects of viscous damping in a body with free vibration are introduced. These aspects will be heavily referenced in the following Chapters 3 and 4.

2.1 Fluid problem

2.1.1 Governing equations

When studying fluid motion, it is essential to state the fundamental governing equations that describe the evolution of the fluid flow. This goal can be achieved mathematically through conservation laws, obtained by considering a control mass CM and its extensive properties, such as mass, momentum and energy. However, in fluid flows, it is difficult to deal with a parcel of matter, being more convenient to work within a control volume CV [32]. From this volume approach comes the general conservation equation:

$$\frac{d}{dt}\int_{V_{CM}} \rho\psi \, dV = \frac{d}{dt}\int_{V_{CV}} \rho\psi \, dV + \int_{S_{CV}} \rho\psi(\boldsymbol{v} - \boldsymbol{v_b}) \cdot \boldsymbol{n} \, dS, \tag{2.1}$$

where V_{CV} and V_{CM} are the CV and CM volumes, S_{CV} constitutes the surface enclosing CV and n the unit normal vector to that surface. The parameters v and v_b represent the velocity of the fluid and of the CV surface, respectively, while ψ is any conserved intensive property.

From Equation 2.1, one can obtain the conservation equations of mass, momentum or of any conserved scalar quantity [32]. As in this study the fluid is assumed to be isothermal in all simulations, the equations of Navier Stokes (NS) represent two physical conservation laws: the mass conservation Equation 2.2a, for $\psi = 1$, and the momentum conservation Equation 2.2b, for $\psi = \boldsymbol{v}$.

$$\frac{d}{dt}\int_V \rho\, dV + \int_S (\rho \boldsymbol{v}) \cdot \boldsymbol{n}\, dS = 0 \tag{2.2a}$$

$$\frac{d}{dt}\int_V \rho v_i\, dV + \int_S \rho v_i \boldsymbol{v} \cdot \boldsymbol{n}\, dS = \int_S T \cdot \boldsymbol{n}\, dS + \int_V \rho f_i\, dV \tag{2.2b}$$

with f_i as the body forces per unit of mass and T as the stress tensor.

One can then make a statistical approach to the problem at hand by averaging these flow equations, while reattaining the most relevant terms and modelling the turbulence effects with additional turbulence models [33]. This process leads to the Reynolds-Averaged Navier-Stokes equations used in ReFRESCO.

2.1.2 ReFRESCO

As stated in Chapter 1, this work aims to expand on the functionalities of the CFD code ReFRESCO, specifically its 2.7.0 version, in order to test it on a wind turbine model. This software solves multiphase incompressible viscous flows through the Navier-Stokes equations stated in Chapter 2.1.1, which is conveyed by the name it stands for: Reliable & Fast RANS Equations (solver for) Ships, Cavitation and Offshore [34].

Due to the complexity of these equations, a numerical approach is needed through the discretization of the domain with the Finite Volume Method, using cell centred collocated variables, i.e. flow properties whose values are stored at the cell's center [35]. This algorithm requires multiple iterative processes, accounting for the equations of momentum, mass/pressure, volume fraction, turbulence and other transport equations. One of those iterative processes corresponds to the velocity-pressure coupling, which is achieved with the aid of a pressure-weighted interpolation method, combined with a segregated pressure-correction algorithm (the Semi-Implicit Method for Pressure Linked Equations, also known as SIMPLE, whose procedure is presented in Figure 2.1). All the iterative processes associated to other transport equations are treated in a segregated mode as well, where the equations for a certain variable are solved for all cells [33].

Time iterations are performed implicitly through first or second-order backward schemes [36], with a typical solving process in ReFRESCO containing three iteration loops, denoted as the time loop, the outer loop and the inner loop (refer to Figure 2.1). At each time loop, the outer-loops account for non-linearity and deferred corrections, containing within them the inner loops, where the momentum, pressure correction, velocity and turbulence model equations are solved using the parallelized-solvers library PETSc [33]. The process comes to an end and exits the loops when the suitable convergence criteria or the maximum number of outer loops are met.

ReFRESCO also features deforming, moving and sliding grids. The deforming grids are inherently associated to FSI simulations and are used in any case with flexible bodies in this thesis. The moving grids are used particularly in the DTU 10MW RWT model, with the intent of simulating the wind turbine's rotation. In that regard, two distinct CFD grids are pondered for the simulation of that model.

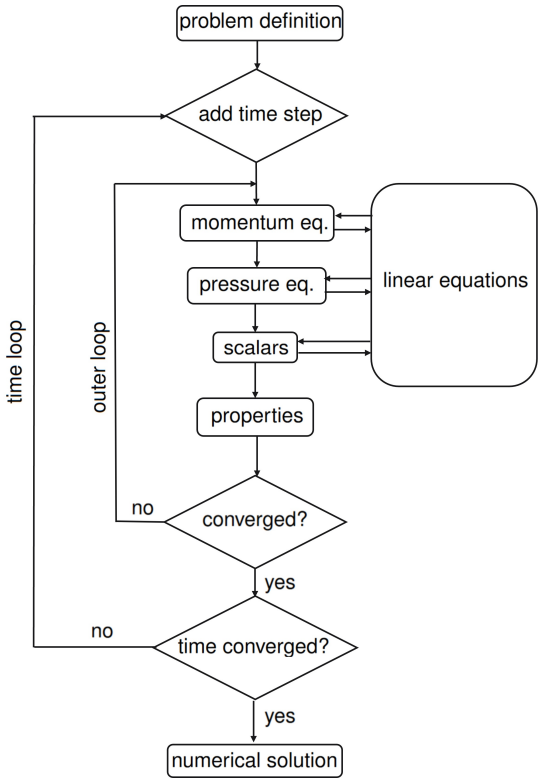

Figure 2.1: Schematic overview of the SIMPLE algorithm in ReFRESCO (adapted from Wieleman [37]).

The first is the Absolute Formulation Method (AFM), in which, according to Make and Vaz [38], "the RANS equations are solved in the moving reference frame but using variables written in terms of absolute or inertial reference frame quantities".

According to the theory manual of ReFRESCO [33], with this formulation, the previous RANS equations can be rewritten as follows in Equations 2.3a and 2.3b.

$$\frac{d}{dt}\int_V \rho\, dV + \int_S (\rho(\boldsymbol{v} - \boldsymbol{v_b})) \cdot \boldsymbol{n}\, dS = 0, \tag{2.3a}$$

$$\frac{d}{dt}\int_V \rho v_i\, dV + \int_S \rho v_i(\boldsymbol{v} - \boldsymbol{v_b}) \cdot \boldsymbol{n}\, dS = \int_S (\mu + \mu_t)[\nabla \boldsymbol{v} + \nabla \boldsymbol{v}^T] \cdot \boldsymbol{n}\, dS + \int_V \left[\nabla\left(p + \frac{2}{3}\rho k\right) - \rho(\boldsymbol{\Omega} \times \boldsymbol{v}) + \rho \boldsymbol{B}\right] dV, \tag{2.3b}$$

where p is the fluid pressure and μ and μ_t are the fluid dynamic viscosity and turbulent viscosity. The parameter $\boldsymbol{\Omega}$ corresponds to the imposed angular velocity, while k and $\boldsymbol{B}$ constitute the kinetic turbulence energy and an external force, respectively. For the evaluation of μ_t, an additional transport model concerning the turbulence of the flow is required.

This formulation implies that the rotor geometry remains thus static, which facilitates the FSI process and its interface coupling. The AFM formulation has been successfully applied at full scale to the NREL 5MW rotor by Vaz *et al.* [38], with the simulations yielding a good quality agreement of the thrust and torque with the full-scale BEM theory based results, made available by NREL. Nevertheless, it should be noted that this method is quite limited with the types of motion it can represent and may struggle to

capture the unsteadiness of the flow [35].

Secondly, considering the state-of-the-art from Chapter 1.2, the AFM approach is not expandable to other more complex test cases, where, for example, rotor-tower interactions are computed. Therefore, Sliding Grids (SG) are also considered for the turbine study, which should not compromise too much the computational cost of the simulations. This method has already been successfully employed in a FSI context with RWTs: Hsu and Bazilevs [19] simulated the NREL 5MW wind turbine using SG, which presented a good conjunction of accuracy and efficiency portraying the motion of the flexible rotor blades and the rotor-tower interactions and; in Leble [39], simulations with SG applied to the DTU 10 MW model successfully depicted the aero-elastic behavior of the rotor undergoing a prescribed motion in yaw and pitch.

Using the SG technique, distinct CFD grids are constructed in order to fit into one another, sharing a common interface [35]. According to Bazilevs *et al.* [17], this approach applied to wind turbines allows that, "*rather than rotating the entire computational domain, only the inner cylindrical subdomain that encloses the rotor undergoes a spinning motion inside the cylindrical cutout of the outer stationary domain*" [40]. These two subdomains do not overlap each other and are in relative motion, creating a sliding cylindrical interface, as depicted in Figure 2.2. A numerical procedure is then responsible for imposing a continuity of kinematics at the interface between the exterior and the interior rotating subdomain, even though the interface discretizations are incompatible between both sub-grids [19].

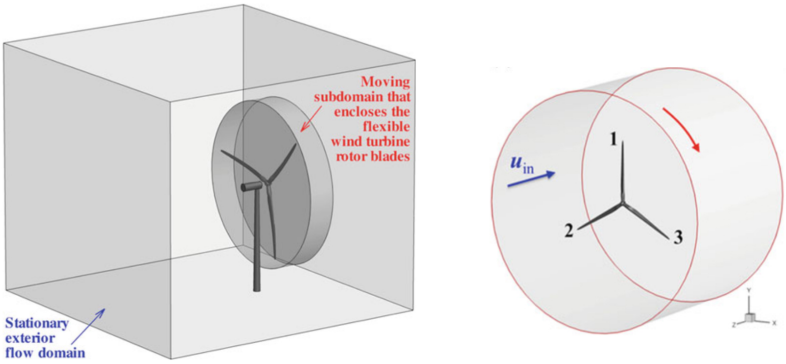

Figure 2.2: SG setup for the simulation of a full wind turbine machine (on the left), with inner subdomain (on the right) [19]

Additionally, ReFRESCO offers the possibility of complementing its simulations with turbulence models to account for turbulence fluctuations, presenting a variety of RANS options. While the k-ω SST 2003 model is initially considered for the turbine simulations in Chapter 6, due to its usual implementation in turbine simulations [1] [41], the $k - \sqrt{k}L$ (KSKL) option is the chosen one to employ in this thesis. It corresponds to a two-equation turbulence model, considering a transport equation for the turbulent kinetic energy k and for $\sqrt{k}L$, where L constitutes an integral length scale [35]. This latter parameter leads to scale-adaptive simulations (SAS), which present the ability to adjust the local flow

scales [33], with proper RANS performance in stable flow regions and adequate adaptation to large turbulent structures in unstable flow regimes [42]. This model thus yields simulations that are quite stable in comparison with the k-ω SST 2003 model, without necessarily losing its accuracy.

It is also worth of mention that the code is parallelised using Message Passing Interface (MPI), where the structural and fluid grids suffer a subdomain decomposition, in which different portions are solved in the distinct processors and then the solution is reassembled. However, the present work involves fundamental changes to the structural portion of the simulations, which makes the altered code only executable with one processor.

2.1.3 Grid quality

The grid quality of the fluid mesh supplied to ReFRESCO is essential to ensure the accuracy of the computed solution. Aiming at ascertaining the reliability of those grids before the simulation, two key parameters are evaluated when generating the CFD meshes: non-orthogonality and skewness. After the simulation is computed, discretization errors can also be adressed, to ensure the grid's accuracy.

Non-orthogonality and skewness

The non-orthogonality corresponds to the value of the angle ϕ between the unit vector joining centroids of two contiguous elements and the unit vector normal to the face shared by both elements [43]. Ideally, this deviation, represented in Figure 2.3, would be null for all the cells of the grid, with both vectors being collinear, as significant non-orthogonality increases the diffusion term in the conservation equation and diminishes the robustness of the discretization method.

The skewness or eccentricity concept is expressed by Figure 2.4, where the line connecting two cell centers doesn't pass through the face's centroid f but through f' instead. Having in account that all face integrations take place at the centroid point f, this deviation of the aforementioned line from that point decreases the second order accuracy of the discretization method [43]. Therefore, optimal fluid grids aim for reduced deviation from the centroid, i.e. reduced skewness.

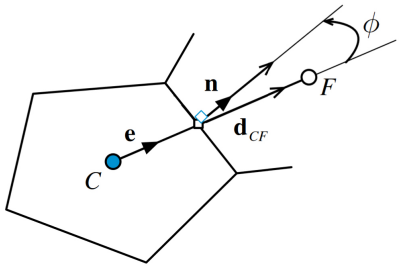

Figure 2.3: Non-orthogonal element (adapted from Moukalled *et al.* [43]).

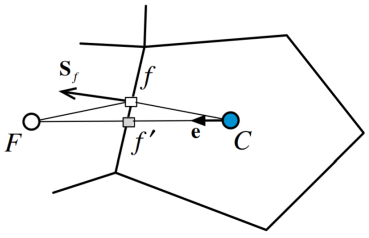

Figure 2.4: Non-conjunctional elements [43]).

Even though these are guiding parameters when developing the CFD grids, it is important to note that ReFRESCO also accounts for the existence of these phenomena, attenuating them through embedded corrections in its non-linear iterations [33].

When already working with the simulations, a new variable is evaluated to assess the fluid grid accuracy: the y^+. It corresponds to the dimensionless nominal distance from the wall to the first layer of cells, indicating the grid spacing adjacent to that wall [35]. Ideally, this parameter should take values close to 1 for low and medium Reynolds numbers, in order to properly resolve the sub-viscous boundary layer (BL) near the wall [44]. For higher Reynolds numbers, it can take higher values and it is used to define the range of applicability of wall functions.

Discretization errors

The discretization errors of the generated grids are obtained based on the work and tools developed by Eça and Hoekstra [45]. An error estimator is initially calculated from Richardson extrapolation, through Equation 2.4.

$$\psi_i - \psi_o = \alpha h_i^p, \tag{2.4}$$

where ψ_i corresponds to the numerical solution of any local scalar quantity on the grid, ψ_o is the estimated continuous solution (i.e., solution with infinity refinement), α is a constant and p and h_i are the order of accuracy and the reference grid cell size, respectively [45].

This estimator is then inserted inserted into Equation 2.5, where a least squares fit of the data takes place.

$$S(\psi_o, \alpha, p) = \sqrt{\sum_{i=1} (\phi_i - (\phi_o + \alpha h_i^p))^2} \tag{2.5}$$

The parameters ψ_o, α and p can then be obtained from the minimization of the function S and a numerical uncertainty equation associated to the data can be written, based on the discretization errors.

2.2 Structural problem

2.2.1 Finite Element Method

The study of the structural behavior of a wind blade requires the idealization of a discrete-element mathematical representation of its continuous structure, with the intent of simplifying the analysis of the model at hand.

With this in mind, relying on its elastic and inertial properties expressed in the matrix form, the approach taken in the present work corresponds to the Finite Element Method, where the geometric domain of a structure is divided in multiple subdomains, called finite elements, and each of these divisions are associated to an approximation function [46]. These functions depend not only on the geometry of the structure, but also on the number and location of points that each element connects, called nodes. At each of these connections, one can establish an algebraic equation that links the physical quantities at study and, after assembling these equations based on continuity, a system can be solved with solutions

for each node. A detailed algorithm of this method is presented bellow, whose reasoning will be closely followed in Chapter 4.

1. **Discretization**: one establishes the division of the spatial domain in finite elements, whose ensemble is called mesh.

2. **Strong and weak formulation**: the governing equations of the problem are enunciated.

3. **Shape Functions**: define an approximation to the solution of the problem as a linear combination of nodal values and approximation functions.

4. **Determination of elementary matrices**: compute element matrices by applying the shape functions to the aforementioned formulation over the element at hand.

5. **Assembly**: inter-element continuity is established by connecting element nodes on their local referential to the nodes on the global coordinate system.

6. **Imposition of boundary conditions (BC)**: the global degrees of freedom of the problem are identified and applied to the assembled equations.

7. **Solving system of linear equations**.

2.2.2 Free vibration with viscous damping

A phenomenon that will be observed in the benchmark simulations, represented in Figure 2.5, corresponds to the viscous damping. This mechanism consists on the dissipation of vibrational energy of the moving body due to the resistance offered by the surrounding fluid [47] and it can be characterized through parameters such as the logarithmic decrement δ and the damping ratio ζ.

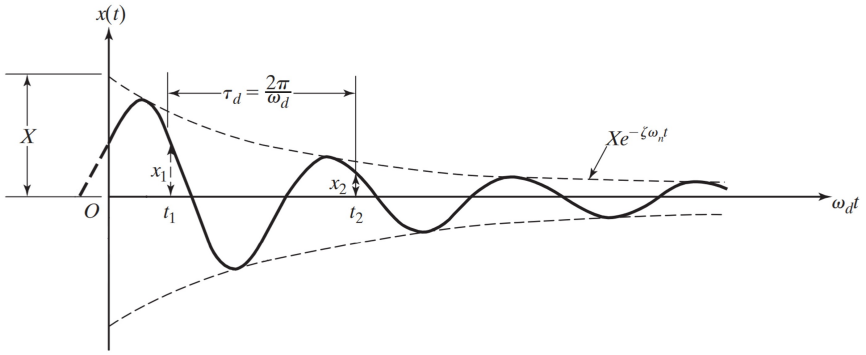

Figure 2.5: Damped vibration (adapted from S. Rao [47]).

The logarithmic decrement, defined in Equation 2.6, is defined as the natural logarithm of the ratio between same phase amplitudes of the free damped motion, representing the rate at which the amplitude of the vibration decreases [47].

$$\delta = \frac{1}{m} \ln \frac{x(t)}{x(t + m\tau_d)}, \tag{2.6}$$

where $x(t)$ and $x(t+m\tau_d)$ denote the amplitudes (displacements) measured m cycles apart and τ_d is the period of the damped vibration. The damping ratio can be easily obtained from this parameter through Equation 2.7.

$$\zeta = \frac{\delta}{\sqrt{(2\pi)^2 + \delta^2}}, \tag{2.7}$$

Chapter 3

Fluid Structure Interaction

The current Chapter focuses on an essential aspect to perform aeroelastic calculations, where a coupling between the structural model of a body and the surrounding fluid must be achieved, in order to solve the equations of motion of the body: the fluid structure interactions problematic.

This class of problems presents a mutual dependence between the structural model and the fluid behavior: the flow properties depend on the shape of the structure and its motion, while the motion and deformation of the structure depend on the fluid loads that are acting on the structural model [48]. This symbiosis between the two domains can be described generally by the Equation of motion 3.1, whose solutions correspond to the focus of any FSI simulation.

$$[M]\ddot{\boldsymbol{x}} + [C]\dot{\boldsymbol{x}} + [K]\boldsymbol{x} = \boldsymbol{F}, \tag{3.1}$$

where [M], [C] and [K] correspond to the mass, damping and stiffness matrices of the body, respectively. The array $\boldsymbol{x}$ represents the nodal displacements and rotations, while $\boldsymbol{F}$ is an array for the nodal applied forces that come from the fluid.

A FSI module was implemented on ReFRESCO by Jongsma and Windt [30] and this thesis has the goal to expand on its features, concerning the types of element it supports. In order to get a clear view of its original functioning, a brief characterization of the algorithm of this module is stated on the current Chapter, as well as a description of the implementation executed on the internal code of ReFRESCO for the purposes of this work.

3.1 FSI in ReFRESCO

Aiming a minimal intervention on the existing solution algorithms for the flow equations, the FSI module of ReFRESCO takes a partitioned approach to solve its problems. A description of this method and the alternative monolithic approach is stated on Table 3.1.

Table 3.1: Numerical solution methods for FSI simulations, concerning solvers.

Partitioned approach	Monolithic approach
It utilizes already available fluid and structural solvers in each domain separately and, through an iterative method, satisfies interface conditions, enabling the use of different discretisation for the fluid and structural grids [49].	Equations for structural and fluid domains are solved simultaneously using an unified solver with a single coupled system of equations [30].

In what concerns the monolithic method, its simultaneous nature with the solving of the fluid and structure equations increases the stability of the simulations, as their mutual influence is evaluated directly [50]. However, it is computationally challenging and mathematically suboptimal in most cases [51], which, combined with the use of existing and optimized software for the fluid and structural problems on the partitioned approach, motivates the choice to utilize the latter method on ReFRESCO.

The partitioned approach also comprises the important feature of allowing different discretisation for the fluid and structural parts of the domain, as the structure typically requires a less refined mesh than the fluid [30]. Nonetheless, one must consider that, in this method, no changes occur to the flow simultaneously to the computation of the structural response, which introduces an additional numerical error to the simulations [31]. Therefore, a coupling mechanism is essential to achieve a robust algorithm with the interaction of the two solvers. In that sense, a dichotomy arises on the partitioned approach: weak and strong coupling, described on Table 3.2.

Table 3.2: Coupling methods for FSI simulations.

Weak coupling	Strong coupling
Coupling of the incompressible flow and structural solvers is performed only once per time step [30].	The solutions from both solvers are exchanged multiple times per time step, until convergence is achieved [30].

While the weak coupling is more appealing in terms of efficiency, the strongly-coupled approach is the adopted one by ReFRESCO [30], due to the existence of stability issues associated to the weak coupling when working with incompressible flows [52]. The overall algorithm of FSI simulations in ReFRESCO is further developed in Chapter 3.1.2, where these approaches become more evident.

3.1.1 Data input

Before analysing the functioning of the FSI simulations step by step, it is essential to understand the fluid and structural data that ReFRESCO requires as input, aiming to solve the equations of motion of the body and determine the flow behavior.

In relation to the structural data, the structural grid with the nodes' coordinates of the model is required, as well as its mass and stiffness matrices. These matrices are crucial to solve the Equation 3.1 and they can be read through two possible formats of input: ANSYS© and Harwell-Boeing (HB) format.

The first case demands input files specific to the ANSYS© software, only supported by ReFRESCO if generated by a version up to the 19.3 R1 one of ANSYS©. As the current release of ANSYS© surpasses that version, this option is not considered in this work.

The second type of input comprises files that can also be created by ANSYS© but are not reliant on the version of the software and can be read outside of it: the Harwell-Boeing format. This type of file is responsible for storing information concerning sparse matrices and includes an header that supplies a variety of information concerning the matrix at hand, such as its type, dimensions, number of non zero entries, format descriptors for its values, among other aspects [53]. This header is then followed by a list of the numerical entries of the matrix that respect the format assigned previously. Other information regarding the mesh mapping with the equations of the matrices is covered by additional files.

All the structural input files associated to the HB format are listed hereinafter with respective functions:

1. *.intnodes*: listing of the coordinates of the nodes from the structural model;
2. *.massmatrix.mapping* and *.stiffmatrix.mapping*: these files ensure the mapping of each line of the mass and stiffness matrices with the correspondent degree of freedom of each node;
3. *massmatrix.txt* and *stiffmatrix.txt*: each file contains the mass and stiffness matrices in HB format, respectively.

In what concerns the fluid data, its grid is created using the program HEXPRESS©, an automatic unstructured mesh generator of hexahedral elements [54], and a file with extension *.grid* must be provided to the ReFRESCO simulation.

Additionally, the presence of a basic input file is also mandatory: the *controls.xml*. It contains tags in a tree like structure, listing relevant parameters to define the simulation, namely the input format of the structural data, reference values, convergence and divergence tolerances and information on what transport equations to consider and which approach to take to solve them [55].

3.1.2 FSI algorithm

With the input data covered, the algorithm of the FSI simulations can be outlined, based on the work of Jongsma and Windt [30].

As evidenced in Figure 3.1, the loads $\boldsymbol{F}$ acting on the object are initially computed, based on external forces and the loads exerted by the flow through pressure and shear stress. This is executed through interface coupling of non-identical structural and fluid grids, a subject that will be covered in Chapter 3.1.3.

Following this task, the equations of motion of the deformable model are solved. Having in consideration that the FSI module of ReFRESCO neglects the damping of the structure, one obtains from Equation 3.1:

$$[M]\ddot{\boldsymbol{x}} + [K]\boldsymbol{x} = \boldsymbol{F}, \tag{3.2}$$

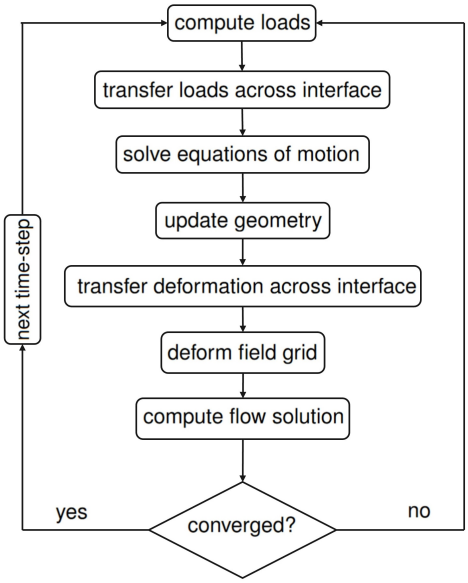

Figure 3.1: Flow chart representing one time step of a FSI simulation, from Jongsma [30].

In order to obtain the solutions of a set of these differential equations, the equation of motion 3.2 can be redefined as [31]:

$$\frac{d\boldsymbol{Q}}{dt} + [A]\boldsymbol{Q} = \begin{bmatrix} \boldsymbol{F} \\ 0 \end{bmatrix}, \text{ with } \boldsymbol{Q} = \begin{bmatrix} M\dot{x} \\ x \end{bmatrix} \text{ and } [A] = \begin{bmatrix} 0 & K \\ -M^{-1} & 0 \end{bmatrix} \tag{3.3}$$

With these Equations 3.3 established, one aims to solve them numerically in time and ReFRESCO offers three distinct solution schemes to do so: the Newmark time integration, Crank-Nicholson and the three time level scheme with second order backward-difference [31]. The three level scheme is the selected method for the FSI simulations in this case, as it generally presents better accuracy in comparison to the other available methods for computing flow behavior [56] and it has been used on other simulations similar to the ones approached on this work, such as Bronswijk [31] and Wood [57].

Considering $f(\boldsymbol{Q}, t) = \begin{bmatrix} \boldsymbol{F} \\ 0 \end{bmatrix} - A\boldsymbol{Q}$, that scheme is defined by [31]:

$$\frac{3\boldsymbol{Q}^{n+1} - 4\boldsymbol{Q}^{n} + \boldsymbol{Q}^{n-1}}{2\Delta t} = f(\boldsymbol{Q}^{n+1}, t^{n+1}) \tag{3.4}$$

Subsequently, through this method, one obtains the solutions from the equations of motion and they are used to update the vertices of the CFD mesh through, once again, fluid-structure interface coupling. Following this process, a grid deform method is applied on the field grid of the flow domain with an identical interpolation to one used on the interface. This has the intent to propagate the displacements of the interface through the fluid grid.

At last, an update for the flow solution is computed and the whole procedure is repeated until the convergence criteria defined for the flow method solution on the controls file has been met [30]. When the criteria is achieved, the process can advance to next time step, as shown on the flowchart from

Figure 3.1.

3.1.3 Interface coupling

Regarding the interface between the two domains, the coupling of fluid and structure equations is usually defined by kinematic and dynamic boundary conditions [58], given in Equations 3.5a and 3.5b.

$$\boldsymbol{u_f} = \boldsymbol{u_s} \text{ on } \Gamma \tag{3.5a}$$

$$T_s \boldsymbol{n_s} = T_f \boldsymbol{n_f} \text{ on } \Gamma, \tag{3.5b}$$

with $\boldsymbol{u}$ representing the displacements, T the stress tensor and $\boldsymbol{n}$ the outward normal of the continuous interface Γ between the structural and fluid grids. The first condition conveys equal displacements on the fluid and structure grids at Γ, while the second expresses that, on that same interface, the pressure on the fluid mesh is in equilibrium with the structural one.

In order to achieve accurate results, another condition can be added to this group: conservation of global energy over the interface. This conservative coupling approach can be written as seen on Equation 3.6.

$$\int_{\Gamma_f} \boldsymbol{u_f} \cdot T_f \boldsymbol{n_f} \, ds = \int_{\Gamma_s} \boldsymbol{u_s} \cdot T_s \boldsymbol{n_s} \, ds \tag{3.6}$$

In ReFRESCO, two approaches for interface coupling are presented that respect the Equations 3.5a and 3.5b: Radial Basis Function (RBF) Interpolation and Point Matching. While the RBF interpolation was implemented as conservative and respects the condition of Equation 3.6, the same cannot be stated for the Point Matching method, where energy in significant amounts is lost during the simulation [58], which is detrimental to the accuracy of the results of that method.

Radial Basis Function interpolation

The Radial Basis Function Interpolation transfers the quantity of a mesh A to another grid B recurring to a global interpolation function, which results from the sum of basis functions [58], as shown in Equation 3.7.

$$f_i(x) = \sum_{j=1}^{N_c} \alpha_j \psi(\|x - x_{Aj}\|) + p(x), i = A, B, \tag{3.7}$$

where to every known data point of mesh A (x_A) corresponds a distinct radial basis function in the form of $\psi(\|x - x_{jc}\|)$ and $f_i(x)$ is the interpolation function that results from their linear combination, for a set of N_c points. Additionally, $p(x)$ is a polynomial whose minimal degree is dependent on the chosen RBF function ψ [59].

In ReFRESCO, the function ψ corresponds to the C^2 function stated in Equation 3.8 [31]. It presents compact support, in which only mesh nodes inside a sphere with a defined radius r around a centre x_j

are influenced by the movement of that centre [59]. The larger r is, the more accurate the solutions will be yielded but with more dense matrix systems to solve.

$$\psi(\xi) = (1-\xi)^4(4\xi+1), \tag{3.8}$$

with $\xi = x/r$. Having defined the ψ function, the RBF interpolation can then be performed in two distinct steps, according to Jongsma [30]. Firstly, the coefficients α_j are determined by evaluating the condition on Equation 3.9 for all data points and by ensuring that the resulting system of linear equations presents positive definiteness, through Equation 3.10.

$$f_A(x_{Aj}) = F_{Aj}, j = 1, ..., N_c, \tag{3.9}$$

with F_{Aj} as the discrete values of f_A at the interface of mesh A.

$$\sum_{j=1}^{N_c} \alpha_j P(x_{Aj}) = 0, \tag{3.10}$$

where P is a polynomial with a degree less or equal than that of polynomial p [59].

The second step constitutes writing the previously stated conditions as presented on Equation 3.11 [58].

$$\begin{bmatrix} F_A \\ 0 \end{bmatrix} = \begin{bmatrix} \Phi_{AA} & Q_A \\ Q_A^T & 0 \end{bmatrix}^{-1} \begin{bmatrix} \alpha \\ \beta \end{bmatrix}, \tag{3.11}$$

where Φ_{AA} is a square matrix containing the evaluation of the basis function $\psi(\|x_{Ai} - x_{Aj}\|)$. α contains the coefficients α_j and β the coefficients of the polynomial p, while Q_A is a matrix where each row j has the form $\begin{bmatrix} 1 & x_{Aj,Bj} & y_{Aj,Bj} & z_{Aj,Bj} \end{bmatrix}$ [59].

Finally, solving this system and evaluating the matrix vector product presented in Equation 3.12, the values on mesh B (F_B) are obtained.

$$F_B = \begin{bmatrix} \Phi_{BA} & Q_B \end{bmatrix} \begin{bmatrix} \alpha \\ \beta \end{bmatrix}, \tag{3.12}$$

where Q_B takes the same form as Q_A and Φ_{BA} contains the evaluation of the basis function $\psi(\|x_{Ai} - x_{Bj}\|)$.

After obtaining the properties of the receiver mesh, in what concerns the update of the interface position, the RBF method is also assisted by the Aitken under-relaxation, with the intent of ensuring stability of the coupled system. Through this procedure, a relaxation factor is applied to the interface positions on an iterative process inside each time-step, based on the computed shape and the one from the previous and present iterations [30].

Additionally, a greedy method is applied in order to tackle computation challenges and update the interpolation. This type of algorithm makes an optimal choice for the correction of any node involved in

the RBF interpolation by targeting only the largest error of an active list of points, without considering any consequences that might outcome from that choice. The cells with higher error are then included in the next interpolation, forcing that error to zero [60].

Point matching

An alternative functionality to the RBF interpolation corresponds to Point Matching. This coupling does a Nearest Neighbour Interpolation (NNI), where the data from one mesh is directly assigned to another, depending on the distance between the donor and receiver nodes. In what concerns displacements, the value computed on the donor mesh (structural) is attributed to the closer nodes on the receiver (fluid), with the possibility of defining an interpolation factor. Regarding the loads, the reasoning is identical but the donor is the CFD grid and the receiver is the structural mesh, with the interpolation coefficient being defined based on the number of vertices connected to each cell of the interface.

3.2 FSI implementation with beam models

While the solid elements are already successfully tested on the work of Bronswijk [31] with the just described FSI algorithm, one can aim to obtain less complex computations and more mathematical simplicity on the simulations of a body like a blade of a wind turbine. In that sense, beam elements present themselves as good candidates to approximate the behavior of a model like that, as they can encompass important phenomenons that the blades may suffer and they have been used for that same goal on multiple works [23] [24] and tools, namely HAWC2 [8] and OpenFAST [9]. This possible simplification of the simulations arises nonetheless the need for compatibility of ReFRESCO with this type of elements.

When simulating the behavior of a body through a beam, the mesh of those elements corresponds to a line along which its nodes are distributed, with defined cross-sections that emulate the body's geometry. However, in order to establish the interaction between the structural and fluid grids with the RBF interpolation method, ReFRESCO uses the interface nodes on the outer surfaces of the structural mesh to transfer the displacements and loads, which poses a challenge when considering a structural grid that is situated internally to the actual body.

Therefore, when working with this type of elements, it is mandatory to mitigate this problematic, in order to achieve a proper interface coupling, whether with the Point Matching or the RBF interpolation method.

It is important to refer that, throughout this implementation, the original functioning of ReFRESCO is ensured by the creation of new variables and conditions that are not activated unless the structural model of the simulation corresponds to a beam model. Additionally, after the implementation is completed, different validation suites are tested in order to verify the correct functioning of the altered code of ReFRESCO.

3.2.1 Interface coupling

On one hand, the Point Matching method can be considered a good candidate to perform the transfer of displacements and loads directly between the beam structural mesh and the CFD grid. This coupling currently doesn't function with HB files as input and presents poor performance with ANSYS© files, having difficulty to match all the structural vertices with the CFD ones.

On the other hand, the RBF interpolation is currently the main coupling method used in ReFRESCO and it's compatible with HB input files, with validated results on numerous benchmarks. Having this in mind, if one intends to keep using this method with the beam models, it is necessary to fill in the missing nodes that establish the contact with the fluid and build a new auxiliary structural grid representing the outer surfaces of the body, as seen in Figure 3.2. The construction of this outer structural mesh is the approach taken in this work.

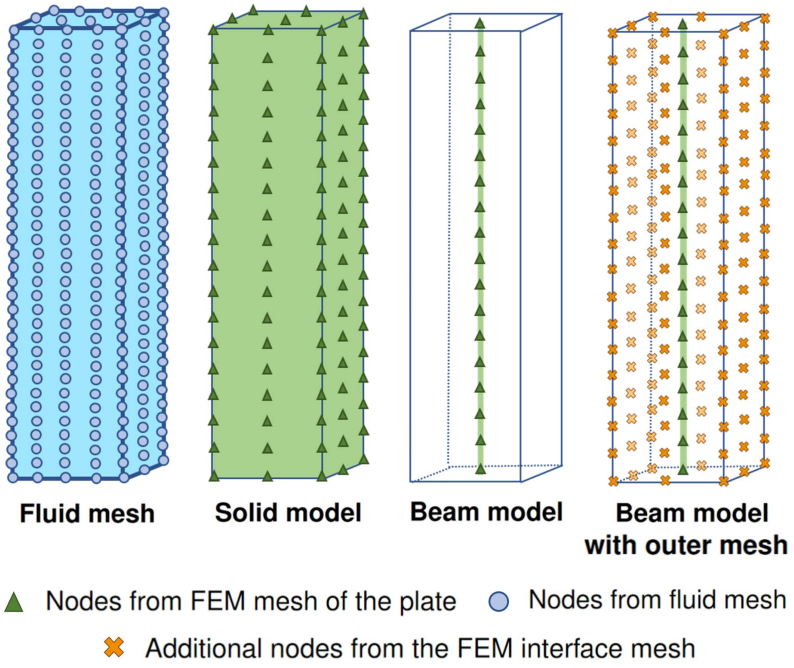

Figure 3.2: Scheme of fluid and structural grids considered to represent an example body.

3.2.2 Data input

The creation of a new outer mesh that interacts with the CFD grid requires the files already stated on Chapter 3.1.1 for the beam data, with the addition of a new structural file with the extension *.outernodes*. This file contains the number of nodes on the outer mesh, boundary conditions and a listing of the coordinates of all those points, while the file *.intnodes*, on this context, consists on a listing of the coordinates of the nodes from the beam model. A function with the goal of reading this information, concerning the outer mesh, is added to the main code of ReFRESCO and changes are made to the function that reads FEM data, in order to allocate properly the new variables of the outer mesh.

Considering that this approach requires a different functioning from ReFRESCO when dealing with its structural meshes, a new tag with logical value is also added to the listing of the *controls.xml* file:

<beamModel>. This parameter is set by default as false but, if activated, it informs ReFRESCO that the structure at hand corresponds to a beam and the simulation runs the code with the implemented changes that will be stated hereinafter.

3.2.3 FSI algorithm with beam models

Loads

The implementation of the outer mesh essentially requires further development of the structural portion of the FSI module. Similarly to the rationale stated in Chapter 3.1.2, the computed fluid mechanics forces are transferred to the structural model so they can be considered when solving the equations of motion of the body. However, in the present case, these forces are interpolated in the outer structural mesh through RBF interpolation and, afterwards, the load applied to each node of that mesh is transferred to the closest node of the beam grid. This transfer has to be implemented in ReFRESCO through changes of the main code, namely the creation of different arrays to carry the load values and the calculation of the forces applied on the beam grid. Such modifications are made on the already existent RBF interpolation function dedicated to loads transfer, as well as on the one responsible for computing the loads contribution of the fluid.

After the beam nodes receive the loads from the outer mesh, the equations of motion of the beam model can then be solved.

Degrees of freedom of rotation

As it will be further developed in Chapter 4, a beam model may include degrees of freedom of rotation on its nodes. This constitutes a challenge to overcome in the FSI module, as ReFRESCO only considers models with translational degrees of freedom, for example bodies with solid elements. Having this in mind, the option of rotations is incorporated on the HB interface function of the main code, with the possibility to include those degrees of freedom on the structural mapping files. This addition allows the linear system to compute not only displacements, but also the rotations of the nodes. However, initially, the latter results are not taken into account on the update of the geometry of the beam because only translations were considered on the original module.

Taking into account that the objects of study are linear structural models, the displacements of the nodes are specified with respect to the initial geometry of the model [30]. In order to tackle the issue of the rotations, the same train of thought is applied here, where, for each update of the geometry, the initial coordinate system is rotated with the computed angles of the previous iteration and the current displacements are applied to the new rotated system.

The values of the calculated angles from previous (θ_p) and present (θ_c) outer iterations are saved on distinct arrays and the coordinate system of each node is rotated with the matrix $[R_\theta]$ present on Equation 3.13. This matrix is directly applied to the entries of translational displacements $\tilde{\boldsymbol{r}}^{\boldsymbol{i}}$, obtaining its values $\boldsymbol{r}^{\boldsymbol{i}}$ on the rotated coordinate system, as seen in Equation 3.14.

$$[\mathbf{R}_\theta] = \begin{bmatrix} \cos\theta p_y \cos\theta p_z & \sin\theta p_x \sin\theta p_y \cos\theta p_z - \cos\theta p_x \sin\theta p_z & \cos\theta p_x \sin\theta p_y \cos\theta p_z + \sin\theta p_x \sin\theta p_z \\ \cos\theta p_y \sin\theta p_z & \sin\theta p_x \sin\theta p_y \sin\theta p_z + \cos\theta p_x \cos\theta p_z & \cos\theta p_x \sin\theta p_y \sin\theta p_z - \sin\theta p_x \cos\theta p_z \\ -\sin\theta p_y & \sin\theta p_x \cos\theta p_y & \cos\theta p_x \cos\theta p_y \end{bmatrix} \tag{3.13}$$

$$\boldsymbol{r^i} = [R_\theta]\tilde{\boldsymbol{r}}^{\boldsymbol{i}}, \tag{3.14}$$

All this process can be better understood through the flow chart in Figure 3.3, where the procedure for a single outer iteration is depicted.

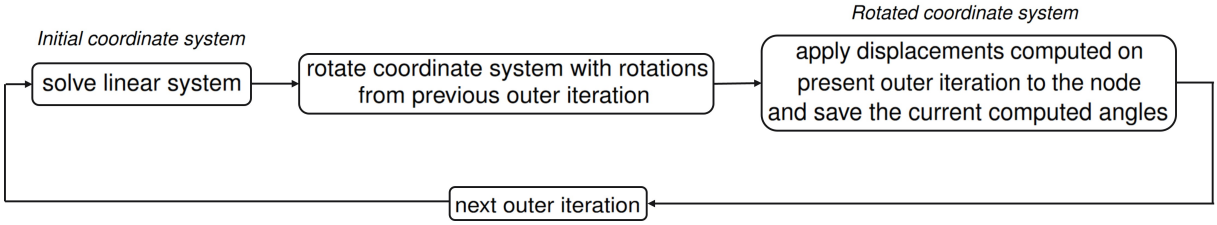

Figure 3.3: Flow chart of the process for the computed rotations at each outer iteration.

Deformation

After applying the newly computed displacements to the beam geometry, the outer structural mesh also needs to deform, as the discretised flow domain will aim to match the shape of the surface of the object. Therefore, each node of the outer mesh receives the same displacement as the one computed for the closest beam node.

While this transfer between the beam and outer structural grids is equivalent to the NNI approach used in the Point Matching coupling, it is implemented entirely inside the update interface function of the module, without resorting to that already existing coupling functionality. This decision is attributed to the intention of ensuring that all nodes are taken in account on the transfer between the structural grids, while implementing minimal changes to the overall code, as the Point Matching functions would also require extensive modification to encompass this simple transfer between structural grids.

It is also worthy mentioning that, similarly to the beam mesh, the outer grid has imposed boundary conditions stated on its input file. When implementing the current algorithm, these points with fixed degrees of freedom are taken into account by imposing null values to its displacements and loads across the entire simulation, in spite of any interaction the flow may produce.

Following this transfer between structural meshes, once again through RBF interpolation, the CFD grid is updated in the interface with the displacements from the new shape of the outer surface of the body. This process raises the need for changes on the mapping of the nodes on many functions of the main code, as this RBF transfer does not involve the grid associated to the equations of motion but an additional outer structural mesh. With the interpolation concluded, the field grid of the flow is

updated and a new flow solution is finally computed. All this process, represented on the flow chart of the Figure 3.4, repeats itself until the imposed convergence criteria or the limit number of iterations is reached. Changes are also applied to the time step function of ReFRESCO, with the intent of updating the interface position used on RBF interpolations for the next time step.

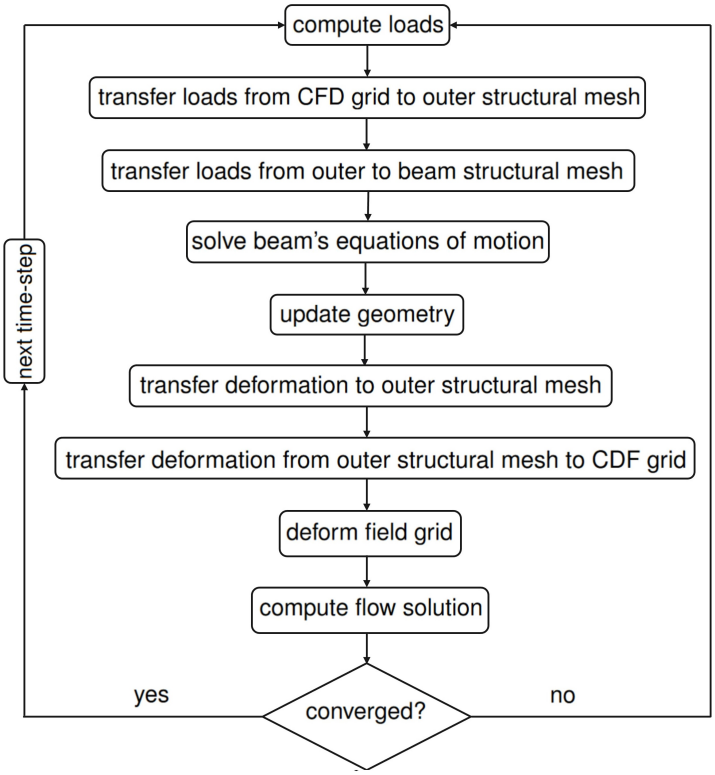

Figure 3.4: Flow chart representing one time step of an FSI simulation with a beam model.

Chapter 4

Computational Structural Beam Module

With the problematic of the beam interface introduced in the previous Chapter, the present one conveys the theoretical reasoning behind structural models with such type of elements, while also covering the implementation of a module capable of simulating the behavior of a beam, whether connected to ReFRESCO or not.

Additionally, a study on the accuracy of the developed solver is presented at the end of this Chapter, recurring to a benchmark with documented results as reference.

4.1 Beam model formulation

4.1.1 Conceptualization of the problem

As it was stated in Chapter 3, in order to solve the equations of motion, ReFRESCO receives all the structural data from ANSYS©, with the exception of the files in Harwell-Boeing format, which don't need to be provided necessarily by that software. Aiming to remove in its entirety the dependency on FEM data originated from that software, a beam solver feature can be added to complement ReFRESCO.

Having the development of this new module in mind, ANSYS© presents itself a reliable source for the formulation of the beam elements, as the module is supposed to mimic its functioning in tandem with ReFRESCO. Comprising important phenomenons when studying a blade of a wind turbine, such as axial, bending and torsion deformations, the BEAM4 corresponds to an adequate candidate to solve the problem at hand.

Taking an identical reasoning to Reddy [46], BEAM4 can be decoupled in 4 distinct models: a bar with only axial displacements, one torsion element with rotation around the x axis and two Timoshenko beam elements for the xy and xz planes. In what concerns the latter, the beam plane sections remain plane after bending, but not necessarily normal to the longitudinal axis, as transverse shear is taken into consideration [46].

From this superposition of elements, one obtains a three dimensional beam element with two nodes and six degrees of freedom on each end: three translational and three rotational, as depicted in Figure 4.1.

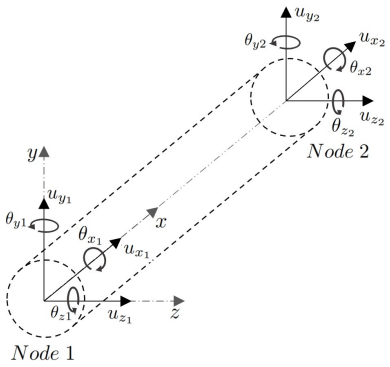

Figure 4.1: Adopted beam element in local coordinate system.

After choosing this element as reference, similarly to the work of Almeida [27], one can achieve a better understanding of the creation of the beam solver through its theoretical formulation. Therefore, with that same goal, the through-line of that formulation will hereinafter follow loosely the steps of the finite element method, already introduced in Chapter 2.

4.1.2 Strong formulation

Axial deformation

For a uniform beam with length L undergoing an axial force $p(x)$, the governing Equation is:

$$\frac{d}{dx}\left(EA\frac{du_x}{dx}\right) + p(x) = 0, \forall x \in [0, L], \tag{4.1}$$

where E is the Young's modulus of the material, A is the cross section and u_x is the displacement along the x axis [46]. This second order differential equation requires two boundary conditions in order to be solved, where displacement and load impositions can be acceptable examples: for instance, a fixed end of the beam $u_x(x1) = 0$ and a force applied on the free end $EA\frac{du_x}{dx}(x_2) = P$.

The strong formulation of the problem at hand comprises the collection of these three equations just stated.

Bending deformation

The deflection z of a Timoshenko beam suffering a distributed transverse load $q(x)$, for example on the plane xz, is governed by the following second order differential equations:

$$-\frac{d}{dx}\left[GAK_{sh}\left(\theta_y + \frac{du_z}{dx}\right)\right] + q(x) = 0, \forall x \in [0, L] \tag{4.2a}$$

$$-\frac{d}{dx}\left(EI_{yy}\frac{d\theta_y}{dx}\right) + GAK_{sh}\left(\theta_y + \frac{du_z}{dx}\right) = 0, \forall x \in [0, L], \tag{4.2b}$$

where I_{yy} denotes the area moment about the y axis of the beam, E is the Young's modulus of the material, G the shear modulus, $\theta_y(x)$ is the rotation around the y axis and K_{sh} corresponds to shear correction coefficient [46]. For a bending deformation on the plane xy, I_{yy}, θ_y and u_z turn into I_{zz}, θ_z and u_y, respectively.

The combination of these two second order differential equations demands four boundary conditions to solve a posed problem and, similarly to the axial deformation, some examples of those conditions may be fixed supports (u_z and rotations are zero) or simple ones (moments and u_z are null).

Torsion deformation

When a twisting load is applied to the beam, its free torsion behavior can be described by Equation 4.3, where J is the torsional moment of inertia, θ_x the torsion angle around the x axis and m_x corresponds to the distributed torsion load [27]:

$$\frac{d}{dx}\left(GJ\frac{d\theta_x}{dx}\right) + m_x = 0, \forall x \in [0, L], \tag{4.3}$$

Applying the same reasoning as before, the equation requires two boundary conditions, for example $\theta(0) = \theta_1$ and the moment of torsion $T(L) = T_L$.

4.1.3 Weak formulation

After establishing the strong formulation, the residual (Equations 4.1, 4.2a and 4.2b or 4.3, depending on the type of deformation) is multiplied with an arbitrary continuous function v, integrating then this product over the length of the beam. Applying this logic to all the aforementioned deformations, one obtains the Table 4.1 with respective weak formulations [46][27].

Table 4.1: Weak formulation for deformations on the chosen beam element.

Deformation	Weak formulation
Axial	$\left[EA\frac{du_x}{dx}\cdot v\right]_0^L - \int_0^L \left[EA\frac{du_x}{dx}\cdot\frac{dv}{dx} - p(x)\cdot v\right] dx = 0$ (4.4)
Bending	$-\left[GAK_{sh}\left(\theta_y + \frac{du_z}{dx}\cdot v_1\right)\right]_0^L + \int_0^L \left[\frac{dv_1}{dx}\cdot GAK_{sh}\left(\theta_y + \frac{du_z}{dx}\cdot v_1\right) + v_1 q\right] dx = 0$ (4.5a)
	$-\left[EI\frac{\theta_y}{dx}\cdot v_2\right]_0^L + \int_0^L \left[\frac{dv_2}{dx}\cdot EI\frac{d\theta_y}{dx} + v_2 GAK_{sh}\left(\theta_y + \frac{du_z}{dx}\right)\right] dx = 0$ (4.5b)
Torsion	$\left[GJ\frac{d\theta_x}{dx}\cdot v\right]_0^L - \int_0^L \left[\frac{dv}{dx}\cdot GJ\frac{d\theta_x}{dx} - vm_x\right] dx = 0$ (4.6)

4.1.4 Shape functions

Following the enunciation of the deformations the beam element suffers, one must define its shape functions, in order relate nodal and global values of the element concerning primary variables. This process, based on the documentation of ANSYS© APDL [61], is covered in Appendix A.

4.1.5 Determination of elementary matrices

Aiming to obtain the elementary matrices, the interpolation functions stated in Appendix A must be inserted into the weak formulation of the beam element, by replacing the weight functions v and the variables whose degree of freedom is at study, u or θ, depending on the type of deformation [46].

On the matrix form, the stiffness matrix of the beam element of the solver in development is presented on Equation 4.7, according to the documentation of ANSYS© [61].

$$[K^i] = \begin{bmatrix} \frac{EA}{L} & & & & & & & & & & & \\ 0 & a_z & & & & & & & & & & \\ 0 & 0 & a_y & & & & & & & & & \\ 0 & 0 & 0 & \frac{GJ}{L} & & & & & Sym & & & \\ 0 & 0 & -b_y & 0 & c_y & & & & & & & \\ 0 & b_z & 0 & 0 & 0 & c_z & & & & & & \\ -\frac{EA}{L} & 0 & 0 & 0 & 0 & 0 & \frac{EA}{L} & & & & & \\ 0 & -a_z & 0 & 0 & 0 & -b_z & 0 & a_z & & & & \\ 0 & 0 & -a_y & 0 & b_y & 0 & 0 & 0 & a_y & & & \\ 0 & 0 & 0 & -\frac{GJ}{L} & 0 & 0 & 0 & 0 & 0 & \frac{GJ}{L} & & \\ 0 & 0 & -b_y & 0 & d_y & 0 & 0 & 0 & b_y & 0 & c_y & \\ 0 & b_z & 0 & 0 & 0 & d_z & 0 & -b_z & 0 & 0 & 0 & c_z \end{bmatrix} \tag{4.7}$$

with

$$a_y = \frac{12EI_y}{L^3(1+\Phi_z)}, \qquad a_z = \frac{12EI_z}{L^3(1+\Phi_y)}, \qquad b_y = \frac{6EI_y}{L^2(1+\Phi_z)}, \qquad b_z = \frac{6EI_z}{L^2(1+\Phi_y)},$$

$$c_y = \frac{(4+\Phi_z)EI_y}{L(1+\Phi_z)}, \qquad c_z = \frac{(4+\Phi_y)EI_z}{L(1+\Phi_y)}, \qquad d_y = \frac{(2-\Phi_z)EI_y}{L(1+\Phi_z)}, \qquad d_z = \frac{(2-\Phi_y)EI_z}{L(1+\Phi_y)},$$

where the shear parameters are as follows

$$\Phi_y = \frac{12EI_z}{GA_{sh}L^2}, \qquad \Phi_z = \frac{4EI_y}{GA_{sh}L^2}, \qquad A_{sh} = \frac{A}{K_{sh}}$$

The variable A_{sh} represents the beam cross-sectional area effective in shear, where K_{sh}, already defined in Chapter 4.1.2, is obtained depending on the shape of the cross section at study.

In what concerns the mass matrix, using the same shape functions that originated the stiffness matrix, one obtains the consistent matrix from Equation 4.8 [61]:

$$[M^i] = \rho AL \begin{bmatrix} \frac{1}{3} & & & & & & & & & & & \\ 0 & a_z & & & & & & & & & & \\ 0 & 0 & a_y & & & & & & & & & \\ 0 & 0 & 0 & \frac{J_x}{3A} & & & & & Sym & & & \\ 0 & 0 & -c_y & 0 & e_y & & & & & & & \\ 0 & c_z & 0 & 0 & 0 & e_z & & & & & & \\ \frac{1}{6} & 0 & 0 & 0 & 0 & 0 & \frac{1}{3} & & & & & \\ 0 & b_z & 0 & 0 & 0 & d_z & 0 & a_z & & & & \\ 0 & 0 & b_y & 0 & -d_y & 0 & 0 & 0 & a_y & & & \\ 0 & 0 & 0 & \frac{J_x}{6A} & 0 & 0 & 0 & 0 & 0 & \frac{J_x}{3A} & & \\ 0 & 0 & d_y & 0 & f_y & 0 & 0 & 0 & c_y & 0 & e_y & \\ 0 & -d_z & 0 & 0 & 0 & f_z & 0 & -c_z & 0 & 0 & 0 & e_z \end{bmatrix} \tag{4.8}$$

with each parameter presented in Table 4.2.

Table 4.2: Mass matrix parameters of the beam solver.

$a_y = \frac{\frac{13}{35} + \frac{7}{10}\Phi_z + \frac{\Phi_z^2}{3} + \frac{6I_y}{5AL^2}}{(1+\Phi_z)^2}$	$a_z = \frac{\frac{13}{35} + \frac{7}{10}\Phi_y + \frac{\Phi_y^2}{3} + \frac{6I_z}{5AL^2}}{(1+\Phi_y)^2}$	$b_y = \frac{\frac{9}{70} + \frac{3}{10}\Phi_z + \frac{\Phi_z^2}{6} - \frac{6I_y}{5AL^2}}{(1+\Phi_z)^2}$
$b_z = \frac{\frac{9}{70} + \frac{3}{10}\Phi_y + \frac{\Phi_y^2}{6} - \frac{6I_z}{5AL^2}}{(1+\Phi_y)^2}$	$c_y = \frac{(\frac{11}{210} + \frac{11}{120}\Phi_z + \frac{\Phi_z^2}{24} + (\frac{1}{10} - \frac{\Phi_z}{2})\frac{I_y}{AL^2})L}{(1+\Phi_z)^2}$	
$c_z = \frac{(\frac{11}{210} + \frac{11}{120}\Phi_y + \frac{\Phi_y^2}{24} + (\frac{1}{10} - \frac{\Phi_y}{2})\frac{I_z}{AL^2})L}{(1+\Phi_y)^2}$	$d_y = \frac{(\frac{13}{420} + \frac{3}{40}\Phi_z + \frac{\Phi_z^2}{24} - (\frac{1}{10} - \frac{\Phi_z}{2})\frac{I_y}{AL^2})L}{(1+\Phi_z)^2}$	
$d_z = \frac{(\frac{13}{420} + \frac{3}{40}\Phi_y + \frac{\Phi_y^2}{24} - (\frac{1}{10} - \frac{\Phi_y}{2})\frac{I_z}{AL^2})L}{(1+\Phi_y)^2}$	$e_y = \frac{(\frac{1}{105} + \frac{1}{60}\Phi_z + \frac{\Phi_z^2}{120} + (\frac{2}{15} + \frac{\Phi_z}{6} + \frac{\Phi_z^2}{3})\frac{I_y}{AL^2})L^2}{(1+\Phi_z)^2}$	
$e_z = \frac{(\frac{1}{105} + \frac{1}{60}\Phi_y + \frac{\Phi_y^2}{120} + (\frac{2}{15} + \frac{\Phi_y}{6} + \frac{\Phi_y^2}{3})\frac{I_z}{AL^2})L^2}{(1+\Phi_y)^2}$	$f_y = \frac{(\frac{1}{140} + \frac{1}{60}\Phi_z + \frac{\Phi_z^2}{120} + (\frac{1}{30} + \frac{\Phi_z}{6} - \frac{\Phi_z^2}{6})\frac{I_y}{AL^2})L^2}{(1+\Phi_z)^2}$	
$f_y = \frac{(\frac{1}{140} + \frac{1}{60}\Phi_z + \frac{\Phi_z^2}{120} + (\frac{1}{30} + \frac{\Phi_z}{6} - \frac{\Phi_z^2}{6})\frac{I_y}{AL^2})L^2}{(1+\Phi_z)^2}$	$f_z = \frac{(\frac{1}{140} + \frac{1}{60}\Phi_y + \frac{\Phi_y^2}{120} + (\frac{1}{30} + \frac{\Phi_y}{6} - \frac{\Phi_y^2}{6})\frac{I_z}{AL^2})L^2}{(1+\Phi_y)^2}$	

The shear deformation parameters Φ_y and Φ_z take the same expressions presented for the stiffness matrix.

Assembly

Finally, based on the matrices computed for each element, it is possible to assemble the global stiffness and mass matrices of the model, while ensuring the interelement continuity of the variables at study. Additionally, the imposed boundary conditions must be taken into account when building these

matrices, as those degrees of freedom won't factor in on the solving of the linear equations system.

4.2 Implementation of the beam solver

With the intent of performing minimal changes to the internal code of ReFRESCO on this matter, the implemented beam solver is developed as a separate entity, through a user-coding module that, if desired, can then be interlinked with the main code when running the simulation at hand. With the premise behind its algorithm already covered, the implementation of the solver becomes the focus of this study, followed by its validation and verification.

With the beam solver development, the main goal is to remove ReFRESCO's dependency on ANSYS©. This could be achieved by supplying directly the structural deformation of the beam to ReFRESCO but it would entail further extensive modifications of the main code. Having this into account, an alternative is set: the development of a separated module from the main code, in Fortran 2005 language, where the beam solver supplies all the files that ANSYS© would for the HB input option. This reasoning is made clear by Figure 4.2, where one can assert the original functioning of ReFRESCO with ANSYS© files as input, and by Figure 4.3, where the beam solver module is implemented and raises the need for a unique file to be provided in order to run the structural portion of the FSI simulation.

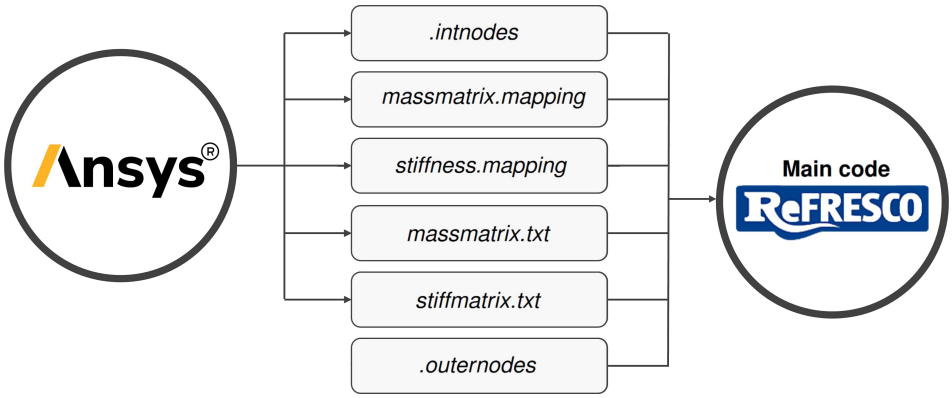

Figure 4.2: ReFRESCO functioning with structural data from a beam generated by ANSYS© as input (HB format).

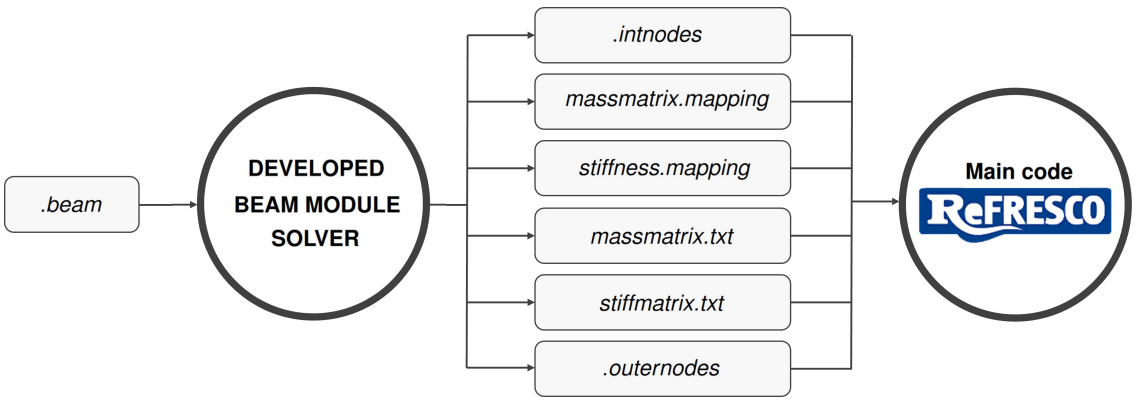

Figure 4.3: ReFRESCO functioning with structural data provided by the beam solver module as input.

4.2.1 Beam solver input data

In what concerns the aforementioned input file, it is supplied to the module through a file edited by the user, with a filename extension *beam*. Considering the HAWC2 input files as a reference and the necessary variables to solve the linear system, the input parameters for the beam solver are defined with the construction of the stiffness and mass matrices as its primal goal. Therefore, the beam element data and its geometric and material properties are required for the solver's calculations and posterior creation of the files whose functions were already mentioned in Chapter 3.1.1. The input *.beam* also comprises outernodes mesh data, which is provided exclusively to create the file *.outernodes*. All the input parameters of the file *.beam* are presented in Table 4.3.

Table 4.3: Parameters of the input file *.beam*.

Beam Element Data			
Number of elements	Coordinates of nodes for each element [m]	Orientation of local y axis in global coordinates [m]	Degrees of freedom of each node
Material		**Geometric - cross section**	
Density ρ $[kg/m^3]$ Young's modulus E $[N/m^2]$ Shear modulus G $[N/m^2]$ Poisson factor v		Area moment of inertia about y axis I_{yy} $[m^4]$ Area moment of inertia about z axis I_{zz} $[m^4]$ Torsional moment of inertia J_x $[m^4]$ Cross section area A $[m^2]$ Shear correction coefficient K_{sh}	
Outernodes Mesh Data			
Number of outernodes	Number of imposed outernodes and respective ID	Coordinates of outernodes [m]	

It is also worth mentioning that the tag <beamModel> on the *controls.xml* file must be activated on this context, as we are dealing with a beam model, which requires a different functioning when dealing with its interface coupling.

4.2.2 Model geometrical properties and limitations

When working with models of symmetrical uniform cross sections, the location of the shear centres, centroid and centre of mass are coincident and the beam model intersects these points for each considered cross section, making the computation of the geometric parameters from Table 4.3 a simple process. This is the case with the benchmark from Chapter 5.

However, when dealing with non symmetrical cross sections, the aforementioned points are not coincident. In this case, as it was approached by Almeida [27] and Tüfecki *et al.* [26], the beam should be placed inside the body it represents, aligned with its elastic axis, with all the model's rigidity concentrated along its length. According to Stodieck *et al.* [62], this constitutes a common reference axis in conventional engineering beam models, where all the loads that are applied to it produce only bending and no torsion at any station along its span. The torsion of the model is thus by the bending-torsion coupling associated to the Timoshenko element [62].

Another important aspect to consider when developing a framework with the developed module is that the formulation it is based on is only valid for beam elements with constant cross section properties.

Having in consideration the fact that the module is set to be used with a wind turbine blade where these parameters are highly variable, approximations have to be adopted to account for the non-constant spanwise properties.

Once again turning to ANSYS© documentation [61], in order to address this issue, the mass and stiffness matrices remain intact but averaged values of the two nodes composing the element are considered for its element properties, as seen in the following Equations 4.9a and 4.9b.

$$A_{av} = \frac{A_1 + \sqrt{A_1 A_2} + A_2}{3} \tag{4.9a}$$

$$I_{av} = \frac{I_1 + \sqrt[4]{I_1^3 I_2} + \sqrt{I_1 I_2} + \sqrt[4]{I_1 I_2^3} + I_2}{5} \tag{4.9b}$$

The same reasoning is applied to the mass, Young's and shear modules of each element but with a simple arithmetic mean between the values from both nodes.

4.2.3 Elementary stiffness and mass matrices computation

Having constructed a proper *.beam* input file, its data is then assimilated by the user code module when the controls of the simulation are being read on ReFRESCO, so that the entire process can take place before the structural files are demanded. The solver asserts all the elements with a length different than zero that constitute the model at hand and identifies the nodes that belong to more than one element, as repeated nodes on the listing of the mesh represent the same degrees of freedom on the matrices. With that goal in mind, a connectivity table is created, keeping track of coincident degrees of freedom from different elements and imposed boundary conditions.

The module then builds the stiffness and mass matrices for each element with the information that was previously extracted from the input file and based on the matrices that are presented in Chapter 4.1.5. Taking into account that those matrices are defined for a local coordinate system, they will need to be transformed to approach a global one, depending on the orientation of the element at study.

4.2.4 Transformation of coordinate system

It is essential when assembling the global matrix of the model to have a cohesive approach in what concerns the chosen coordinate system. Therefore, all elementary matrices, with respective displacements and forces, should refer to the same referential: the global one, as presented in Figure 4.4.

In order to change the coordinate system of an element, similarly to the reasoning presented in Chapter 3.2.3, one must apply a transformation matrix $[\Gamma^i]$, as it can be easily perceived in Equation 4.10.

$$\boldsymbol{v^i} = [\Gamma^i]\tilde{\boldsymbol{v}}^{\boldsymbol{i}}, \tag{4.10}$$

where $\boldsymbol{v^i}$ corresponds to an array of displacements and/or rotations of an element i on the global Cartesian coordinates system and $\tilde{\boldsymbol{v}}^{\boldsymbol{i}}$ on the local element one, respectively. Considering the problem at hand, the mass and stiffness need to be transformed accordingly to the global referential, which is

obtained through the Equations 4.11 and 4.12.

$$[K^i] = [\Gamma^i]^T [\tilde{K}^i][\Gamma^i], \tag{4.11}$$

$$[M^i] = [\Gamma^i]^T [\tilde{M}^i][\Gamma^i], \tag{4.12}$$

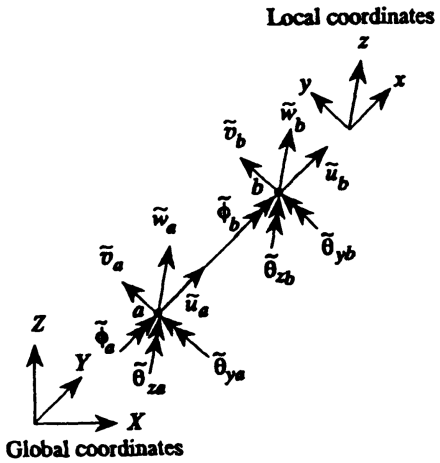

Figure 4.4: Global and local coordinates system for beam element with 12 degrees of freedom [63].

The rotation matrix $[\Gamma^i]$ can be defined by [63]:

$$[\Gamma^i] = \begin{bmatrix} \gamma & 0 & 0 & 0 \\ 0 & \gamma & 0 & 0 \\ 0 & 0 & \gamma & 0 \\ 0 & 0 & 0 & \gamma \end{bmatrix} \tag{4.13}$$

with:

$$[\gamma] = \begin{bmatrix} \cos xX & \cos xY & \cos xZ \\ \cos yX & \cos yY & \cos yZ \\ \cos zX & \cos zY & \cos zZ \end{bmatrix}, \tag{4.14}$$

where the cosines refer to angles between the direction of axes from the global and local coordinates system, presented on Figure 4.4. In the developed module, knowing the coordinates of the vectors associated to the axis at hand, these transformation matrices can be obtained through the definition of the scalar product, from which one obtains for any cosine:

$$\cos aA = \frac{a \cdot A}{\|a\|\|A\|}, \tag{4.15}$$

where $\|a\|$ and $\|A\|$ are the norms of the vectors a and A.

4.2.5 Assembly of global matrix and boundary conditions imposition

After applying the transformation of the coordinate system to each elementary matrix, one can finally assemble them into the global matrices of the model. Yet, the user has the ability to define primary boundary conditions, by stating fixed nodes through the input file *.beam*, and these must be

considered on the final assembly of the linear systems.

Currently, the solver only supports fixed nodes with all of their 6 degrees of freedom nullified, as it is deemed sufficient to simulate a clamped plate or blade on one end. Therefore, when a node is fixed, the rows and columns of the matrices associated to its 6 degrees of freedom are removed from the final assembled matrix. This is achieved thanks to the aforementioned connectivity table and an array responsible for the mapping of the unconstrained degrees of freedom of each node with the final global matrix, where only entries of free nodes are concerned.

Additionally, aiming to validate this solver, static and dynamic problems require not only these primary boundary conditions but also secondary: the loads applied on each node. While on ReFRESCO they are supplied by the fluid interaction, for solely structural simulations they need to be provided to each element through an array as the one presented in Equation 4.16.

$$\boldsymbol{F^i} = \begin{bmatrix} F_{x1} & F_{y1} & F_{z1} & M_{x1} & M_{y1} & M_{z1} & F_{x2} & F_{y2} & F_{z2} & M_{x2} & M_{y2} & M_{z2} \end{bmatrix}^T \tag{4.16}$$

Each node thus endures three components of a force F and three components of a moment M on the global coordinate system and, if constrained, those entries can be removed through the already mentioned mapping array.

It is also worthy of mention that, as presented in Table 4.3, the input file includes a list of the constrained beam and outer nodes. While the first is relevant to the solver and the mapping array, the latter serves only to inform ReFRESCO that the displacements and loads of those outer nodes must remain null during the entire simulation, as it was previously established in Chapter 3.2.3.

For a better understanding of the functioning procedure of the developed beam module, refer to the flowchart from Figure 4.5.

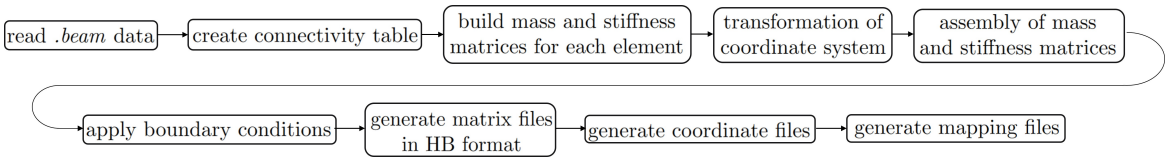

Figure 4.5: Basic steps of the beam module.

4.3 Validation and verification of beam solver

For the validation of the beam solver, De Nayer's benchmark [64] is chosen to test the module, as it has already been extensively studied on multiple works, namely from Bronswijk [31] and Lesmana [65]. It corresponds to an isotropic plate with quadrangular cross section, fixed on one end, as seen on Figure 4.6. This model is one of the focal points of this work and will be further discussed in Chapter 5, in an FSI context. For the current problematic at hand, it can serve as a reliable way of validating the beam solver, since its results can be compared with the ones from Bronswijk [31] and from ANSYS© APDL.

4.3.1 Linear static analysis

The static analysis of a beam element can be executed resorting to Equation 4.17.

$$[K]\boldsymbol{x} = \boldsymbol{F} \tag{4.17}$$

While on a FSI context the forces $\boldsymbol{F}$ come from the fluid, in the present case they are attributed by the user solely to validate the solver. For this task, a distributed load q=50 N/m is applied to the beam as represented in Figure 4.6 and the plate's properties are stated in Table 4.6. Having in account that the plate is quadrangular, the shear correction factor used on the stiffness matrix is calculated through the expression $\alpha = \frac{12+11v}{10(1+v)}$, where v is the Poisson factor [66].

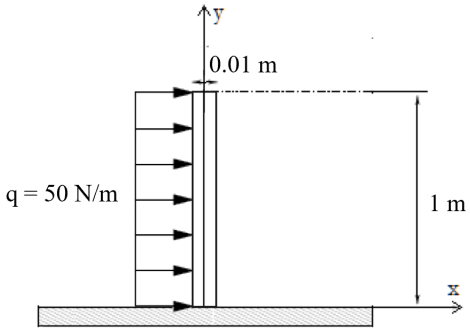

Figure 4.6: Benchmark for static analysis [65].

Table 4.4: Geometric and material properties of benchmark for static analysis.

Density, ρ $[kg/m^3]$	1200
Poisson ratio, v	0.32
Young modulus, E $[GPa]$	3.5
Area, A $[m^2]$	10^{-4}
Moment of inertia, I_{yy} $[m^4]$	$8.3 \cdot 10^{-10}$
Moment of inertia, I_{zz} $[m^4]$	$8.3 \cdot 10^{-10}$

Applying this distributed load, a convergence study can be conducted through a diverse discretization of the plate, with different sizes of beam elements composing it. From Table 4.5, it is possible to infer that, even with the change of number of elements and their aspect ratio, the beam solver is quite accurate at calculating the deformation when compared with the results from ANSYS© APDL, where the BEAM4 element was used. This is agreeable with the facts that the beam solver formulation is predominately based on the documentation of this same element.

Additionally, in Figure 4.8, one can see the deformed shape of the beam with 200 elements, where the plot generated by the beam module perfectly matches the one from ANSYS©.

Table 4.5: Convergence study of the x maximum displacement of the beam from De Nayer benchmark.

Element size y [m]	0.1	0.04	0.02	0.01	0.005	0.001
Number of elements	10	25	50	100	200	1000
Aspect ratio	10.0	4.0	2.0	1.0	0.5	0.1
ANSYS© BEAM4 [m]	0.021517	0.021517	0.021517	0.021517	0.021517	0.021517
Beam solver [m]	0.021589	0.021528	0.021520	0.021517	0.021517	0.021517
% Relative difference	0.334619	0.051122	0.013943	0.000000	0.000000	0.000000

It is also worthy of note that these values are compatible with the analytical solution calculated in Bronswijk's work [31] for a Euler-Bernoulli beam as an approximation of the plate, with no difference in regards to the maximum deflection of its tip either. Having in consideration that the solver uses the

Timoshenko model, these low deviations can be attributed to the fact that the shear deformation is negligible for the aspect ratio that the beam at study presents.

A verification study is also conducted for this analysis, recurring to the tools mentioned in Chapter 2.1.3. Through the data associated to the previously stated grids, one obtains Figure 4.7, where an estimated uncertainty of the computed values results in 0.03%. This value can be deemed quite accurate, as the fit through the data is of second order.

Aiming a thorough validation of the module, other loads are applied to the tip of the plate (y=1m), with the different testing cases listed in Table 4.6.

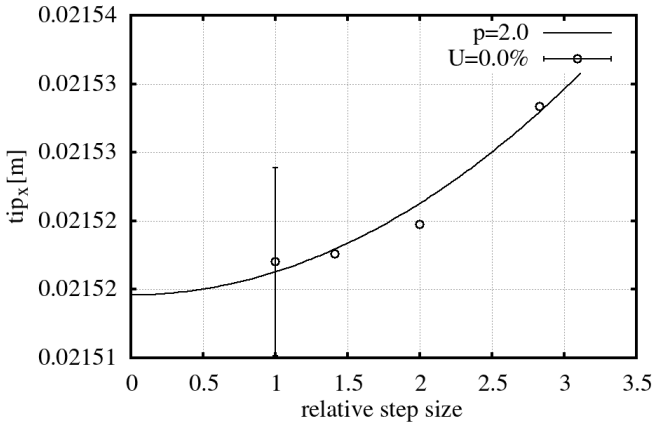

Figure 4.7: Numerical uncertainty of tip displacements in static analysis, obtained with tools developed by Eça and Hoekstra [67].

As it can be evidenced on Table 4.7, the beam solver developed for ReFRESCO once again presents highly accurate results when compared to the ones from ANSYS©, exhibiting deformations on other degrees of freedom that resulted from the different types of loads applied to the plate.

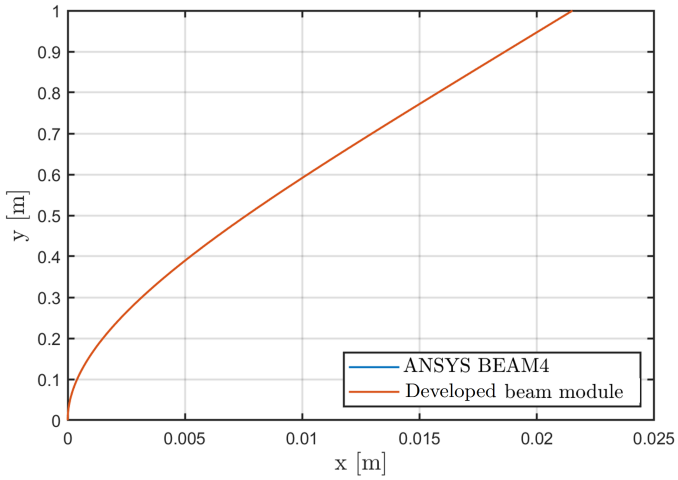

Figure 4.8: Beam horizontal deformation with 200 elements, with ANSYS© and beam solver plots.

Table 4.6: Load cases on linear static analysis of De Nayer benchmark.

Case	Load type applied at the tip of the plate (y=1m)	Value
1	F_y	10000 N
2	F_z	5 N
3	M_x	5 N/m
4	M_y	5 N/m
5	M_z	5 N/m

Table 4.7: Linear static analysis validation with 200 elements, considering ANSYS© beam elements as reference.

	Displacements and rotations	u_x [m]	u_y [m]	u_z [m]	θ_x [rad]	θ_y [rad]	θ_z [rad]
Case 1	ANSYS© BEAM4	0.00000	0.028571	0.00000	0.00000	0.00000	0.00000
	Developed beam solver	0.00000	0.028571	0.00000	0.00000	0.00000	0.00000
	% Relative difference	0.00000	0.00000	0.00000	0.00000	0.00000	0.00000
Case 2	ANSYS© BEAM4	0.00000	0.00000	0.57377	0.00000	0.00000	0.00000
	Developed beam solver	0.00000	0.00000	0.57377	0.00000	0.00000	0.00000
	% Relative difference	0.00000	0.00000	0.00000	0.00000	0.00000	0.00000
Case 3	ANSYS© BEAM4	0.00000	0.00000	0.86059	1.72117	0.00000	0.00000
	Developed beam solver	0.00000	0.00000	0.86059	1.72117	0.00000	0.00000
	% Relative difference	0.00000	0.00000	0.00000	0.00000	0.00000	0.00000
Case 4	ANSYS© BEAM4	0.00000	0.00000	0.00000	0.00000	2.27194	0.00000
	Developed beam solver	0.00000	0.00000	0.00000	0.00000	2.27194	0.00000
	% Relative difference	0.00000	0.00000	0.00000	0.00000	0.00000	0.00000
Case 5	ANSYS© BEAM4	-0.86059	0.00000	0.00000	0.00000	0.00000	1.72117
	Developed beam solver	-0.86059	0.00000	0.00000	0.00000	0.00000	1.72117
	% Relative difference	0.00000	0.00000	0.00000	0.00000	0.00000	0.00000

4.3.2 Modal linear analysis

Considering only undamped free vibrations of the body, by setting the damping and force values to zero, its equation of motion becomes:

$$[M]\ddot{\boldsymbol{x}} + [K]\boldsymbol{x} = 0 \tag{4.18}$$

Assuming a simple harmonic motion $\boldsymbol{x} = \boldsymbol{X}e^{\omega it}$ and replacing it on Equation 4.18, one obtains an eigenvalue and eigenvector problem, as presented in Equation 4.19.

$$\left([K] - \omega^2[M]\right)\boldsymbol{X} = 0 \tag{4.19}$$

A modal analysis can thus be performed and the undamped natural frequencies of a structure can be extracted from the De Nayer benchmark [64].

As one can conclude from Table 4.8, the obtained natural frequencies by the beam module are very close to the ones from ANSYS©, never surpassing an relative difference of 1%, which verifies the reliability of this solver to represent the behavior of free vibrations for beam elements.

Table 4.8: Modal analysis of plate with 200 beam elements.

Mode	ANSYS© BEAM4 [Hz]	Developed beam solver [Hz]	% Relative difference
1^{st}	2.7527	2.7531	0.0145
2^{nd}	17.232	17.245	0.0753
3^{rd}	48.172	48.250	0.162
4^{th}	94.199	94.446	0.262
5^{th}	155.37	155.90	0.340

An uncertainty analysis is performed once again, this time with the results of the modal analysis. Testing the same grids used in the convergence study of Table 4.5, the maximal uncertainty among their first modes corresponds to 0.19%, which proves a good precision of these computed results, using the different aforementioned beam mesh discretizations. The plots obtained from the uncertainty analysis, for the first three modes, are presented in Figure 4.9.

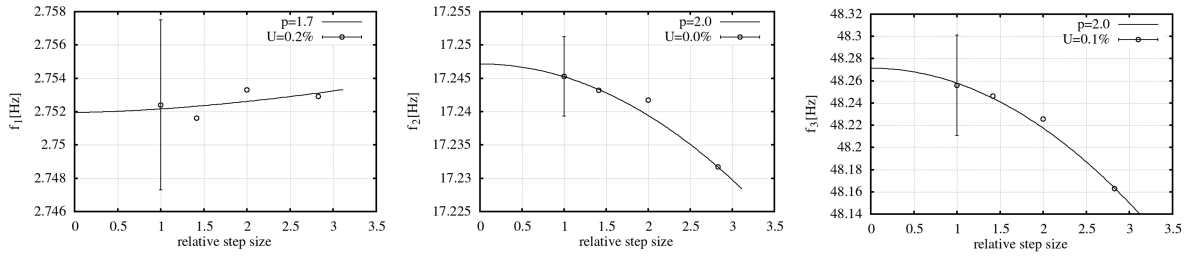

Figure 4.9: Numerical uncertainty of natural frequencies for the first (on the left), second (on the center) and third (on the right) modes, obtained with tools developed by Eça and Hoekstra [67].

Chapter 5

Benchmark case

In chapter 4, the De Nayer benchmark [64] was used with the intent of validating exclusively the implemented beam solver. In the present one, the next crucial step is taken: the validation of the interaction of beam models with a fluid grid on a FSI domain, with the structural files originated either from ANSYS© or the developed beam solver. Having this goal in mind, the current Chapter covers the steps leading up to the simulation of the De Nayer benchmark in ReFRESCO and its results, as well as some performance and sensitivity studies regarding the beam solver in a FSI context.

5.1 Case description

The benchmark case in analysis corresponds to a thin flexible plate clamped at the bottom wall boundary and located downstream of an incompressible fluid flow, with uniform inflow velocity parallel to the bottom wall.

Originally, this model corresponds to a two dimensional (2D) case but, according to Bronswijk [31], in order to simulate it with the FSI module in ReFRESCO, a depth has to be attributed to the benchmark, making it 3D. The results of this adapted model are nonetheless valid to associate to the 2D original benchmark, as the flow maintains a symmetry relative to the plane xy (refer to Figure 5.1). Therefore, considering the added depth of 0.01 meters to the De Nayer model [64], conducted in the thesis of Bronswijk [31], the plate has a quadrangular cross section with a thickness of 0.01 meters. Other dimensions concerning the domain of the simulation are presented in Figure 5.1, with the respective coordinate system.

In what concerns the fluid, it has an inlet velocity of 10 m/s, which, combined with the reference length of 1 meter and with the properties stated on Table 5.1, results in a flow with a Reynold's number of 50 and hence without significant turbulent effects [31] [64] [65] (turbulence models are not approached for the current benchmark).

The flow is associated to an open domain with a no slip boundary condition imposed on the plate body [64] and its boundary conditions are defined in Figure 5.1 and in more detail in Table 5.3. The properties of both plate and fluid domains are presented on Table 5.1.

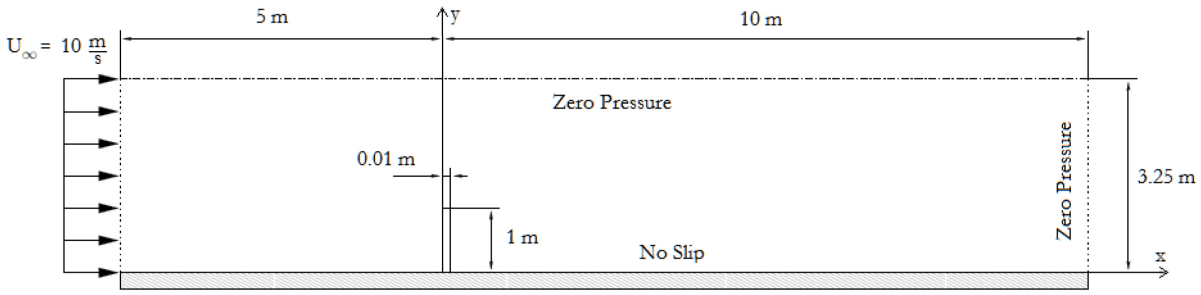

Figure 5.1: Benchmark simulation setup for clamped vertical plate [65].

Table 5.1: Properties of the plate and of the fluid domain [65].

	Fluid	**Plate**
Density, ρ $[kg/m^3]$	1	1200
Poisson ratio, υ	-	0.32
Young modulus, E $[GPa]$	-	3.5
Dynamic viscosity, μ $[Pa \cdot s]$	0.2	-
Moment of inertia, I $[m^4]$	-	8.3E-10

5.2 Structural models

Three distinct structural models representing the plate from the benchmark are simulated, as it was already referred in Chapter 1.4:

1. **Solid Model (SM)**: a reference case where the plate is represented through SOLID186 elements from the Finite Elements package ANSYS© Mechanical APDL, similarly to what was studied and validated by Bronswijk [31].

2. **Beam ANSYS© Model (BAM)**: a flexible plate with BEAM4 elements, where the structural data is originated from ANSYS© as well.

3. **Beam Solver Model (BSM)**: a flexible representation of the plate with beam elements generated by the beam solver, using a *.beam* file as input.

5.2.1 SM and BAM cases

The development of these structural models is performed in the module ANSYS© Mechanical APDL, with an output that is compatible with the RANS solver ReFRESCO. The FEM grid consists uniquely on the plate, with the clamped boundary condition on its base and with its top end free.

Considering that this structural grid is coupled in the FSI simulation with a 3D finite volume method, it must be constituted by elements that also present a three dimensional nature, in order to portray the added depth of the current benchmark. Therefore, the SM case makes use of a similar approach to the one from Bronswijk [31], where the solid elements constituted the structural model in study.

For the current model, the SOLID186 is selected to represent the plate, as it presents better results on the convergence studies [31], without compromising significantly the performance of the simulation

(Bronswijk [31] used SOLID185 ones). Each of these elements contains twenty nodes and three translational degrees of freedom in each of those nodes, presenting a capability for plasticity, large deflection and large strain scenarios [68].

In order to study a proper configuration of the elements in the model, a convergence study is executed in the same conditions as the one from Table 4.5, recurring to the tip displacements and natural frequencies of the plate as parameters. According to Reddy [46], a beam with constant flexural rigidity EI presents exact values of displacements on its nodes, for any transverse load. Therefore, for the conditions of this benchmark, the BEAM4 element constitutes an appropriate reference for the current convergence study, as it also takes into consideration shear effects and bending deformations, with the latter being a dominant phenomenon in this analysis. However, in a FSI context, the SM case is the one that will provide reference results, as a model with a similar FEM mesh has already been validated by Bronswijk [31].

Table 5.2: Convergence study of SM case, with SOLID186 elements (blue marked on the chosen discretization for the model). Reference values of BAM are concerning a model of 200 BEAM4 elements.

Element size x [m]	0.005	0.005	0.005	0.0025	0.0025
Number of elements in x	2	2	2	4	4
Element size y [m]	0.04	0.01	0.005	0.0025	0.005
Number of elements in y	25	100	200	400	200
Element size z [m]	0.005	0.005	0.005	0.0025	0.0025
Number of elements in z	2	2	2	4	4
Total number of elements	100	2000	4000	64000	16000
SM tip displacement [m]	0.021362	0.021395	0.021401	0.021406	0.021405
% Relative difference to BAM	-0.7204	-0.6181	-0.5391	-0.5159	-0.5205
SM natural frequency [Hz]	2.76308	2.76097	2.7606	2.76023	2.76031
% Relative difference to BAM	0.3771	0.2859	0.2724	0.2590	0.2619

From the convergence study presented in Table 5.2, one can conclude that the SOLID186 element does not require much refinement on the discretization of its models, as there are no deviations from the reference values superior to 1%, either regarding the displacements or the natural frequencies. Testing different mesh topologies, one concludes that the elements with an aspect ratio of 1 present the best results but do require more computational costs in an FSI context, due to their superior number of elements. For this case, aiming at achieving efficient simulations, the blue marked dimensions on Table 5.2 are chosen for the grid representing the plate in the SM case. This configuration, shown in Figure 5.2, should not compromise the accuracy of the results since its deviations on the convergence study are quite negligible.

In what concerns the BAM case, the reference beam elements from the SM case are adopted: the BEAM4. They are suitable to represent slender to moderately thick beam structures, presenting tension, compression, torsion and bending capabilities, while taking in consideration shear deformations [68]. Its formulation has already been extensively covered in Chapter 4, as well a study on the discretization of the plate model of the present benchmark with BEAM4 elements (refer to Chapter 4.3).

Finally, with the created models, the respective matrix files are created by ANSYS© APDL, as well

as a list with the nodes of the FEM grid. For the SM case, only the surface points that will be in contact with the fluid are extracted to the *.intnodes* file. These nodes belong to the faces intercepted by the midplane $z = 0.05m$, as shown in red in Figure 5.5.

For the BAM case, the *.intnodes* file provides the coordinates of the beam nodes, while the extracted points from the SM case are used for the outer structural mesh of the model in the FSI simulations.

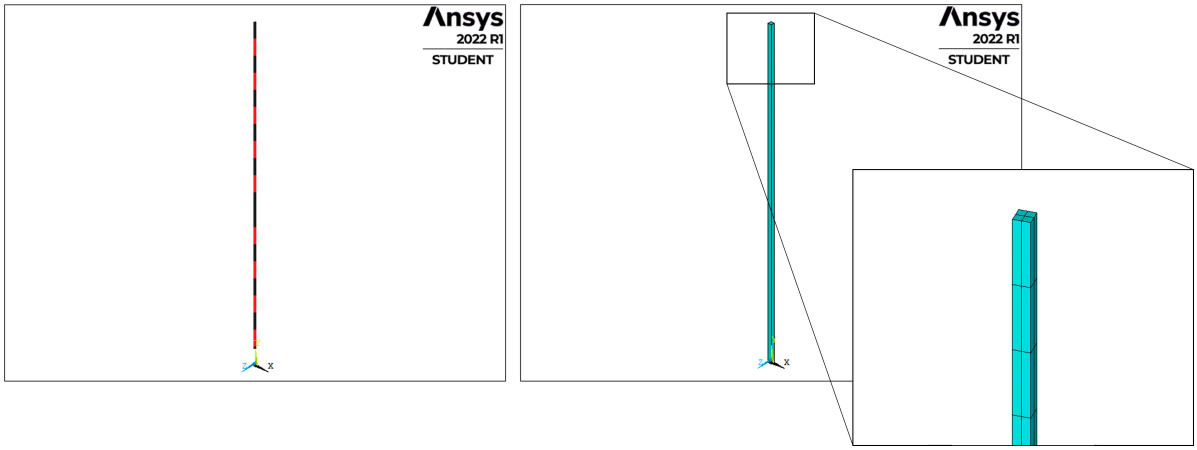

Figure 5.2: Example of a BAM case with 18 elements (on the left) and the final SM mesh (on the right).

5.2.2 BSM case

The BSM case relies on the creation of an input file *.beam* with the properties of the beam mesh and the outer structural grid that interacts with the fluid.

In what concerns the beam model itself, it doesn't require any additional calculations to obtain the properties of each element, as the plate presents no variation of its cross section properties along its length. Therefore, one only needs to apply the properties enunciated in Table 5.1 to the FEM grid. A convergence study of the resulting beam has already been carried out in Chapter 4.

Similarly to the followed proceedings in the BAM case, for the outer structural mesh, the interface nodes from the SM are used to establish the coupling between the beam and CFD grids.

5.3 Fluid model

In what concerns the fluid model, as stated in Chapter 3, its mesh is created with the program HEXPRESS©, through a script in Python language.

The dimensions of the computational domain are identical to the ones presented in Figure 5.1, with the dimension in the z direction equal to the thickness of the plate, as explained in Chapter 5.1.

When working with this benchmark, De Nayer [64] used a structured grid of 30000 cells, while Lesmana [65] and Bronswijk [31] both used an unstructured mesh consisting of approximately 16000 cells. Stemming from the grids of the latter works, a similar mesh is thus constructed in this thesis, where multiple refinement boxes are set around the plate in study, in order to reduce discretization errors of the

mesh. The final obtained grid of this work, after testing different refinements, consists on an unstructured full hexahedral mesh with 11204 cells and it is represented in Figure 5.3.

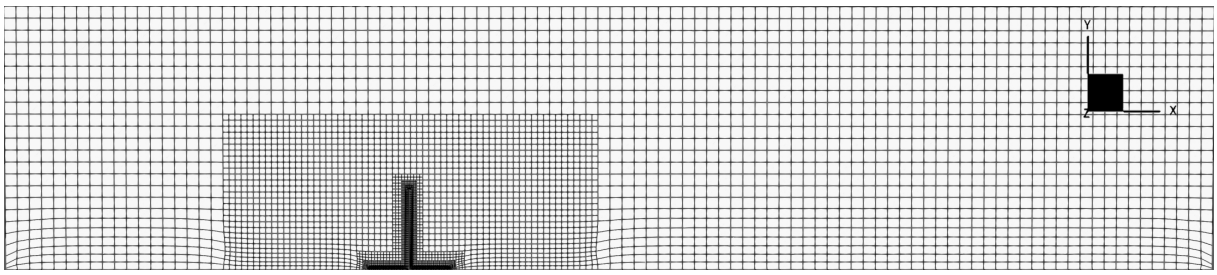

Figure 5.3: Developed benchmark grid based on the one developed in Lesmana [65] and Bronswijk [31], with multiple refinement boxes.

Its boundary conditions, defined in the settings of the simulation, are stated in Table 5.3, respecting the ones already presented in Figure 5.1.

Table 5.3: Boundary conditions of the benchmark simulation [31].

Domain Face	**Boundary condition**
Inlet	Inlet velocity of 10 m/s
Outlet	Null pressure at the boundary
Plate	Null velocity at the plate surface
Front ($z = 0.01m$)	Normal component of velocity is null on the wall and free tangential velocity
Back ($z = 0.00m$)	Mirror boundary condition of the Front
Top	Null pressure at the boundary
Bottom	Null velocity at the wall (no slip)

As mentioned in Chapter 2, the grid quality is evaluated through the non-orthogonality and eccentricity of its cells, prior to the simulation. After the completion of such simulation, the y^+ values are monitored, aiming at ensuring that the viscosity-affected region close the plate is well resolved. Additionally, a discretization error is determined for this grid in an FSI context, using the numerical uncertainty method of Eça and Hoekstra [67], mentioned in Chapter 2. The SM is used here, in order to confirm that the generated CFD grid is reliable with the already validated interface coupling and thus ensure that the beam interface coupling results are not symptomatic of the CFD mesh and the RBF interpolation uncertainties. Three identical grids with distinct cell density are then created, through changes in the Python script. Grid C1 corresponds to the original grid of 11204 cells, while C2 and C3 results from the refinement of C1 once and twice respectively. The number of elements from each grid is presented in Table 5.4, alongside the results of the discretization study in Figure 5.4.

On the x axis of Figure 5.4, the relative step sizes are presented, where 3 corresponds to the unrefined grid C1 and 2 and 1 are the meshes C2 and C3, respectively. On the y axis, the forces applied on the plate in the x coordinate are presented. These values are extracted in an equilibrium position of the plate, at t=6.0 seconds, where the results can already be approached as steady (this behavior of the plate will be further explained in this Chapter). The estimated uncertainty for the coarsest grid

corresponds to 0.08%, approximated to 0.1% in Figure 5.4, from which one can conclude that it is quite accurate. Considering this result and the increased computational costs associated to the finer grids C2 and C3, the grid C1 is the chosen one for the simulations of the benchmark.

Table 5.4: Different grids used on the numerical uncertainty study.

Grid name	Total number of cells
C1	11204
C2	76570
C3	245987

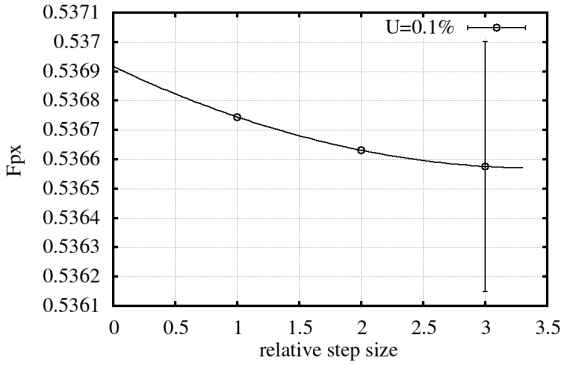

Figure 5.4: Numerical uncertainty of FSI simulation, obtained with tools developed by Eça and Hoekstra [67].

5.4 Simulation settings

As stated in Chapters 3 and 4, ReFRESCO requires for its FSI simulations the fluid and structural data of the problem at hand. Concerning the SM and BAM cases and respective structural input, one needs to provide the HB files generated by ANSYS© and the *.outernodes* file, while in the BSM case user coding is used with the *.beam*, which carries the beam properties and the beam and outer structural mesh coordinates. The tag <beamModel> is activated for both BAM and BSM cases.

Aiming the proper functioning of the RANS-FEM coupling in the simulation, one has to evaluate if there is a good agreement between the outer grid and the CFD mesh, as well as if the beam is aligned with the elastic axis of the body, which, in this case, corresponds to the center line of the plate. For a better understanding of the structural grids involved in the simulation, refer to Figure 5.5, where a scheme of the model is presented in its undeformed state.

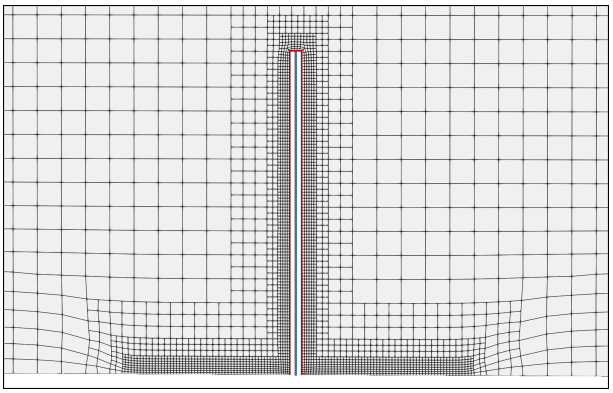

Figure 5.5: Scheme of the models from BAM and BSM simulations, with the beam grid (blue) and the outer surface mesh (red).

The FSI module has been developed for unsteady FSI problems, since the grid deform method has to solve the deformation of the fluid grid that results from the updates of the deformation of the structure, for each time step (refer to Chapter 3). Therefore, if one desires to solve steady problems, unsteady simulations have to be performed until the equilibrium is obtained. This is the case for the current benchmark, as the plate is expected to reach an equilibrium after some time, with a steady outcome [31] [64] [65].

In those unsteady computations, time discretization is executed by subdividing the simulation into a discrete number of time steps and solving it through an implicit three time level scheme. While the choice of a large time step may not capture accurately the response of the system, by "omitting" portions of the deformation in the timeline, an excessively small time step can create inaccuracy and instability of the solver. This fine balance was studied for the conditions of the current benchmark by Bronswijk [31], where the optimal chosen time step is the same as in De Nayer's [64] and Lesmana's [65] simulations: Δt = 0.01 seconds. Hence, the simulations in this work present that same time step, since it properly portrays the deformation of the plate and it's not too small of an interval, which doesn't create extreme fluctuations of pressure and, consequently, of the response forces.

For each of those time steps, the deflection of the plate will be simulated in response to the airflow of 10 m/s that is applied instantly, without a ramp function, and forces and displacements are monitored. The forces applied on the plate are calculated based on the integral of the pressure over the area of the exposed surface of the model, while the x displacement of the tip of the body is directly stored in an output file, allowing further studies on the vibrations of the plate.

Moreover, based on the parameters of Bronswijk's simulations [31], a convergence tolerance for the outer loops is set to 1.0E-5. The grid deform method uses RBF interpolation with a support radius of 0.8 meters and convergence tolerance of 1.0E-4. As developed in Chapter 3, the transfer of displacements and loads across the interface is also performed with the RBF interpolation, now with a lower support radius of 0.4 meters and a convergence tolerance of 1.0E-9.

In regards to the velocity-pressure coupling, it is achieved through a segregated mass momentum solver. For the convective flux discretization, a QUICK scheme of second order accuracy is adopted, which means the discretization error decreases four times when the grid is refined twice [31]. A QUICK scheme is also applied to the momentum solver.

5.5 Results

5.5.1 Comparison between BAM, BSM and SM cases

Tip displacements

Initially, the simulations are computed with 200 beam elements, with each element presenting a size of 0.005m along the y axis, and 421 outer structural nodes, with the dimensions of each element marked as blue on Table 5.2.

Recurring to the settings stated in Chapter 5.4, the body's movement is simulated during 10 sec-

onds, at the end of which the plate has a well defined stabilized deflection, according to the previous works on the benchmark. This is achieved thanks to the viscous damping of the motion, resultant of the interaction of the plate with the surrounding air flow. Following the tip displacements of the body, one can observe that same phenomenon, previously explored in Chapter 2, and obtain an identical plot to the one in Figure 2.5.

Having already validated the beam solver working independently from ReFRESCO, it is now essential to ascertain if the beam interface is working and if that developed beam module has a good agreement with the ANSYS© results, in a transient mode. Both evaluations are ensured by this first stage of the simulations, where the displacements of the tip of the plate are monitored, plotted and analysed for the SM, BAM and BSM cases. Those results are presented in Figure 5.6, as well as relevant points (with green squares) that are then depicted in Figure 5.7.

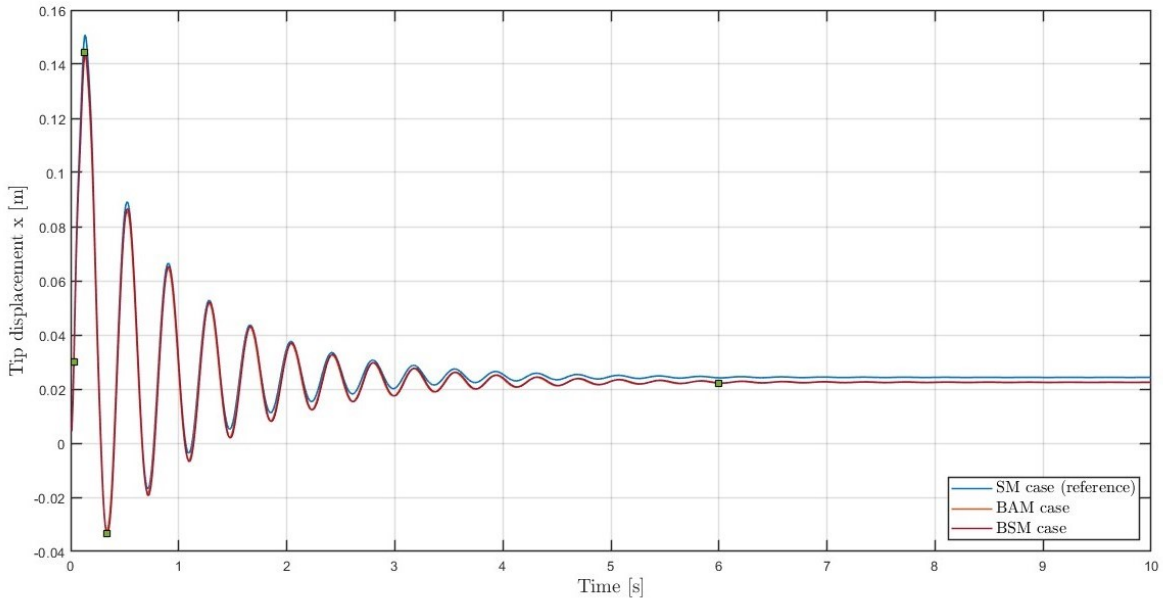

Figure 5.6: Tip displacement obtained from different models of the plate.

In what concerns the validation of the beam module in a transient context, the results of the beam solver present an excellent agreement with the ones coming from the ANSYS© generated data, as their plots in Figure 5.6 are coincident.

However, both models have slight variations from the SM reference case, that stabilizes at x= 0.0243 m, like in the other studies of the benchmark [31] [64] [65]. Comparing both beam cases with the solid one, the deviation starts in the initial instant, with a superior amplitude of the tip displacement than the one from the SM case.

It was inferred from the convergence study of Table 5.2 that the beam and solid models behave similarly when subjected to the same loads. Therefore, having into account that, initially, the mesh of the SM and the outer grid of the beam cases present the same loads on each of their nodes, the resulting difference in amplitudes between both may be attributed to the fact that the implemented beam-fluid coupling requires a better discretization from its structural grids, since its NNI method lacks in

robustness. This deviation is then propagated until the equilibrium position x= 0.0223 m is reached, with an approximate deviation of -7.1% from the reference model result.

The evolution of the plate is depicted in Figure 5.7, representing the deformation of the BSM model at distinct time steps. Firstly, at t=0.03 s, it is possible to identify a large pressure in the frontal area, where the inlet flow first collides with the body at study, and a lower pressure zone close to the other side of the plate, where a separated region of the flow appears, due to the forcing of the fluid into the corner of the body, where a singularity of the NS equations occurs [69]. This region increases its dimension, while the center of the generated vortex moves away from the plate, at t=0.13 s. Eventually, the properties of the structure and the flow become independent from time, around t=6.00 s, which yields approximately steady results.

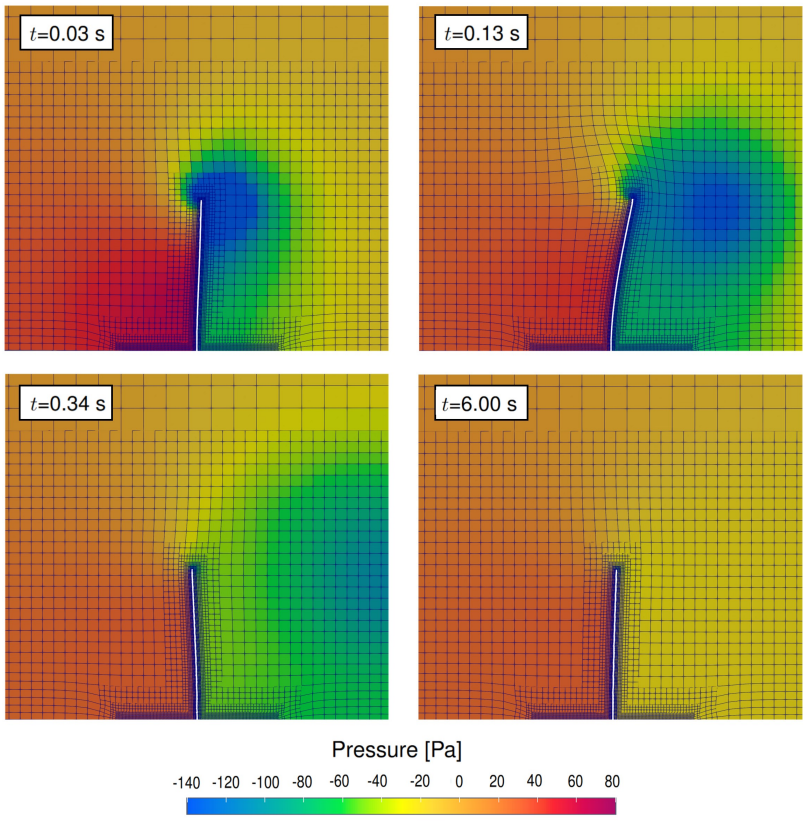

Figure 5.7: Plate response at relevant time steps, for the BSM simulation.

Response frequency and viscous damping

The plate vibrates most significantly within the first 5 seconds of the simulation, making it suitable to apply to the BSM's tip displacements a Fast Fourier Transform (FFT), with the intent of obtaining the response frequency of the body. This development is coded in Matlab© with a Hanning window, as it contains good frequency resolution and allows to perform an FFT over a non integer number of cycles [70]. Considering a time step of 0.01 seconds, the plot in Figure 5.8 is obtained, where the response frequency extracted from the marked peak corresponds to 2.73438 Hz. The SM and BAM responses

have resulted in this same frequency as well, which also matches the one obtained in Bronswijk [31].

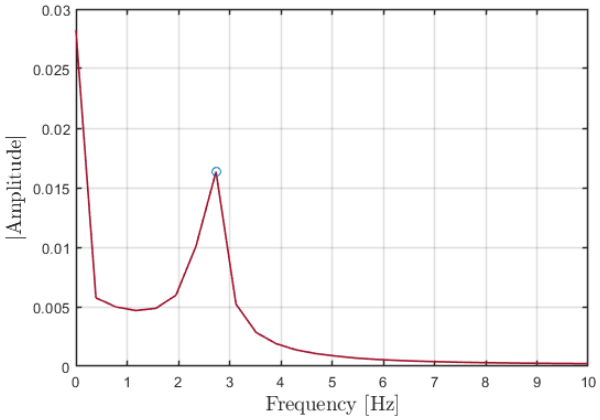

Figure 5.8: Single sided amplitude spectrum with a time step of 0.01 seconds.

Additionally, the logarithmic decrement and damping ratio are calculated in order to compare them in between the simulated models and with the ones obtained by Bronswijk [31]. The equations associated to these parameters are presented in Chapter 2 and through them it is possible to obtain Table 5.5.

Table 5.5: Logarithmic decrement and damping ratio of the response from the different models.

	Logarithmic decrement δ	Damping ratio ζ
SM case	0.125757	0.02011
BAM case	0.125887	0.02003
BSM case	0.126502	0.02013

The three models present quite similar damping ratios, which, combined with the equal response frequencies, makes clear that, in this case, the beam interface doesn't significantly affect the frequency and the damping response to the interactions with the fluid. The results' accuracy is corroborated by the identical computed values in Bronswijk's work [31], where the obtained damping ratio constitutes 0.021 (deviations from it are smaller than 5% for all the tested cases).

Performance

ReFRESCO generates multiple output files with information on the simulation process that takes place. From that data, it is possible to extract the number of outer iterations that are computed in the entire simulation, as shown in Table 5.6.

Evaluating the number of outer iterations, one concludes that the beam models are not presenting more efficiency then the SM case. In what concerns the equations of motion, the SM case has 2250 degrees of freedom (3 for each node) to solve, while the BSM and BAM cases have 1200 (6 for each

node). Considering that the solid model has to solve a higher number of equations and its stiffness and mass matrices present denser distribution in their main diagonal (see Figure 5.9), the lack of performance from the beam models should not be attributed to the solving of such equations, but to the RBF interpolation coupling between the outer mesh and the CFD grid and/or deformation of the fluid mesh after being updated in the interface with the body. As it will be inferred in the following studies, the beam interface can reach quite irregular shapes due to the NNI approach, increasing the computational costs of the simulation when compared with the solid models.

Table 5.6: Number of outer iterations for simulations of 1000 timesteps of 0.01 seconds, for the different model cases.

	Number of outer iterations
SM case	153254
BAM case	309054
BSM case	309440

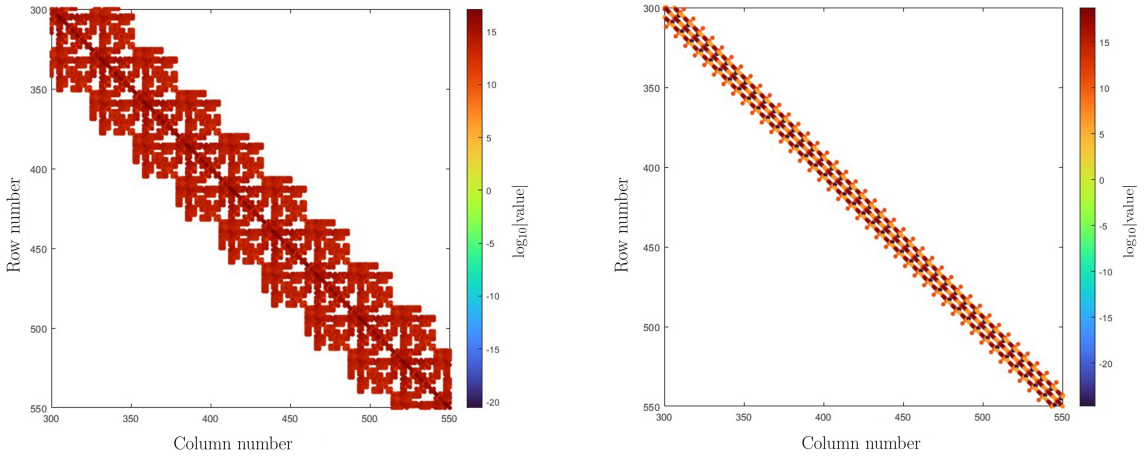

Figure 5.9: Amplified main diagonal color map of the entries distribution for stiffness matrices of the plate model, with SOLID186 (on the left) and BEAM4 elements (on the right). The mass matrices present a similar pattern. Plots obtained with altered code from MATLAB© Central File Exchange [71].

5.5.2 Rotation degrees of freedom

In order to appraise the effect of the implemented rotation degrees of freedom in the update of the interface between the body and the fluid, the initial simulation is executed without those computed rotations entering to play on the FSI coupling, for comparison purposes. The unsteady evolution of the plate is practically coincident with or without those rotations, reaching equilibrium positions with 0.3% deviations from one another. Therefore, it can be concluded that the rotation degrees of freedom are negligible for the interface update in the current benchmark and future works may focus on the reassessment of their utility for the interface update with other set ups.

5.5.3 Parametric study on structural grids discretization

From now on, the focus of this study involves solely the BSM case, as the main goal of this work is to perform the simulations without recurring to ANSYS©. A parametric study is thus performed for that test case, in order to assess how the discretization of the different meshes involved in the simulation affects the computed results. This framework also creates a precedent on how to handle the generation of the structural grids of the blades from wind turbine models.

Beam and outer grids discretization

While initially a parametric study on the beam and outer grids is executed separately, quickly it is possible to infer that the conjunction of both meshes is the preponderant factor for an accurate and efficient performance of the simulations. Having this in mind, the new generated structural grids are presented firstly, followed by an analysis on the impact of those grids on the computed results.

Starting with the beam grid, its discretization is varied, resulting on distinct models with 10, 50, 100 and 500 elements, listed in Table 5.7.

Table 5.7: Generated beam grids, with different discretization.

Beam grid	Number of beam elements	Element size y [m]
B1	50	0.020
B2	100	0.010
B3	200	0.005
B4	500	0.002

Following this process, with the intent of developing a study on the effects of the refinement of the outer mesh, new grids are created with different element dimensions, obtaining the distinct configurations presented in Table 5.8.

Table 5.8: Different outer structural grids used in this portion of the study.

Outer grid	Element size x [m]	Element size y [m]	Element size z [m]	Number of nodes
O1	0.005	0.02	0.005	257
O2	0.0025	0.02	0.0025	421
O3	0.0025	0.01	0.0025	1465
O4	0.0025	0.005	0.0025	1620

Testing the beam grids B with the different outer grids O, one obtains the Table 5.9, concerning the computed equilibrium displacements of the plate and its deviations from the reference value of the SM case. Damping ratios and response frequencies were also calculated for each test case but showed no significant changes with the alteration of the discretization of either mesh. The simulated time span for all computed simulations is 6 seconds, where equilibrium is already reached by the plate, and all the other settings remained unaltered from the initial test case.

For the same outer mesh, it is possible to verify that the increase of the refinement on the beam grid

doesn't create significant variations on the computed equilibrium displacement, without even contributing necessarily to the better accuracy of the simulations at hand.

However, these conclusions don't apply to the effects of the outer mesh discretization, as it becomes clear that this factor has a preponderant part in the accuracy of the computed solutions of the simulations. By increasing those grids' refinement, a convergence towards the reference value is observed for any selected beam mesh. This evolution culminates with the computation of an equilibrium displacement with solely 1% deviation from the reference value, achieved by the combination of the B4 and O4 grids.

Table 5.9: Displacement results of the test cases, regarding the parametric study of the beam and outer grids discretization. Marked with a cross mark are the simulations that diverged.

		Outer mesh			
		O1 (257 nodes)	**O2 (421 nodes)**	**O3 (1465 nodes)**	**O4 (1620 nodes)**
Beam mesh	**B1 (50 elements) [m]**	0.031117	0.021831	✗	✗
	Deviation from SM	28.93%	-9.54%		
	B2 (100 elements) [m]	0.031174	0.022550	✗	✗
	Deviation from SM	29.17%	-6.56%		
	B3 (200 elements) [m]	0.031136	0.022253	0.025065	✗
	Deviation from SM	29.01%	-7.797%	3.86%	
	B4 (500 elements) [m]	0.031099	0.022078	0.025217	0.02386231
	Deviation from SM	28.86%	-8.52%	4.49%	-1.13%

Nonetheless, both grids refinement must be taken into account when setting up a simulation, as they are deeply interlinked by the NNI approach taken in this work, which is why certain simulations diverged in this study. Having in consideration that the main deformation in this benchmark is due to bending, the spanwise refinement is essential to portray correctly that movement. Therefore, aiming at obtaining a better understanding of the instability in some of the computed cases, the ratio between the y dimensions of the beam and outer elements for each combination of grids is presented in Table 5.10. A pattern can thus be identified: test cases where the outer mesh is equally or more refined than the beam model (ratio equal or superior to one), in what concerns its y coordinate, tend to eventually diverge. The problem in those simulations may be attributed to the fact that the lack of discretization of the beam model in comparison with the outer one can lead to "jumps" of displacements in the interface of the body with the fluid, which creates negative volume cells in the CFD grid (refer to Figure B.1, from Appendix B). This limitation can be tackled by developing a more robust mapping system between the aforementioned meshes.

Aiming at the study of the discretization's effect on the performance of the simulations, the Table 5.11 is generated.

No clear tendency is identified in these results but it is worth noting that the refinement increase in both grids doesn't necessarily lead to a higher number of outer iterations, as it is the case with the conjunctions B4-O3 and B4-O4, in which the number of iterations are quite similar to the ones obtained in combinations with coarser grids. This is most likely explained by the fact that more regular updated

Table 5.10: Ratio between y dimensions of beam and of outer elements for the different test cases.

		Outer mesh			
		O1	O2	O3	04
Beam mesh	B1	1.0	1.0	2.0	4.0
	B2	0.5	0.5	1.0	8.0
	B3	0.25	0.25	0.5	1.0
	B4	0.25	0.25	0.20	0.40

interfaces between the outer and CFD mesh tend to form when the grids are better refined, saving thus computation costs in the structural-fluid grids' coupling (depicted in Figure B.2, from Appendix B, with a comparison between models).

Table 5.11: Number of iterations for the different computed test cases, regarding the parametric study of the beam and outer grids discretization. Marked with a cross mark are the simulations that diverged.

		Outer mesh			
		O1 (257 nodes)	**O2 (421 nodes)**	**O3 (1465 nodes)**	**O4 (1620 nodes)**
Beam mesh	**B1 (50 elements)**	250731	262747	✗	✗
	B2 (100 elements)	241000	254956	✗	✗
	B3 (200 elements)	238876	253089	246596	✗
	B4 (500 elements)	239455	309440	247417	263400

In conclusion, when working with a wind turbine in the following Chapter, the outer mesh should be highly refined if accurate results are to be obtained but one must taken into account that the beam should have a denser discretization than the outer grid, in order to avoid possible situations of divergence (the problem with the y coordinate may also occur with a wind turbine model, as the body is quite slender and bending is the expected main deformation as well [39]). This higher refinement of the meshes should not have a great impact on the performance of the simulations, since the outer iterations for the different combinations of grids were quite similar in this benchmark.

Chapter 6

DTU 10MW Turbine

This Chapter is centered around two distinct simulations of the full-scale DTU 10MW RWT. The first considers the rotor as a rigid body, without deformation, while the second focuses on a flexible blade, where the FSI module of ReFRESCO is used in tandem with the developed beam solver.

6.1 Case description

The DTU 10MW RWT corresponds to a horizontal axis wind turbine, whose geometry and operational specifications are presented in Table 6.1. For the purposes of this work, following the same methodology of Hsu and Bazilevs [17] and Yu and Kwon [18], solely the RNA of the turbine at full scale is studied, as one only intends to verify the deformation of a blade of the rotor with the developed beam solver and the beam interface coupling. Additional information on the aerodynamics properties of this case are also stated in Table 6.1, where the chosen temperature of the air is 14℃, which is within the usual operational range of temperatures of offshore wind turbines [72]. Regarding the calculation of the Reynolds number, based on the methodology adopted in the work of Make and Vaz [38], it is obtained at 70% of the blade span, using as a reference length the airfoil's chord, $c_{0.7}$, and as reference velocity the relative velocity of the flow at that spatial point (vector sum of the inlet velocity and the rotation of the blade).

Table 6.1: Case key parameters (geometry properties extracted from Ostachowicz *et al.* [1]).

Geometry		Operation Conditions		Aerodynamics properties	
Number of blades	3	Rated power $[MW]$	10	$\mu_{14℃,1atm}$ $[Pa \cdot s]$ [73]	1.789E-5
Rotor Diameter $[m]$	178.3	Rated wind speed $[m/s]$	11.40	$\rho_{14℃,1atm}$ $[kg/m^3]$ [73]	1.225
Hub diameter $[m]$	5.6	Rated tip speed $[m/s]$	90	Reynolds number $Re_{c0.7}$	1.832E7
		Tip speed ratio TSR	7.50	$c_{0.7}$ $[m]$	4.392
		Angular speed ω $[rads^{-}1]$	0.959		

6.2 Fluid model

In what concerns the fluid model, as stated in Chapter 2.1.2, two methods are tested in the approaching of the fluid domain. On one hand, Sliding Grids are considered, as they can set a basis for future work with rotor-tower interactions. Having this in mind, two sub-domains are created: one of them constitutes a cylinder encompassing the RNA, while the other is a cylinder with a hole where the first sub-domain fits, as shown in Figure 6.2. On the other hand, the AFM approach has been taken in a multitude of simulations of the rotor of FOWTs [38][74][75], creating an interesting opportunity to establish comparisons with works involving the DTU 10 MW RWT and with the computed simulations using the SG.

The geometry of the three blade RNA is generated in HEXPRESS©, from a supplied file by MARIN that contained a unique blade and a hub. The generated domain dimensions are based on the methodology followed by Make [74] with the NREL 5MW model and later by Castro [75] with the DTU 10 MW one, both using the AFM approach. Having this in mind, the domain presented in Figure 6.1 is created, similarly to Castro's [75] set up. Based on the work of Leble and Barakos [39], the chosen dimensions for that grid should also be applicable to the SG, with the addition of the interface, represented by the dotted lines in that same Figure.

The generated grids must have enough upstream length, in order to ensure that the numerical perturbations from the inlet are able to dissipate before reaching the rotor, while also guaranteeing that the rotor does not influence the inlet flow. Enough downstream length must also be set, so that the wake is able to develop, reaching a near zero gradient flow at the outlet. Finally, the domain should also be wide enough, in order to warrant the use of the approximation of undisturbed flow on the sides, with null pressure. Regarding the BC in the interfaces of the SG, these are not too close to the RNA geometry in order to achieve lower gradients, with which they perform better.

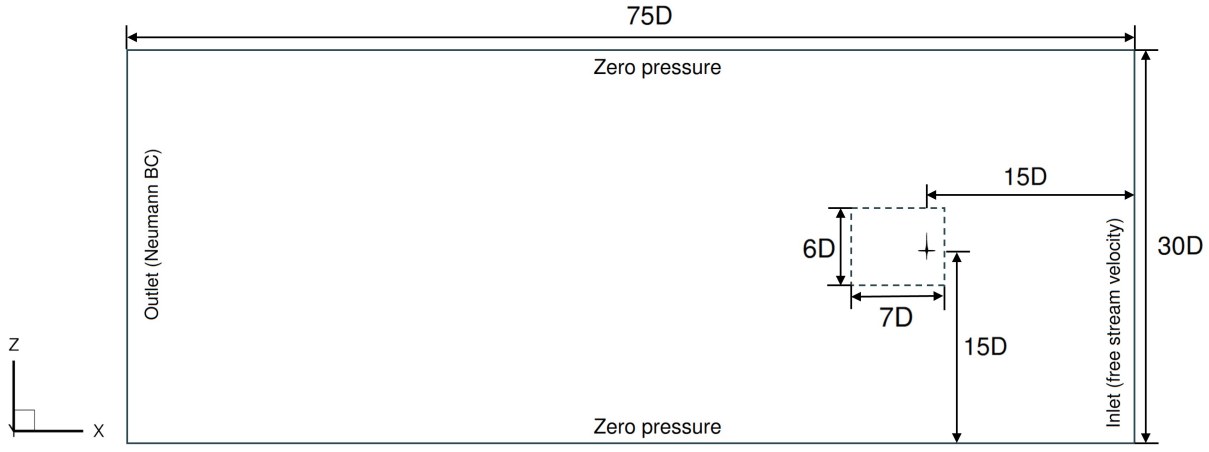

Figure 6.1: DTU 10MW RWT domain setup for the fluid grids (rotor not at scale). The AFM grid does not have an interface between sub-domains, while the SG do, which is represented by the dotted lines.

In what concerns the imposed boundary conditions of the problem at hand, in both grids, a movement of rotation without translation of the rotor is simulated. Regarding the SG, the body has a purely

rotational motion, in tandem with the sub-domain that encompasses it, and establishes a sliding interface with the external sub-domain. Considering the AFM approach, as stated in Chapter 2, the RNA is static and its rotation is portrayed through additional Right-Hand Side (RHS) terms that are added to the momentum equations.

For both grids, the blades and hub also present a no-slip boundary condition with zero velocity at the wall. The pressure is set to zero on the sides of the domain and, in the outlet, a Neumann type BC is established with the derivatives there set to zero. These boundary conditions are also presented in Figure 6.1.

In regards to the meshes themselves, the SG is the first one to be generated. Initially, already combining the two sub-domains, it is constructed with approximately 13 million cells. This mesh makes use of an HEXPRESS© tool that defines the target y^+ when introducing the viscous layer to the model, providing an adequate chance of solving of the boundary layer. Nevertheless, the computational costs associated to this grid are far too high for the testing of the flexible model with just one processor, since the beam solver is not parallelised. Aiming at reducing the number of cells of the generated unstructured mesh, wall functions are used to approximate the BL, instead of relying on the grid refinement near the wall. This approach considerably decreases the total number of cells to approximately 3.1 million.

Finally, with the AFM approach, a specific refinement to the BL is also not carried out, which leads to a mesh of approximately 3.1 million cells as well. The number of cells of each of these generated domains is stated in Table 6.2, while in Figures 6.2 and 6.3 the SG with less refinement and the AFM mesh are presented. For a more detailed view of the AFM mesh refer to the Appendix C.1.1

Table 6.2: Number of cells of the CFD grids used in the rigid simulations.

Fluid mesh		**Number of cells**	
SG with refinement of the BL	Inner sub-domain	13 594 473	13 679 624
	Sub-domain with hole	85 151	
SG without refinement of the BL	Inner sub-domain	3 107 814	3 192 965
	Sub-domain with hole	85 151	
AFM without refinement of the BL		3 185 555	

6.3 Rigid blade

6.3.1 Simulation settings

The selected inlet velocity for all simulations corresponds to the rated wind speed of the turbine, 11.4 m/s. This parameter constitutes the wind speed at which the maximum output power of the turbine is first reached [76]. In what concerns the rotation velocity of the rotor, the value of -0.959 rad/s, relative to the x axis, is selected. This number fits in between the minimum and maximal rotor speeds, with a TSR of 7.5, and provides reference results from Castro [75], since the same speed is used in his work.

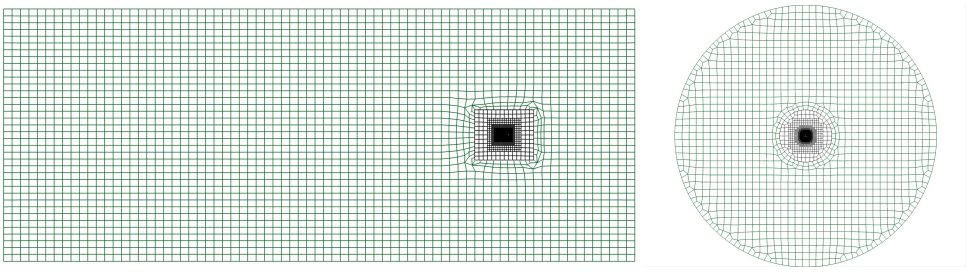

Figure 6.2: DTU 10 MW RWT Sliding Grids configuration without significant refinement of the BL: front and side view. The outer sub-domain is represented in green color, while the inner is in black.

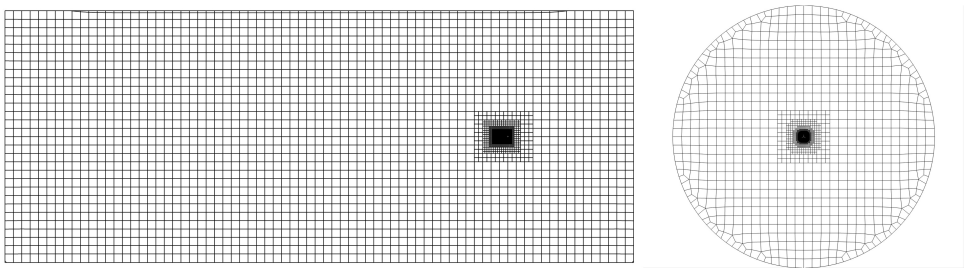

Figure 6.3: DTU 10 MW RWT grid, through the AFM approach.

Concerning the time discretization of the unsteady simulations, the implicit Euler scheme, of first order accuracy, is selected for stability reasons. This leads to the choice of an appropriate time step, which, in simulations with wind turbine models, is usually defined by evaluating the angular displacement of the rotor per selected interval of time [35], considering the angular speed of the RNA constant. Based on the literature review executed on this topic [35][40][75], simulations with wind turbines tend to use time step values that cover a rotation bellow $10°$ per time step. Having in account the established operation conditions for this test case in Table 6.1, specifically the angular speed of the rotor, a time step of 0.145596 seconds is selected, since the RNA would rotate approximately $8°$ per time step.

Moreover, differently from the benchmark case, turbulence is accounted for the wind turbine study. As already referenced in Chapter 5, the adopted turbulence model is the $k - \sqrt{k}L$ one, which was found to be more stable in comparison with other alternatives offered by ReFRESCO, when simulating wind turbine models [35]. In regards to the discretization of the convective fluxes, the second order accuracy scheme Limited QUICK is once again adopted. The same values for convergence tolerance from the benchmark in the outer loops are selected here, as well as similar approaches on the mass-momentum and the momentum solvers.

6.3.2 Results

Displaying the velocity field around the model with Tecplot©, the left plot of Figure 6.4 is obtained from the rigid simulation recurring to SG with less refinement. This distribution of velocity is identical to the one obtained by Castro [75], who simulated the same turbine at the exact same operating conditions. As expected, there is a wind speed drop after the geometry, due to the extraction of the kinetic energy of the flow by the rotor, making it expand. While on the pressure side of the blade there is no separation

of the flow and no very significant 3D effects (refer to Appendix C.1.1), observing the friction streamlines of the suction side, from the other plot of Figure 6.4, it is possible to identify small recirculations phenomenons near the blade trailing edges at low span range, already identified in this model by Zahle *et al.* [77] and Horcas *et al.* [1]. Some minor vorticity is also observed close to the tip of the blades and to the hub itself, in the Figure presented on Appendix C.1.1.

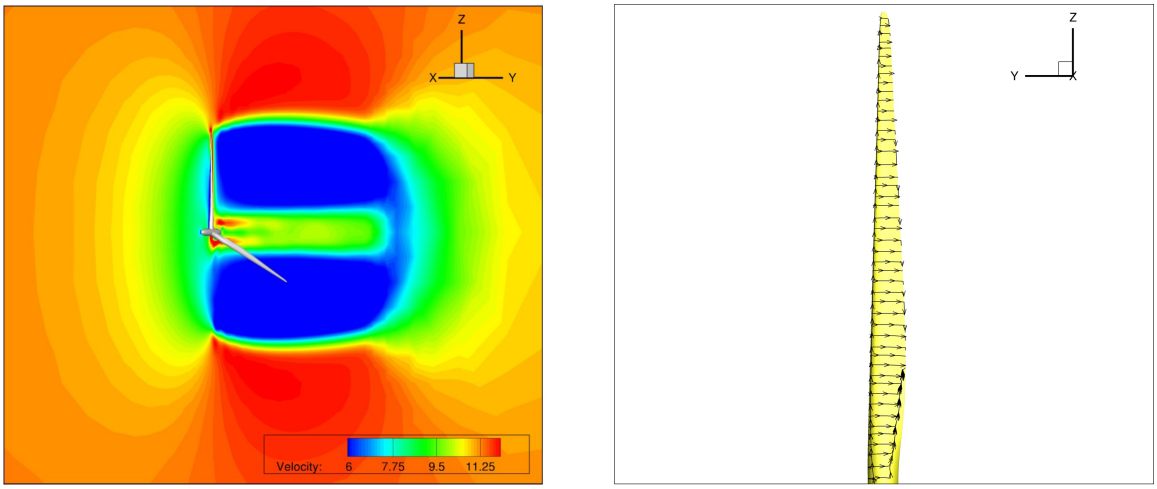

Figure 6.4: Velocity field of the flow around the RNA model of DTU 10MW RWT (on the left) and friction streamlines in the suction side of the blade, at rated speed (on the right).

Aiming at evaluating the discretization error introduced by the fluid grid without expensive Verification and Validation studies that depend on further simulations with other grid refinements, relevant parameters are produced in this Chapter and compared once again with the outcome of the simulations of Castro [75], who tested the model with both ReFRESCO and OpenFAST [9], obtaining identical results in both software.

Firstly, the thrust (F_x) and power ($M_x\omega$) in the axial direction, created by the pressure and friction forces, are extracted from monitoring files of ReFRESCO, rendering the plots from Figure 6.5.

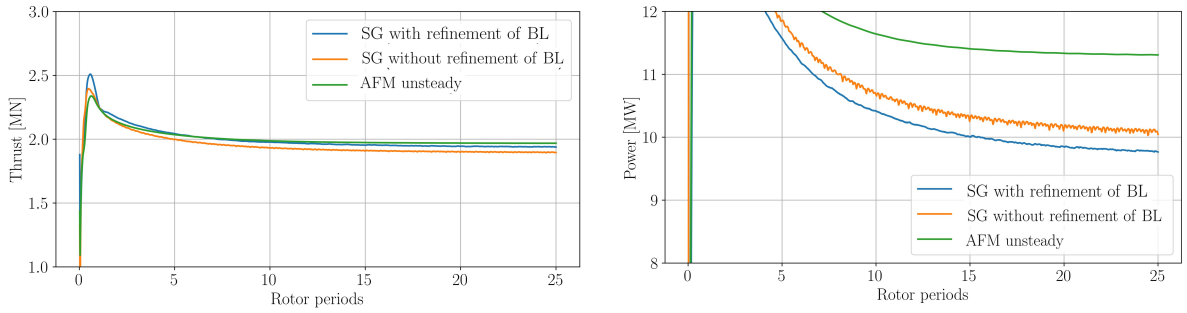

Figure 6.5: Thrust and power computed for the RNA model, with and without significant refinement of the boundary layer.

Through the analysis of these results, the differences between the values originated from the SG with and without refinement of the boundary layer are quite noticeable and the probable leading cause of this constitutes the obtained high values of y^+. As stated in Chapter 6.3.1, wall functions were used to approximate the boundary layer with less refinement but the obtained average of y^+=2228.279

for that grid even exceeds the applicability limits of those functions [35], which most likely leads to a deficient portrayal of the BL with that discretization. Yet, it is important to note that the average thrust and power computed values with that model, 1.90 MN and 10.10 MW respectively, remain in good agreement with ones obtained by Castro [75], where the results are approximately 1.80 MN and 10.0 MW (deviations do not exceed 6%). Therefore, one may conclude that the created set up for the SG, with all its simplifications, doesn't lead to too large differences from the expected results, considering the purposes of these work. Concerning the AFM results, even though it also relies on wall functions to model the BL, it was clearly the most unreliable method, with an averaged thrust of 1.97 MN and power of 11.31 MW, which leads to deviations of 9.4% and 13.1% from the Castro's [75] values, respectively.

Afterwards, the thrust C_T and power C_P coefficients are calculated, based on Equations 6.1a and 6.1b [38].

$$C_T = \frac{F_x}{1/2\rho v_w^3 \pi R^2}, \tag{6.1a}$$

$$C_P = \frac{M_x \omega}{1/2\rho v_w^3 \pi R^2}, \tag{6.1b}$$

with v_w as the inlet wind speed and R as the turbine radius. The resulting plots are depicted in Figure 6.6.

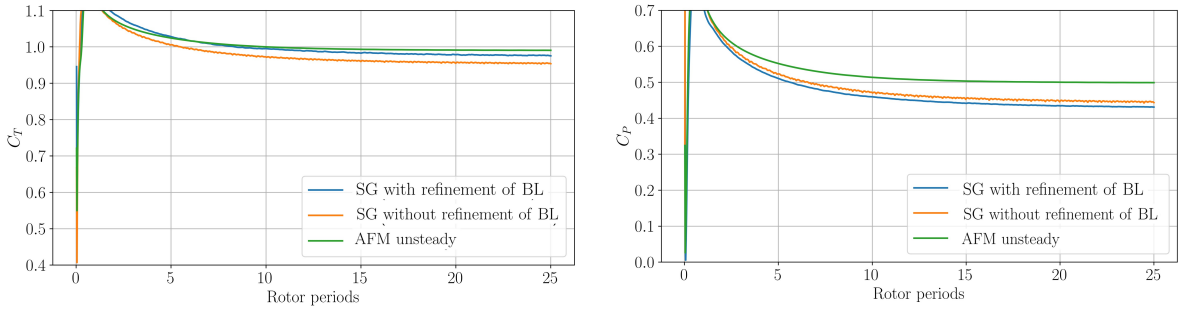

Figure 6.6: C_T and C_P computed for the RNA model,with and without refinement near the wall to capture the BL.

Observing both plots, the AFM simulation presents, as expected based on the aforementioned results, the major deviations from Castro's results (where C_P=0.47 and C_T=0.90, approximately). The attained averages for those parameters in the aforementioned simulation are C_P=0.499 and C_T=0.991.

In the case of the SG, the lack of discretization near the wall doesn't greatly affect these coefficients, since they are quite similar to the ones from the mesh with better refinement close to the wall. Its values, C_P=0.446 and C_T=0.955, don't present large differences from Castro's results [75] either, with deviations not exceeding 7%.

In Lee *et al.* [78], studies were conducted concerning the effects of high y^+ on the results of torque and thrust of a wind turbine blade, simulated with SG. Facing a deficiently solved boundary layer, turbulence models were deemed quite sensitive to grid changes, specially in regards to the computed torques (C_P and power). This fact may corroborate the oscillatory behavior that the results present for both those parameters in the SG with less refinement.

Table 6.3 lists the computed parameters of each simulation, once again with the results of Castro's study [75] as a reference.

Table 6.3: Key parameters computed in the rigid simulations.

Fluid mesh	Thrust [MN]	Deviation from [75]	C_T	Deviation from [75]	Power [MW]	Deviation from [75]	C_P	Deviation from [75]
SG with refinement of the BL	1.94	7.77%	0.977	8.56%	9.78	-2.20%	0.432	-8.09%
SG without refinement of the BL	1.90	5.55%	0.955	6.11%	10.10	1.00%	0.446	-5.11%
AFM without refinement of the BL	1.97	9.44%	0.991	10.11%	11.31	13.1%	0.499	6.17%

From this study, it is possible to conclude that the three grids can be used in a flexible simulation, depending on the intended goal. If one intends higher accuracy but also high computational costs, the SG with more refinement in the BL should be selected. If the opposite is desired, with preference for efficiency over accuracy without compromising too much the results, then the SG with less refinement should be adopted, as the AFM unsteady simulations yielded more significant errors for a similar discretization.

6.4 Flexible blade

In what concerns the flexible simulation, the fluid grid developed for the rigid model is the same. What differs however is the presence of a structural body, vulnerable to deformation. Therefore, a structural model has to be developed, in order to account for the geometry's deflections and rotations, as proceeded in Chapter 5.

6.4.1 Structural model

Beam grid

Following the Hsu and Bazilevs' approach [17], only one of the blades of the RNA is deemed flexible, with the other two remaining rigid. While the results of the flow interaction with the rotor may not be as accurate as in the case in which the three blades are passive of deformation, computational costs are smaller and it would be enough to evaluate the developed tools when working with flexible blades.

The DTU 10 MW RWT has its geometry well documented and publicly available[1]. Based on the aeroelastic data provided by an input file for HAWC2 [8], it is possible to extract the material and geometrical properties of a blade from its rotor, in 50 different cross sections. Stemming from the work of Tüfecki *et al.* [26], these discrete properties are made continuous through a curve-fitting of the data in Matlab©. The functions used in this process can be consulted in Appendix C.1.2.

[1] `https://rwt.windenergy.dtu.dk/dtu10mw/dtu-10mw-rw`

From those functions, it is now possible to extract material and geometric properties for any cross section across the blade's length, allowing a better refinement of the structure.

However, some caution is necessary when approaching this data, as its parameters must match the *.beam* file's requirements. The moments of inertia from the aeroelastic documentation are relative to the principal bending axes of each cross section, with their origin in a point where radial forces (in the z direction) do not contribute to the bending around the x or y directions [79]. Therefore, the orientation of those axes has to be supplied to the developed beam module through the input of the orientation of the local y axis for each element. Additionally, these moments of inertia need to be transferred to the shear center, where the beam nodes are located in each defined cross section. This is performed through the parallel-axis theorem, stated in Equations 6.2a and 6.2b.

$$I_x^{sc} = I_x^{H2} - A \cdot \xi_y, \tag{6.2a}$$

$$I_y^{sc} = I_y^{H2} - A \cdot \xi_x, \tag{6.2b}$$

where I^{H2} is the inertia moment extracted from the HAWC2 file, I^{sc} is the inertia moment relative to a parallel axis passing in the shear center and ξ corresponds to the perpendicular distance between the axes from the different coordinate systems. Having in account that the cross sections of a blade and its properties are non constant, the nodal values also need to be averaged as stated in Chapter 4.2.2, in order to introduce in the beam solver the properties concerning the elements, not the nodes.

Grounded on the conclusions reached in the previous Chapter, a highly refined mesh is thus constructed with 800 elements, each with a dimension of 0.111 meters approximately. A modal analysis is then conducted with this new model, in order to compare the computed frequencies with the results from the reference aeroelastic tool HAWC2, which carries in its installation folder the reference geometry of the DTU 10 MW RWT blade.

The computed results, presented in Table 6.4, have a reasonable agreement with the values calculated in HAWC2, presenting more significant deviations for the second and third flapwise bending modes. A possible explanation for the computed errors is a deficient calculation of the shear center coordinates of the cross sections associated to each node, since that data was provided in function of the location of the center line, that is, a straight line that unites points at the half chord of each considered cross-section. The lack of discretization of these center lines, in comparison with the 50 available cross sections of the blade, may have led to errors in the computation of the variables that are dependent on it. Nevertheless, this model should still be able to portray fairly well the behavior of the DTU 10 MW RWT blade in an FSI simulation.

The positioning of the beam grid inside the blade's geometry is performed by making the tips of both models coincide and verifying if the areas of the geometry's cross sections and the area values that formulated the beam model are similar, for xy planes intercepting the beam nodes. Having ensured this condition, the beam should be able to properly represent the body of the blade, in the coordinate system shown in Figure 6.7, which is consistent with one used in the rigid body simulations.

Table 6.4: Modal analysis of blade model of DTU 10 MW RWT, using the developed beam solver, with HAWC2 results as reference.

Mode	**Developed Beam Solver [Hz]**	**HAWC2 [Hz]**	**Relative difference**	Mode type
1^{st}	0.6286	0.613	2.55%	Flapwise bending
2^{nd}	0.9128	0.932	-2.06	Edgewise bending
3^{rd}	1.6003	1.741	-8.08%	Flapwise bending
4^{th}	2.9090	2.763	5.28%	Edgewise bending
5^{th}	3.2277	3.575	-9.71%	Flapwise bending
6^{th}	5.656	5.696	-0.70%	Coupled flapwise-edgewise bending
7^{th}	6.1808	6.115	1.08%	Torsional

Outer grid

The outer structural mesh is created based on the geometry provided by MARIN, from which it is possible to extract multiple cross sections and its points' coordinates through Rhinoceros3D©. These cross sections are chosen to be adopted as the outer mesh of the model, based on other works with flexible blades, in which the exchange of displacements and loads is performed between the beam and defined cross sections' points [18] [22]. In Figure 6.7, both final structural grids are depicted, with the beam mesh presenting a better refinement than the outer mesh in the spanwise direction.

6.4.2 Simulation settings

In regards to the simulation itself, the same settings as the ones from the rigid cases are adopted, with the addition of parameters concerning the methods associated to the FSI module. The convergence criterion is also generally broadened, aiming to reduce the number of total outer iterations, which is a critical factor for the computing of relevant results at a faster time. For that effect, a convergence tolerance for the outer loops is set to 1.0E-4 for all variables. The RBF interpolation in the grid deform method adopts a support radius of 0.5 meters and a convergence tolerance of 1.0E-4. The transfer of displacements and loads across the outer mesh-fluid interface is performed with a support radius of 0.4 meters and a convergence tolerance of 1.0E-6 in its RBF interpolation. Although these tolerance values are superior to the ones set in the benchmark simulation, the maximum iterations of these processes also have to be increased, in order to ensure that the coupling between the structural and fluid grids is allowed to converge. The number of outer loops is limited to 1500, while the number of deformation iterations is limited to 10 000 with a convergence tolerance of 1.0E-6.

Figure 6.7: Beam grid (in yellow) and outer mesh (white dots) used for the conception of the structural model of the rotor's blade of the DTU 10 MW. Images extracted with Rhinoceros3D©.

Additionally, in an attempt to reduce the number of time steps to reach an approximately steady motion of the rotor, the rigid simulation of the SG grid is ran and its resulting data is then used with the restart functionality of ReFRESCO, where the flexible simulation takes off from the final time step of the rigid one.

Even with the adopted simplifications regarding the fluid grids and these simulation settings, the results of this test case were not computed in time of the completion of this thesis. In order to make the simulation feasible in a reasonable amount of time, it is suggested that future works parallelise the altered code, so it can run on multiple processors and thus distribute the computational costs among them.

Chapter 7

Conclusions

7.1 Achievements

Having reached the completion of this thesis, the following achievements are identified, encompassing most of the goals set out in the Chapter 1.

Implementation of an interface between beam models and CFD grids

Similarly to the main CFD code, which has an extensive research behind it and a continuing expansion on its capabilities looking forward, the FSI module presents considerable potential to achieve more efficient simulations with simpler structural models, reducing its computational costs. Having this in mind, a coupling interface was established between the CFD grid and models constituted by beam elements.

Aiming to avoid extensive modifications of the main code of ReFRESCO, an already existent coupling method of the software was used for this new scenario: the RBF interpolation. However, because this method is implemented to work in the outer surfaces of the body, the loads and displacements transfer had to be performed with a beam grid and an outer structural mesh, that establishes that coupling with the fluid domain through the RBF interpolation. Through the interchange of displacements and loads of the three grids, the deformation of the body and the surrounding fluid was achieved. This implementation mostly involved changes in functions responsible for the allocation of the input data, RBF interpolation and for updating the structural interface.

The update of the interface was also expanded to degrees of freedom of rotation, in which the node's coordinate system is rotated at each outer iteration, based on the angle computed in the previous one.

Creation of a Computational Structural Dynamics Model with beam elements

The creation of the interface coupling led to another challenge: establishing a user friendly way of setting up the structural model in the FSI simulations, without the need to recur to external commercial software. In order to tackle this problematic, the current work has provided a new tool to represent slender bodies, like the blades of wind turbines, through beam elements: a Computational Structural Dynamics Model with said elements, adjunct to the main code of the CFD solver through user coding in

Fortran 2005.

Aiming for simplicity in its input, this new module only requires one file with an extension *.beam* from the user, containing the properties and grid data of the beam model that represents the body, as well as information concerning the aforementioned outer mesh that establishes the interface with the fluid domain. This new complementary code then generates the necessary mass and stiffness matrices that are provided to run the FSI simulation with ReFRESCO.

After its implementation, the solver was then verified, still working independently from ReFRESCO, with a static and modal analysis. Both studies yielded an exceptional agreement with the reference cases constituted by BEAM4 elements, from ANSYS© APDL.

Validation of the new interface coupling and of the developed beam module

Having achieved both aforementioned objectives, the new interface coupling and the developed beam model were validated with a 2D benchmark of a clamped plate, using as reference a solid model that was already validated by Bronswijk [31].

Regarding the evaluation of the former goal, two test cases for the beam models were tested in an FSI context, for the same conditions and with the same settings. Assessing the tip displacement of the plate and its response frequency to the flow, those models presented an identical behavior in comparison to each other and with small deviations from the results of the validated solid elements test case. From these simulations, it was possible to infer that, in an FSI context, the developed beam solver performs with equal accuracy to simulations with ANSYS© generated data and that the beam interface is portraying properly the benchmark behavior, even if with limitations. Those limitations are resultant of the lack of robustness of the employed algorithm to transfer displacements and loads between the structural grids, which may also be in the root of the low efficiency of the beam simulations when compared with the solid elements. Using an Nearest Neighbor Interpolation between the structural meshes, the outer grid can create quite irregular shapes after its displacements update, hindering the convergence of the code and, in some cases, leading to divergence.

A study on the effect of the refinement of the structural meshes was then conducted, in order to assess its effects on the accuracy and performance of the beam simulations. Combining different levels of refinement from both beam and outer grids, the results were the most accurate, as one would expect, for high refinement from both. It was found that the outer mesh has a predominant impact on the accuracy of the simulations, with limitations nonetheless when working with much coarser beam grids in the spanwise direction. This allowed to be set a precedent on how to handle the wind turbine blade of the DTU, in which the beam should present a dense refinement in comparison with the outer mesh, in order to avoid divergence situations where negative volume cells are reached, due to the irregularity of the updated outer mesh. This refinement should not have much consequences in the performance of the simulations, as the number of outer iterations didn't vary much with the various tested grids.

Moreover, the beam test case with the developed beam solver was simulated with and without considering the implemented rotation degrees of freedom but the results yielded negligible differences, from which one can infer that this feature is not impactful in the interface update of the benchmark. The

importance of this functionality should be reassessed in future works through its testing with set ups that involve more 3D motion of the model at study.

Establishment of the fluid and structural grids to simulate the DTU 10MW RWT

Having the goal of simulating a Rotor-Nacelle Assembly with a flexible blade, multiple rigid models were constructed, recurring to an Absolute Formulation Method approach and to Sliding Grids. Aiming to reduce computational costs, these meshes were tested with lesser refinement than usual in their BL.

Both methods appeared to provide reasonable results for the intended purposes of this work: testing the new FSI implementation quickly, with large simplifications, specially the modeling of the BL with wall functions. Nevertheless, SG are the most versatile ones, since they can be used in real life configurations with bodies that are moving and others that are static. In the case of AFM, one is limited to use them with geometries that move all at the same speed, which precludes the inclusion of tower-rotor interactions, for example.

Furthermore, the structural model was also created, based on the documentation of the wind turbine. In this case, rooted in the conclusions that resulted from the benchmark simulations, a dense refinement was applied to the beam model, in order to avoid possible phenomenons of divergence. Having constructed the model, its modal analysis led to agreeable results with the ones from the reference tool HAWC2 [8].

Yet, it must be recognized that the results of the simulation of the DTU 10MW RWT flexible rotor were not obtained by the date of the conclusion of this thesis, due to the non-parallelisation of the code, imposed by the new interface coupling. Only running on one processor, this condition hindered drastically the calculations of the simulation.

7.2 Future work

From the developed work in this thesis, multiple prospects for future research arise, regarding the improvement of the performance of the simulations and the removal of some of their current limitations, concerning the beam solver and the beam-fluid interface.

Focusing on the beam solver, the basis of the formulation of its beam elements is the BEAM4, a legacy element. This type of element has meanwhile been removed from ANSYS© documentation due to issues with consistency and redundancy. Therefore, other beam elements with different degrees of freedom and/or shape functions can be tested with the developed solver in future works, by changing the stiffness and mass matrices formulation.

Furthermore, considering that one of the main goals of this thesis was to remove the dependency of ReFRESCO on external software to generate the structural data of its FSI simulations, another tool that could prove to be useful in further studies would be a cross section analysis software for beam models, similar to one developed by DTU, BECAS© [80]. This tool would be able to generate essential properties of a blade turbine and provide them to the developed beam solver, galvanizing the conception of more complex structural models with different cross sections across their length.

In what concerns the implementation of the interface between the beam models and the fluid grid, it is important to note that the work of this thesis was developed on the 2.7.0 version of ReFRESCO, with the limitation of only running simulations with one processor. It is essential in further studies that this process is adapted to more recent versions of the software, such as 2.8.0., and that this functionality is expanded to simulations on multiple processors, with the parallelization of the altered code.

Additionally, the mapping of forces and displacements between the outer and the beam structural grids has space for improvement, as a nearest neighbour interpolation was employed in this thesis. The low accuracy of this method greatly influences the shape of the outer mesh and, consequently, the stabilization of the FSI coupling and the performance of the simulation. A possible approach to be made would be to compute a linear extrapolation procedure for the outer mesh, based on the interpolation of the displacements and rotations of the beam nodes, with an adequate level of discretization for both grids (refer to Kamakoti and Shyy [81] and Sayed *et al.* [22]).

Bibliography

[1] S. Horcas, F. Debrabandere, B. Tartinville, and G. Coussement. *MARE-WINT: New materials and reliability in offshore wind turbine technology*. Springer Open, 2016. doi: 10.1007/978-3-319-39095-6_18. URL https://link.springer.com/chapter/10.1007/978-3-319-39095-6_18.

[2] W. Musial, P. Spitsen, P. Beiter, and P. Duffy. Offshore wind market report: 2021 edition. Technical report, U.S. Department of Energy, Office of Energy Efficiency and Renewable Energy, NREL, 2021. URL https://www.energy.gov/sites/default/files/2021-08/Offshore%20Wind%20Market%20Report%202021%20Edition_Final.pdf.

[3] E. Ramos, L. D. Oliveira-assis, R. Mena, and L. Ramírez. Current status and future trends of offshore wind power in Europe. *Energy*, 202(2015), May 2020. doi: 10.1016/j.energy.2020.117787.

[4] H. Glauert. The analysis of experimental results in the windmill brake and vortex ring states of an airscrew. *London: Aeronautical Research Committe*, 1026, 1926.

[5] J. Mourits. BEM theory and CFD for wind turbine aerodynamics. Technical report, University of Twente and University of Liverpool, January 2014. URL https://essay.utwente.nl/69276/1/Report_Internship_Jur_Mourits_final.pdf.

[6] J. M. Jonkman and M. B. Junior. Development and verification of a fully coupled simulator for offshore wind turbines. In *45th AIAA Aerospace Sciences Meeting and Exhibit, Wind Energy Symposium*, Golden, Colorado, January 2007. NREL. URL https://www.nrel.gov/docs/fy07osti/40979.pdf.

[7] A. Heege, A. Gaull, S. G. Horcas, and M. Defourny. Experiences in controller adaptations of floating wind turbines through advanced numerical simulation. In *EWEA 2012 Annual Event Conference*, Copenhagen, Denmark, April 2012.

[8] DTU Wind Energy, HAWC2 info. https://www.hawc2.dk/hawc2-info. Accessed: 2022-02-01.

[9] OpenFast - BeamDyn theory. https://openfast.readthedocs.io/en/main/source/user/beamdyn/theory.html?highlight=beam. Accessed: 2022-02-01.

[10] S. Sureshkumar. *Aeroelastic simulation of small wind turbine using HAWC2*. Master's thesis in

Mechanical Engineering, Blekinge Institute of Technology, 2014. URL https://www.diva-portal.org/smash/get/diva2:830090/FULLTEXT01.pdf.

[11] L. Wanga, X. Liub, and G. M.Hall. Nonlinear aeroelastic modelling for wind turbine blades based on Blade Element Momentum theory and geometrically exact beam. *Energy*, 76:487–501, 2014. doi: 10.1016/j.energy.2014.08.046.

[12] K. Shaler, E. Branlard, A. Platt, and J. Jonkman. Preliminary introduction of a Free Vortex Wake Method into OpenFAST. *Journal of Physics*, 1452(012064), January 2019. doi: 10.1088/1742-6596/1452/1/012064.

[13] J. Dong, A. Viré, C. S. Ferreira, and Z. Li. A modified Free Wake Vortex Ring Method for Horizontal-Axis Wind Turbines. *Energies*, 12(3900), 2019. doi: 10.3390/en12203900.

[14] V. Leble and G. Barakos. Forced pitch motion of wind turbines. *Journal of Physics*, 753(2), 2016. doi: 10.1088/1742-6596/753/2/022042. URL https://www.researchgate.net/publication/308829293_Forced_pitch_motion_of_wind_turbines.

[15] B. P. Epps, B. T. Roesler, and R. B. Medvitz. A viscous Vortex Lattice Method for analysis of cross-flow propellers and turbines. *Renewable Energy*, 143:1035–1052, 2019. doi: 10.1016/j.renene.2019.05.053.

[16] A. Segalini and P. H. Alfredsson. A simplified Vortex Model of propeller and wind-turbine wakes. *Journal of Fluid Mechanics*, 725:91–116, 2013. doi: 10.1017/jfm.2013.182.

[17] Y. Bazilevs, M. Hsu, J. Kiendl, and K. Bletzinger. 3D simulation of wind turbine rotors at full scale. Part II: Fluid-Structure Interaction modeling with composite blades. *International Journal for Numerical Methods in Fluids*, 65:236–253, 2011. doi: 10.1002/fld.2454. URL https://web.me.iastate.edu/jmchsu/files/Bazilevs_et_al-2011-IJNMF-2.pdf.

[18] D. O. Yu and O. J. Kwon. Predicting wind turbine blade loads and aeroelastic response using a coupled CFD-CSD method. *Renewable Energy*, 70:184–196, 2014. doi: 10.1016/j.renene.2014.03.033.

[19] M.-C. Hsu and Y. Bazilevs. Fluid–Structure Interaction modeling of wind turbines: simulating the full machine. *Computational Mechanics*, 50:821–833, 2012. URL https://web.me.iastate.edu/jmchsu/files/Hsu_Bazilevs-2012-CM.pdf.

[20] S.G.Horcas, B.Tartinville, C. Hirsch, and G.Coussement. Mesh deformation tool for offshore wind turbines Fluid-Structure Interaction. In *Abstracts of the 11th World Congress on Computational Mechanics (WCCM XI)*, Barcelona, Spain, July 2014.

[21] S. Vilmin, E. Lorrain, C. Hirsch, and M. Swoboda. Unsteady flow modeling across the rotor/stator interface using the nonlinear harmonic method. In *Abstracts of the ASME Turbo Expo 2006: power for land, sea and air*, Barcelona, Spain, May 2006. American Society of Mechanical Engineers. doi: 10.1115/GT2006-90210.

[22] M. Sayed, T. Lutz, E. Krämer, and S. Shayegana. Aeroelastic analysis of 10 MW wind turbine using CFD–CSD explicit FSI-coupling approach. *Journal of Fluids and Structures*, 87:354–377, 2019. doi: 10.1016/j.jfluidstructs.2019.03.023.

[23] A. D. Otero and F. L. Ponta. Structural analysis of wind-turbine blades by a generalized Timoshenko beam model. *Journal of Solar Energy Engineering*, 132(1), 2010. doi: 10.1115/1.4000596.

[24] C. Júnior, A. Cardozo, V. Júnior, and A. Neto. Modeling wind turbine blades by geometrically-exact beam and shell elements: A comparative approach. *Engineering Structures*, 180:357–378, 2019. doi: 10.1016/j.engstruct.2018.09.032.

[25] T. Sharma, V. Murari, and K. Shukla. Static analysis of wind turbine blade using 1D FE model. *International Journal of Engineering*, 13(1):125–130, 2021. doi: 10.4314/ijest.v13i1.19S. URL https://www.ajol.info/index.php/ijest/article/download/210267/198216.

[26] M. Tüfekci, Ömer Genel, A. Tatar, and E. Tüfekci. Dynamic analysis of composite wind turbine blades as beams: An analytical and numerical study. *Vibration*, 4:1–15, 2020. doi: 10.3390/vibration4010001. URL https://spiral.imperial.ac.uk/bitstream/10044/1/92961/4/vibration-04-00001.pdf.

[27] J. Almeida. *Structural dynamics for aeroelastic analysis*. Master's thesis in Aerospace Engineering, Técnico Lisboa, 2015. URL https://fenix.tecnico.ulisboa.pt/downloadFile/1126518382177903/JoaoAlmeida_Thesis.pdf.

[28] J. Kiendl, K. Bletzinger, J. Linhard, and R. Wuchner. Isogeometric shell analysis with Kirchhoff–Love elements. *Computer Methods in Applied Mechanics and Engineering*, 198(49):3902–3914, 2009. doi: 10.1016/j.cma.2009.08.013. URL https://www.researchgate.net/publication/250693564_Isogeometric_shell_analysis_with_Kirchhoff-Love_elements.

[29] J. Kiendl, Y. Bazilevs, M. Hsu, and R. Wuchner. The bending strip method for isogeometric analysis of Kirchhoff–Love shell structures comprised of multiple patches. *Computer Methods in Applied Mechanics and Engineering*, 199(37-40):2403–2416, 2010. doi: 10.1016/j.cma.2010.03.029. URL https://www.researchgate.net/publication/222330451_The_bending_strip_method_for_isogeometric_analysis_of_Kirchhoff-Love_shell_structures_comprised_of_multiple_patches.

[30] S. Jongsma, E. van der Weide, and J. Windt. Implementation and verification of a partitioned strong coupling Fluid-Structure Interaction approach in a Finite Volume Method. In *12th International Conference on Hydrodynamics (ICHD)*, Egmond aan Zee, Netherlands, September 2016. Technical Report MARIN Academy.

[31] L. Bronswijk. *Fluid-Structure Interaction of self-adaptive marine propellers using RANS-FEM towards the validation of BEM-FEM*. Master's thesis in Marine Technology, TU Delft, 2017.

[32] J. H. Ferziger and M. Perić. *Computational methods for fluid dynamics*. Springer, 3rd edition, 2002. URL http://ftp.demec.ufpr.br/disciplinas/TM701/Ferziger%20Peric%20-%20Computational%20Methods%20for%20Fluid%20Dynamics,%203rd%20Ed%20-%202002.pdf.

[33] *ReFRESCO Theory Manual v2.4.0*. MARIN, October 2017. Version 1.0.

[34] G. Vaz, F. Jaouen, and M. Hoekstra. Free-surface viscous flow computations: Validation of URANS code. In *ASME 2009 28th International Conference on Ocean, Offshore and Arctic Engineering*, pages 425–437, Hawai, USA, July 2009. doi: 10.1115/OMAE2009-79398.

[35] T. Gomes. *Verification study of Sliding and Overset Grid Methods*. Master's thesis in Aerospace Engineering, Técnico Lisboa, November 2021. doi: 10.13140/RG.2.2.33368.42241. URL https://www.researchgate.net/publication/357117073_Verification_Study_of_Sliding_and_Overset_Grid_Methods_-_An_Application_to_Wind_Turbine_CFD_Simulations.

[36] K. Key. *Theory of Fluid-Structure Interaction and implementation of a structural solver for elastodynamics in ReFRESCO*. Bachelor Thesis, Aachen University, May 2017.

[37] V. Wieleman. *Verification and validation of full-scale propulsion analysis using CFD*. Master's thesis in Maritime and Materials Engineering, TU Delft, 2018. URL https://repository.tudelft.nl/islandora/object/uuid:73c8079a-1760-4fca-a05f-166f836163a0/datastream/OBJ/download.

[38] G. Vaz and M. Make. Analyzing scaling effects on offshore wind turbines using CFD. *Renewable Energy*, 83:1326–1340, 2015. doi: 10.1016/j.renene.2015.05.048.

[39] V. Leble and G. Barakos. 10-MW wind turbine performance under pitching and yawing motion. *Journal of Solar Energy Engineering*, 139(4), 2017. doi: 10.1115/1.4036497.

[40] Y. Bazilevs, A. Korobenko, X. Deng, and J. Yan. Novel structural modeling and mesh moving techniques for advanced Fluid–Structure Interaction simulation of wind turbines. *International Journal For Numerical Methods in Engineering*, 102(3-4):766–783, July 2015. doi: 10.1002/nme.4738.

[41] P. I. Muiruri, O. S. Motsamai, and R. Ndeda. A comparative study of RANS-based turbulence models for an upscale wind turbine blade. *SN Applied Sciences*, 1(237), February 2019. doi: 10.1007/s42452-019-0254-5.

[42] K. S. Abdol-Hamid. Assessments of k-kL turbulence model based on Menter's modification to Rotta's two-equation model. *International Journal of Aerospace Engineering*, 12, 2014. doi: 10.1155/2015/987682. URL https://www.researchgate.net/publication/275886216_Assessments_of_k-kL_Turbulence_Model_Based_on_Menter%27s_Modification_to_Rotta%27s_Two-Equation_Model.

[43] F. Moukalled, L. Mangani, and M. Darwish. *The Finite Volume Method in Computational Fluid Dynamics: an advanced introduction with OpenFOAM and Matlab*. Springer, 1st edition, 2015. doi: 10.1007/978-3-319-16874-6.

[44] S. M. Salim and S. Cheah. Wall y+ strategy for dealing with wall-bounded turbulent flows. In *International MultiConference of Engineers and Computer Scientists*. IMECS, 2009. URL https://www.researchgate.net/publication/209105574_Wall_y_Strategy_for_Dealing_with_Wall-bounded_Turbulent_Flows.

[45] L. Eça and M. Hoekstra. On the influence of the iterative error in the numerical uncertainty of ship viscous flow calculations. In *26th Symposium on Naval Hydrodynamics*, Rome, Italy, January 2006.

[46] J. N. Reddy. *An introduction to the Finite Element Method*. Mc Graw Hill, 3rd edition, 2006.

[47] S. S. Rao. *Mechanical vibrations*. Prentice Hall, 5th edition, 2010.

[48] Y. Bazilevs, K. Takizawa, and T. Tezduyar. *Computational Fluid-Structure Interaction: methods and applications*. Wiley, 2013. doi: 10.1002/9781118483565.

[49] Q. Zhang and T. Hisada. Studies of the strong coupling and weak coupling methods in FSI analysis. *International Journal for Numerical Methods in Engineering*, 60(12):2013–2029, 2004. ISSN 00295981. doi: 10.1002/nme.1034.

[50] J. Degroote, K. Bathe, and J. Vierendeels. Performance of a new partitioned procedure versus a monolithic procedure in Fluid-Structure Interaction. *Computers and Structures*, 87(11-12):793–801, June 2009. doi: 10.1016/j.compstruc.2008.11.013.

[51] A. de Sousa Cardeira. *Aeroelastic analysis of aircraft wings*. Master's thesis in Aerospace Engineering, Técnico Lisboa, 2014.

[52] C. Förster, W. A. Wall, and E. Ramm. Artificial added mass instabilities in sequential staggered coupling of nonlinear structures and incompressible viscous flows. *Computer Methods in Applied Mechanics and Engineering 196*, 196(7):1278–1293, January 2007. doi: 10.1016/j.cma.2006.09.002.

[53] HB files - Harwell Boeing sparse matrix file format. https://people.sc.fsu.edu/~jburkardt/data/hb/hb.html. Accessed: 2021-12-14.

[54] Y. Baux. New release - Omnis/HEXPRESS version 5.1. https://www.numeca.com/readnews/article/699/category/155. Accessed: 2022-02-07.

[55] *ReFRESCO Documentation - Tutorials*. MARIN, January 2021. Version 2.7.0.

[56] Y. Yu. *Numerical methods for Fluid-Structure Interaction: analysis and simulation*. PhD thesis, Brown University, May 2014.

[57] C. Wood, A. Gil, O. Hassan, and J. Bonet. Partitioned Block-Gauss–Seidel coupling for dynamic Fluid–Structure Interaction. *Computers and Structures*, 88(23-24):1367–1382, 2010. doi: 10.1016/j.compstruc.2008.08.005.

[58] A. Boer, A. Zuijlen, and H.Bij. Comparison of conservative and consistent approaches for the coupling of non-matching meshes. *Department of Aerospace Engineering, Delft University of Technology*, 197(49-50):4285–4297, 2008. doi: 10.1016/j.cma.2008.05.001.

[59] A. de Boer, M. S. van der Schoot, and H. Bijl. New method for mesh moving based on Radial Basis Function Interpolation. *European Conference on Computational Fluid Dynamics*, 2006. URL `https://repository.tudelft.nl/islandora/object/uuid:8db01fd1-94d0-40d7-8e99-9385bd63b92e/datastream/OBJ/download`.

[60] T. Rendall and C. Allen. Efficient mesh motion using Radial Basis Functions with data reduction algorithms. *Department of Aerospace Engineering, University of Bristol*, 228(17):6231–6249, 2009. doi: 10.1016/j.jcp.2009.05.013.

[61] *Theory reference for the mechanical APDL and mechanical applications*. ANSYS Inc., Release 12.0, 2009.

[62] O. Stodieck, J. E. Cooper, and P. M. Weaver. Interpretation of bending/torsion coupling for swept, non-homogeneous wings. *Journal of Aircraft*, 53(4):892–899, 2016. doi: 10.2514/1.C033186.

[63] W. D. Pilkey. *Formulas for stress, strain and structural matrices*. John Wiley and Sons, 2nd edition, 2004.

[64] G. de Nayer. *Interaction Fluide-Structure pour les corps élancés*. PhD thesis, École Centrale de Nantes (ECN), 2008.

[65] H. Lesmana. *Contribution to numerical modeling of Fluid-structure Interaction in hydrodynamics applications*. Master's thesis in Computational Mechanics, École Centrale de Nantes, 2011.

[66] G. R. Cowper. The shear coefficient in Timoshenko's beam theory. *Journal of Applied Mechanics*, 33(2):335–340, 1966. doi: 10.1115/1.3625046.

[67] L. Eça and M. Hoekstra. A procedure for the estimation of the numerical uncertainty of CFD calculations based on grid refinement studies. *Journal of Computational Physics*, 262:104–130, 2014. doi: 10.1016/j.jcp.2014.01.006.

[68] *Theory reference guide ANSYS APDL 2020 R1*. ANSYS Inc., January 2020.

[69] S. R. Dennis, W. Qiang, M. Coutanceau, and J. Launay. Viscous flow normal to a flat plate at moderate Reynolds numbers. *Journal of Fluid Mechanics*, 248:605–635, 1993. doi: 10.1017/S002211209300093X.

[70] National instruments. Understanding FFTs and windowing. `https://download.ni.com/evaluation/pxi/Understanding%20FFTs%20and%20Windowing.pdf`. Accessed: 2022-05-10.

[71] Spyc: a color-coded version of sparse matrix viewer spy. `https://ch.mathworks.com/matlabcentral/fileexchange`. Accessed: 2021-07-19.

[72] P. Jordaens, S. Milis, N. V. Riet, and C. Devriendt. The use of a large climate chamber for extreme temperature testing and turbine component validation. In *Winterwind Conference*, Vienna, Austria, February 2013. URL https://www.researchgate.net/publication/306022757_The_use_of_a_large_climate_chamber_for_extreme_temperature_testing_turbine_component_validation.

[73] Y. A. Çengel and J. M. Cimbala. *Fluid mechanics: fundamentals and applications*. McGraw-Hill, 1st edition, 2018.

[74] M. Make. *Predicting scale effects on floating offshore wind turbines*. Master's thesis, TU Delft, 2014. URL https://www.researchgate.net/publication/277813591_Predicting_scale_effects_on_floating_offshore_wind_turbines.

[75] I. D. R. Castro. *Design of a 10MW wind turbine rotor blade for testing of a scaled-down floating offshore support structure*. Master's thesis in Sustainable Energy Technology, TU Delft, 2017. URL https://repository.tudelft.nl/islandora/object/uuid:d73de375-25dd-470f-bf8b-54341bb2c218/datastream/OBJ/download.

[76] A. Sedaghat, A. Hassanzadeh, J. Jamali, and A. Mostafaeipour. Determination of rated wind speed for maximum annual energy production of variable speed wind turbines. *Applied Energy*, 205: 781–789, 2017. doi: 10.1016/j.apenergy.2017.08.079.

[77] F. Zahle, C. Bak, N. Sørensen, S. Guntur, and N. Troldborg. Comprehensive aerodynamic analysis of a 10 MW wind turbine rotor using 3D CFD. In *Abstracts of the 32nd wind energy symposium*, National Harbor, Maryland, January 2014. American Institute of Aeronautics and Astronautics. doi: 10.2514/6.2014-0359.

[78] K.-S. Lee, Z. Huque, and S. Han. A study on the y+ effects on turbulence model of unstructured grid for CFD analysis of wind turbines. *Journal of the Korean Association for Spatial Structures*, 15: 75–84, 2015. doi: 10.9712/KASS.2015.15.1.075.

[79] T. Larsen and A. Hansen. *How 2 HAWC2, the user's manual*. Risø, DTU, May 2019. Version 12.8.

[80] BECAS - beam cross section analysis software. https://becas.dtu.dk/. Accessed: 2022-05-07.

[81] R. Kamakoti and W. Shyy. Fluid–Structure Interaction for aeroelastic applications. *Progress in Aerospace Sciences*, 40(8):535–558, 2004. doi: 10.1016/j.paerosci.2005.01.001.

Appendix A

Beam element shape functions

Aiming to interpolate a continuous solution between the discrete values at the mesh nodes, it is crucial to define shape functions for the beam element in the developed solver.

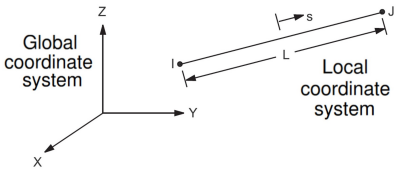

Figure A.1: 3D line element, with local and global coordinate system (adapted from ANSYS manual [61]).

On figure A.1, the three dimensional beam element at study, with nodes I and J, is represented with the respective local coordinate system. Its local coordinate s can be written in function of the global coordinate x through equation A.1 [27], with L as the length of the element at hand.

$$s = \frac{2x - L}{L} \tag{A.1}$$

Considering that the developed beam solver is based on the formulation of BEAM4, one can obtain its shape functions from ANSYS documentation [68]. These functions can be written in the matrix form as seen on equation A.2, where $\boldsymbol{v}$ is the array of displacements and rotations along the element and $N(s)$ contains the shape functions' coefficients. The array $\boldsymbol{v_n}$ encompasses the nodal values correspondent to the 12 degrees of freedom per element that system must compute.

$$\boldsymbol{v} = [N]\boldsymbol{v_n} \tag{A.2}$$

Finally, the system of equations can be written as presented on equations A.3a and A.3b [27] [61], where u and θ correspond to displacements and rotations on the global coordinate system and the subscripts I and J inform on the node whose solution is being computed.

$$\begin{bmatrix} u_x(x) \\ u_y(x) \\ u_z(x) \\ \theta_x \end{bmatrix} = \begin{bmatrix} N1_{u_x} & 0 & 0 & 0 & 0 & 0 & N2_{u_x} & 0 & 0 & 0 & 0 & 0 \\ 0 & N1_{u_y} & 0 & 0 & 0 & N3_{u_y} & 0 & N2_{u_y} & 0 & 0 & 0 & N4_{u_y} \\ 0 & 0 & N1_{u_z} & 0 & N3_{u_z} & 0 & 0 & 0 & N2_{u_z} & 0 & N4_{u_z} & 0 \\ 0 & 0 & 0 & N1_{\theta} & 0 & 0 & 0 & 0 & 0 & N2_{\theta} & 0 & 0 \end{bmatrix} \begin{bmatrix} u_{x,I} \\ u_{y,I} \\ u_{z,I} \\ \theta_{x,I} \\ \theta_{y,I} \\ \theta_{z,I} \\ u_{x,J} \\ u_{y,J} \\ u_{z,J} \\ \theta_{x,J} \\ \theta_{y,J} \\ \theta_{z,J} \end{bmatrix} \tag{A.3a}$$

$$\begin{bmatrix} \theta_y(x) \\ \theta_z(x) \end{bmatrix} = \begin{bmatrix} \frac{du_z}{dx} \\ \frac{du_y}{dx} \end{bmatrix} \tag{A.3b}$$

Table A.1: Basic shape function components [27].

$N1_{u_x} = \frac{1}{2}(1-s)$	$N1_{u_y} = \frac{1}{2}(1-\frac{s}{2}(3-s^2))$	$N1_{u_z} = \frac{1}{2}(1-\frac{s}{2}(3-s^2))$	$N1_{\theta} = \frac{1}{2}(1-s)$
$N2_{u_x} = \frac{1}{2}(1+s)$	$N2_{u_y} = \frac{1}{2}(1+\frac{s}{2}(3-s^2))$	$N2_{u_z} = \frac{1}{2}(1+\frac{s}{2}(3-s^2))$	$N2_{\theta} = \frac{1}{2}(1+s)$
	$N3_{u_y} = \frac{L}{8}(1-s^2)(1-s)$	$N3_{u_z} = \frac{L}{8}(1-s^2)(1-s)$	
	$N4_{u_y} = -\frac{L}{8}(1-s^2)(1+s)$	$N4_{u_z} = -\frac{L}{8}(1-s^2)(1+s)$	

Appendix B

BSM Interfaces from benchmark study

In this Appendix, some examples of interfaces created by the the beam-CFD coupling are presented.

B.1 Divergence

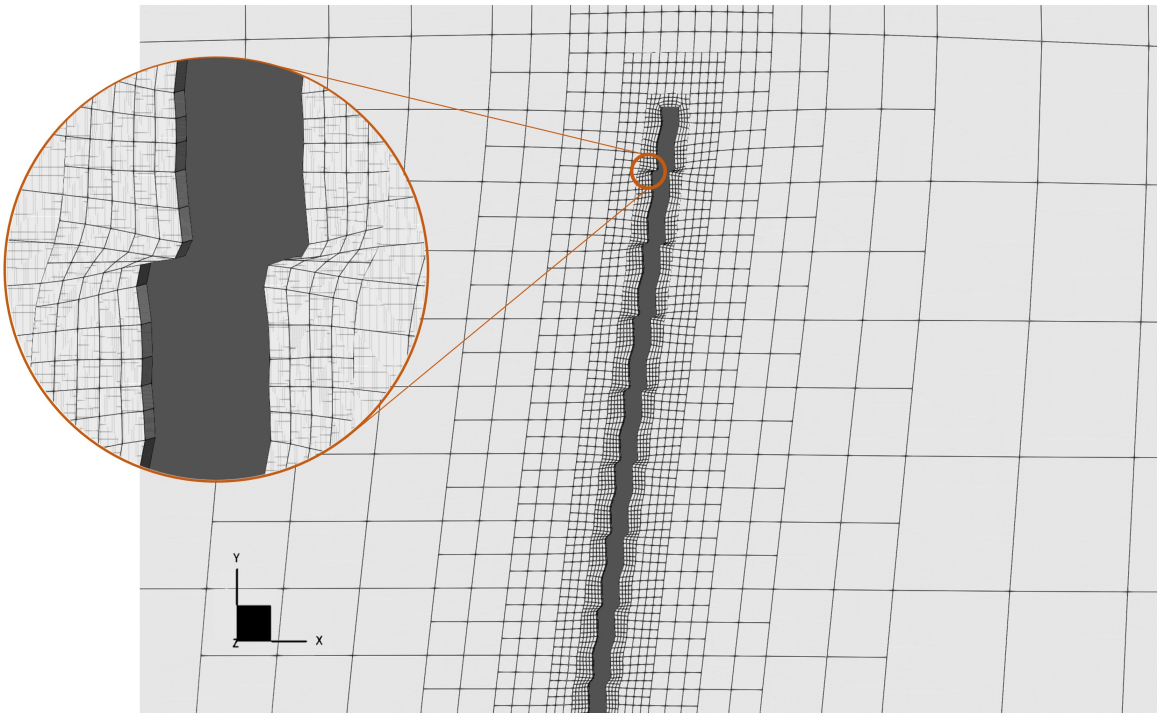

Figure B.1: Time step preceding phenomenon of divergence due to negative volume cells, in combination B1-O4.

B.2 Update interface

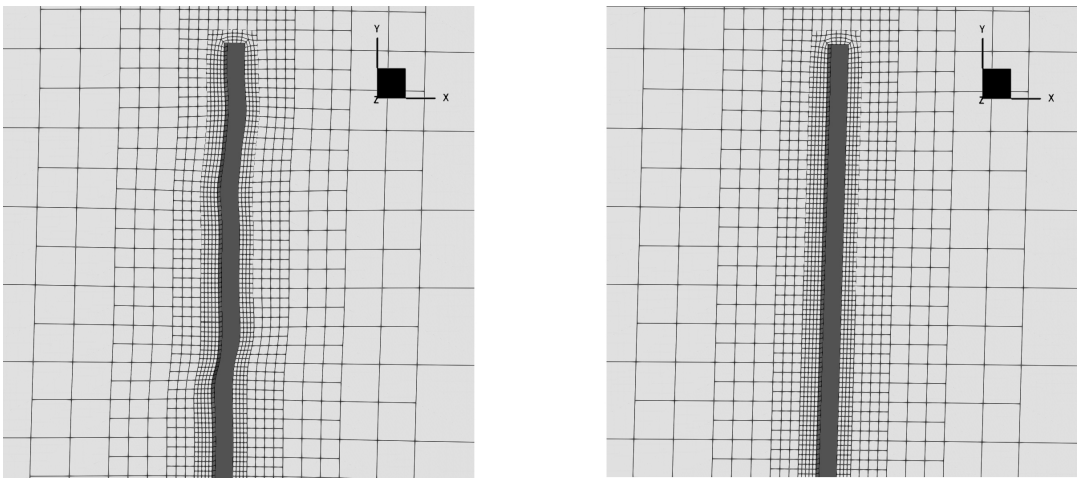

Figure B.2: Amplified interface between outer mesh and CFD grid, for t=6.0 seconds, for a 10 elements beam model (on the left) and a 500 elements one (on the right).

Appendix C

Full-Scale DTU 10MW RWT simulations

The current Appendix focuses on the pre-processing meshing with the AFM approach of the domain with 3.1 million cells, which is quite similar to the SG with less refinement of the BL. This images are followed up by the computed fit curves of the input properties of the beam module, for a blade from the DTU 10 MW RWT. Post-processing figures of the rigid simulation with SG are also presented.

C.1 Pre-processing

C.1.1 Fluid domain

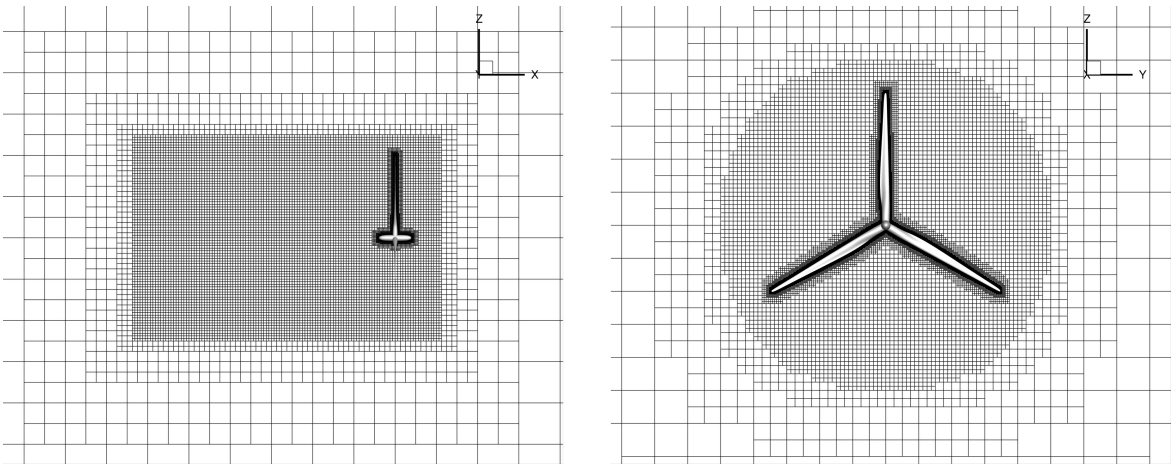

Figure C.1: Amplified side (on the left) and front (on the right) views of the DTU 10 MW RWT grid.

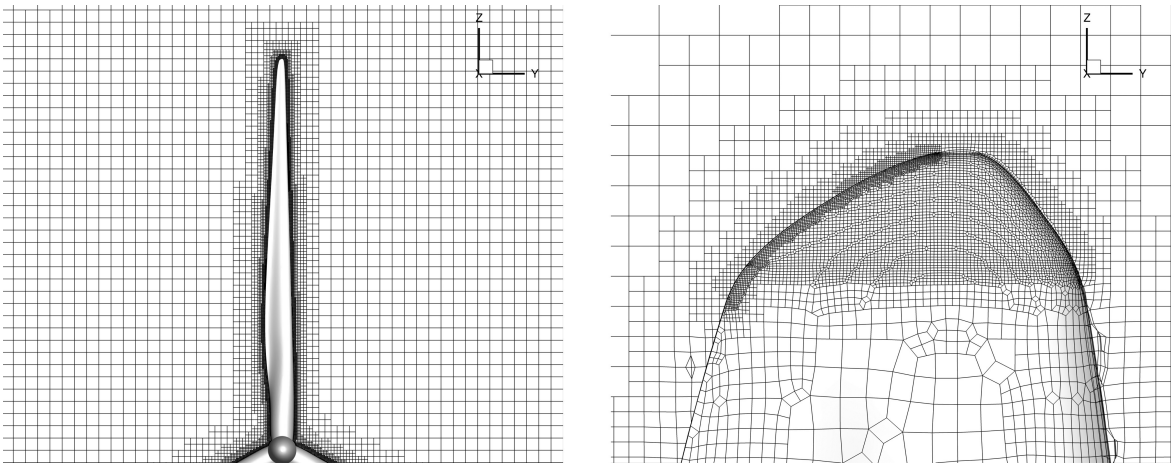

Figure C.2: Amplified view of the refinement around the edge and the tip of the blade for the DTU 10MW RWT.

C.1.2 Structural domain

Aiming to obtain continuous properties of the blade across its length, the presented curve-fitting functions in Equations C.1a-C.1f are used for the plots that follow.

$$\{A, J_p, I_x, I_y\} = a_1 e^{-\left(\frac{z-b_1}{c_1}\right)^2} + a_2 e^{-\left(\frac{z-b_2}{c_2}\right)^2} \tag{C.1a}$$

$$\{\mu, G\} = e^{-\left(\frac{z-b_1}{c_1}\right)^2} + a_2 e^{-\left(\frac{z-b_2}{c_2}\right)^2} + a_3 e^{-\left(\frac{z-b_3}{c_3}\right)^2} \tag{C.1b}$$

$$\begin{aligned} k_x = a_0 + a_1 cos(zw) + b_1 sin(zw) + a_2 cos(2zw) + b_2 sin(2zw) + a_3 cos(3zw) \\ b_3 sin(3zw) + a_4 cos(4zw) + b_4 sin(4zw) + a_5 cos(5zw) \\ b_5 sin(5zw) + a_6 cos(6zw) + b_6 sin(6zw) \end{aligned} \tag{C.1c}$$

$$\begin{aligned} k_y = a_0 + a_1 cos(zw) + b_1 sin(zw) + a_2 cos(2zw) + b_2 sin(2zw) + a_3 cos(3zw) \\ b_3 sin(3zw) + a_4 cos(4zw) + b_4 sin(4zw) \end{aligned} \tag{C.1d}$$

$$x_{sh} = a_1 sin(b_1 z + c_1) + a_2 sin(b_2 z + c_2) + a_3 sin(b_3 z + c_3) \tag{C.1e}$$

$$\begin{aligned} \{y_{sh}, E\} = a_1 sin(b_1 z + c_1) + a_2 sin(b_2 z + c_2) + a_3 sin(b_3 z + c_3) \\ + a_4 sin(b_4 z + c_4) + a_5 sin(b_5 z + c_5) \end{aligned} \tag{C.1f}$$

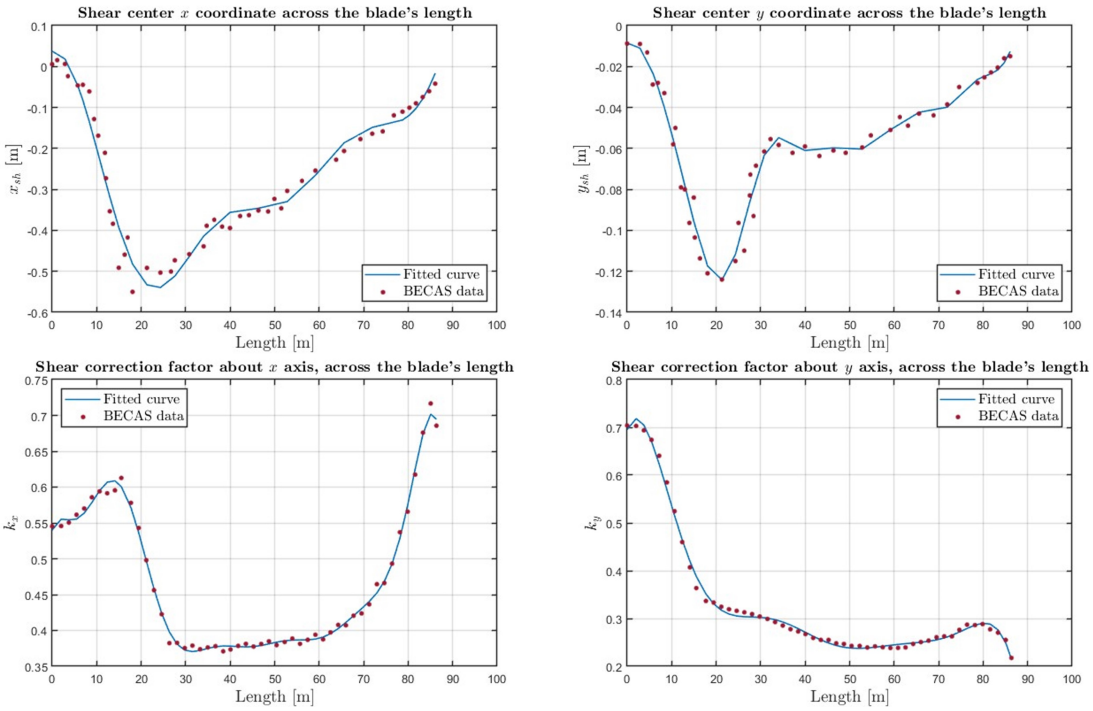

Figure C.3: Variation of the shear correction factors and coordinates of the shear centre of the blade, across its length.

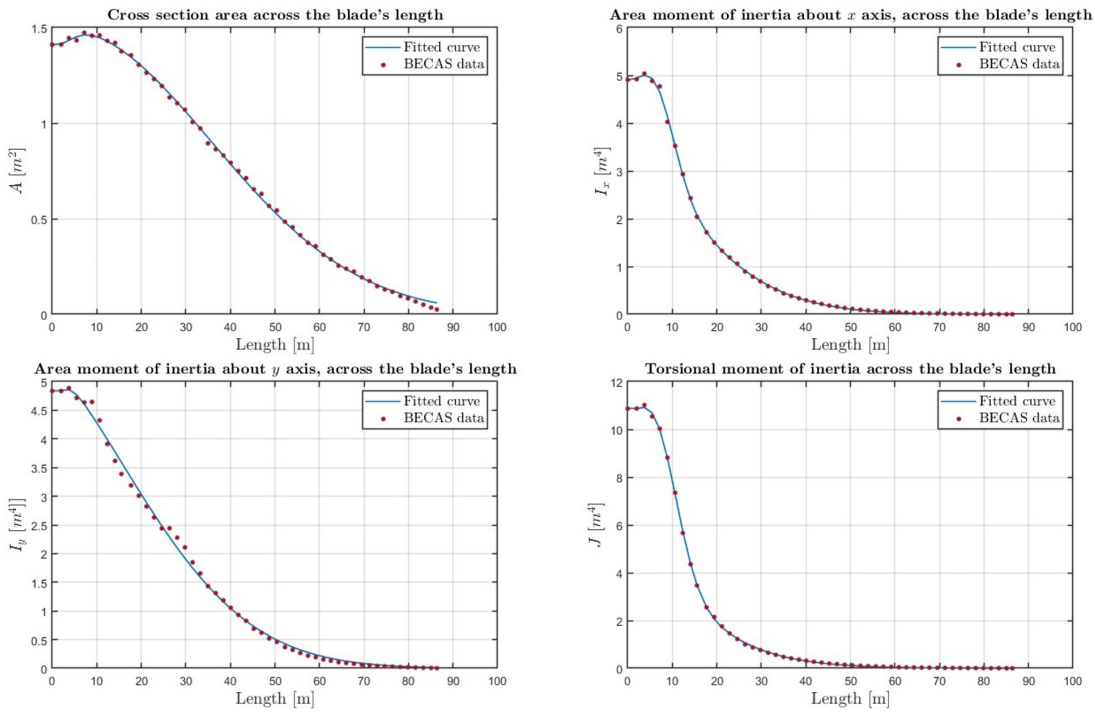

Figure C.4: Variation of the area and moments of inertia properties of the blade, across its length.

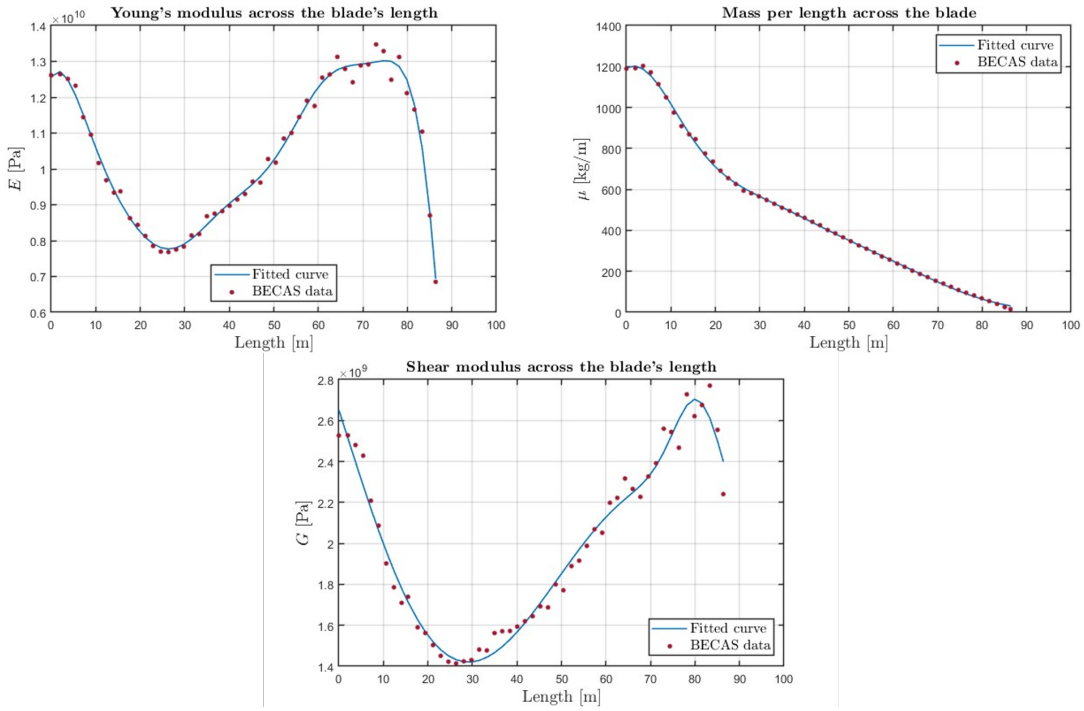

Figure C.5: Variation of the material properties of the blade, across its length.

C.2 Post-processing

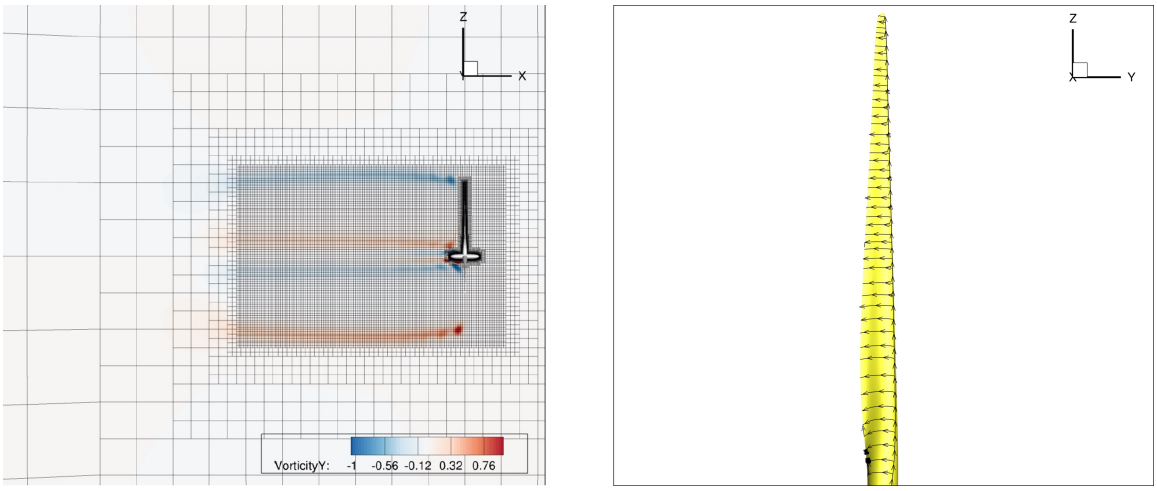

Figure C.6: Vorticity field of the flow around the AFM model of the DTU 10MW RWT's rotor (on the left) and friction streamlines on the pressure side of the blade (on the right).